Nanostructured Silicon for Application in Lithium-ion Batteries and Muon Studies

Chenghao Yue
School of Chemistry
University of East Anglia
Norwich
UK
2020

A thesis submitted in partial fulfilment of the requirements for the degree of Doctor of Philosophy of the University of East Anglia.

© This copy of the thesis has been supplied on condition that anyone who consults it is understood to recognise that its copyright rests with the author and that use of any information derived there from must be in accordance with current UK Copyright Law. In addition, any quotation or extract must include full attribution.

Declaration

I hereby declare that this Ph.D. thesis and the work presented in it are my own, and have not been submitted by me for another degree at this or any other universities. Reference is made to all published work of other authors which I consulted.

Chenghao Yue

Acknowledgement

Firstly, I would like to thank Dr Yimin Chao, my primary supervisor for this great opportunity to carry out my PhD work in his group, for his patience, guidance, support and knowledge.

Secondly, I would like to thank my colleagues during this period, Dr Tiezheng Bian, Dr Ting Li, Dr Qi Wang, Dr Jayshree Ahire, Dr Xiaofeng Wang and Dr Jingyun Ma for their friendship and support.

Thirdly, I would like to express my thanks to Dr Stephen Cottrell at ISIS and Dr Rustem Khasanov at PSI as well as Dr Leandro Miguel Liborio and Dr Simone Sturniolo from RAL who helped me a lot. In addition, I would thank Dr Shaoliang Guan at HarwellXPS for his support and help. Dr Upali A Jayasooriya (University of East Anglia) and Dr Joseph Wright (University of East Anglia) are thanked for their help in the experiments conducted in beamlines.

Most importantly, I thank my parents for their support and encouragement through my research.

Finally, I am also grateful to the scholarship funded by Changzhou Tonghui Solar Electricity Ltd and Biotronik SE & Co. KG.

Abstract

Three types of nanostructured silicon materials have been investigated: Phenylacetylene capped silicon nanoparticle, Biomass SiO_x based material and Hollow structured silicon nanoparticles. The aim of this project is to investigate various silicon nanostructures for better performance in energy applications, for example, high capacity anode materials in lithium-ion battery.

Phenylacetylene capped silicon nanoparticles are synthesized following a bottom up process. Organic ligands are attached to the silicon nanoparticles. This material is used for muon study to get an insight look at the microstructure of the nanoparticles. Muon spin spectroscopy is involved in this project to study the microscopic conductivity between silicon nanoparticles with the ligand (Phenylacetylene) attached to the silicon nanoparticles. Phenylacetylene capped silicon nanoparticles and model molecule are compared using Transverse Field Muon Spin Rotation (TF- μSR) and Avoided Level Crossing Muon Spin Resonance (ALC-μSR). Computer simulations are used for identifying and studying the muon additions.

Biomass SiO_X based material is burned and ball milled from barley husk. With the impurities burned away, only silicon oxide and carbon are left after the initial procedure. Oxygen will react with carbon during ball milling, so the percentage of SiO_x will increase. This material is applied in lithium-ion batteries.

Hollow structure silicon nanoparticles are synthesized via two steps solution process. Glucose solution is used to get produce mono-disperse colloidal carbon on the surface under hydrothermal conditions to wrap the silicon nanoparticles with a thick carbon shell. Titanium isoproproxide was used to get a Ti^{4+} shell outside the carbon shell. Without gas protection, the carbon was burned away and the Ti^{4+} reacts with oxygen to give a TiO_2 shell. This hollow structured silicon nanoparticles are for application in lithium-ion batteries. EMU is a μSR spectrometer which is optimised for zero field and longitudinal field measurements. EMU is involved in this project to investigate the diffusion kinetics of lithium ions in this anode materials.

Access Condition and Agreement

Each deposit in UEA Digital Repository is protected by copyright and other intellectual property rights, and duplication or sale of all or part of any of the Data Collections is not permitted, except that material may be duplicated by you for your research use or for educational purposes in electronic or print form. You must obtain permission from the copyright holder, usually the author, for any other use. Exceptions only apply where a deposit may be explicitly provided under a stated licence, such as a Creative Commons licence or Open Government licence.

Electronic or print copies may not be offered, whether for sale or otherwise to anyone, unless explicitly stated under a Creative Commons or Open Government license. Unauthorised reproduction, editing or reformatting for resale purposes is explicitly prohibited (except where approved by the copyright holder themselves) and UEA reserves the right to take immediate ‘take down’ action on behalf of the copyright and/or rights holder if this Access condition of the UEA Digital Repository is breached. Any material in this database has been supplied on the understanding that it is copyright material and that no quotation from the material may be published without proper acknowledgement.

Contents

Chapter 1: Introduction

Chapter 2: Experimental details

Chapter 1: Introduction

This chapter introduces the basic concepts and background, such as batteries, lithium-ion batteries, electrical vehicles, silicon and nanoparticles. Motivations of this work and future work on biomass SiO_2-C are also included in this chapter.

Contents

1.1 Energy storage systems

1.1.1 Background

Energy is one of the most important and popular topics that have been discussed in the 21st century for a long time. With the rapid depletion of fossil fuels and the increasing deterioration of the environment due to pollution caused by the consumption of large amounts of fossil fuels, there is a high demand for efficient use of energy and a search for renewable and clean energy alternatives to fossil fuels, thus making our development possible.

Energy storage is an intermediate step for the multi-purpose, clean and efficient use of energy. It has attracted worldwide attention and ever-increasing research interest. Energy storage can be traced back to ancient times; it is very simple and natural. Humans initially used forest charcoal, a storage carrier for solar energy biomass, for burning. The fire brought warmth and light, cooked food, and later produced bronzes and irons, so charcoal energy became one of the most important powers of ancient civilisation. About 900 years ago, people discovered coal, which is a product resulting from buried plants that grew millions or even billions of years ago. It stored solar energy at a much higher density than wood or charcoal, and stored it. Later, in the 18th century, coal was used as fuel to drive steam engines, which were a symbol of the first industrial revolution, and later it was used to produce electricity.[1] Petroleum is derived from the residues of biodegradable organic materials and is another high-density solar energy storage medium that has been extensively exploited and used since the early 20th century. Petroleum is obviously not just a fuel; as well as being used to power vehicles with VI internal combustion engines, it is also used to make synthetic fibres, resins, plastics and almost everything in our lives today.

Coal, oil and natural gas are the main energy carriers. They naturally collect and store solar energy for billions of years. Since the invention of electric motors and generators in the 1870s, electrical energy has become the most important secondary energy source and the main form of energy consumption. Electricity can come from fuel, solar power, hydropower, wind power, nuclear power, tidal energy and biological power generation systems, and it is indispensable in almost every part of our lives, from lighting, heating and cooling and cooking to entertainment, transportation and communication. With the rapid development of modern industry and the continuous growth of the global

population, the rate of electricity consumption has risen sharply, and its consumption methods have become more and more diverse. Energy storage has become more complex and important, and ideal high-performance energy storage technologies are needed to achieve efficient, universal and environmentally friendly use of energy, including electricity. In a typical energy storage process, one type of energy is converted into another form of energy, which can be stored and converted to use when needed. Therefore, various energy storage systems are being developed for proper utilisation of different energy supplies.

1.1.2 Energy storage systems for the efficient use of energy

The consumption of electricity is usually not even and there are on-peak and off-peak loading vibrations. By storing the off-peak electricity and releasing the stored energy during the on-peak period, the efficiency, stability, and reliability of an electricity supply system can be significantly improved. Mechanical energy storage and thermal energy storage are mainly used for such peak load shifting.

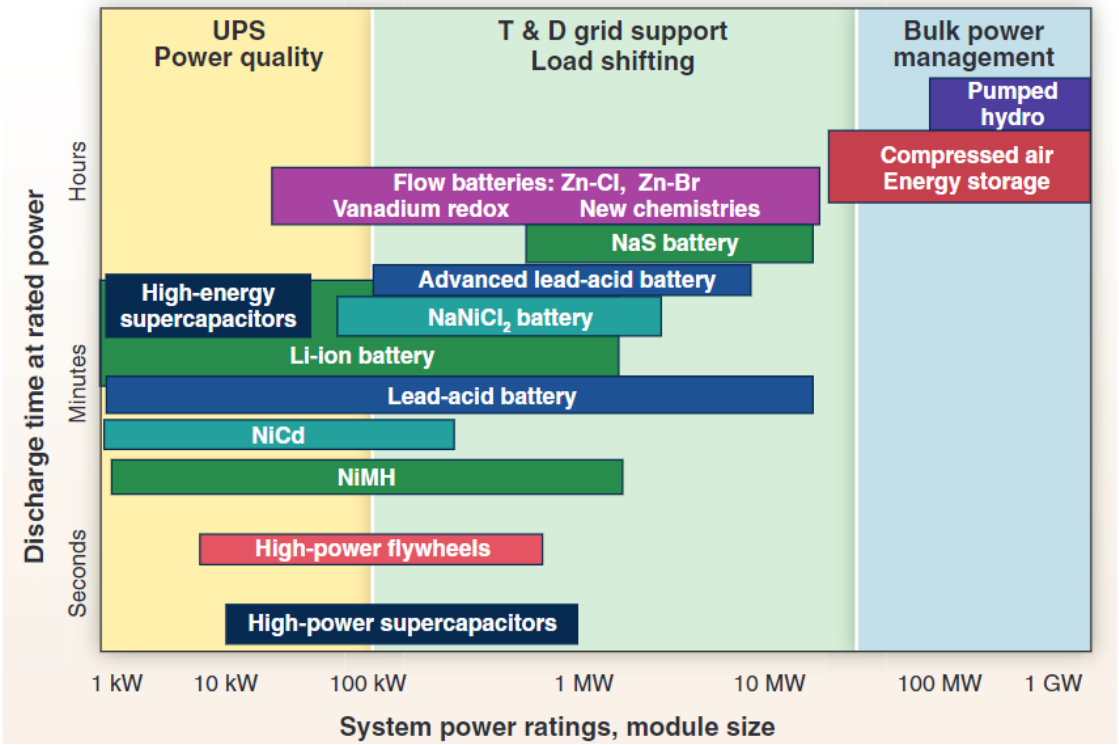

Figure 1. Comparison of discharge time at rated power for different electrochemical energy storage systems. [2, 3]

Energy storage technologies useful for large-scale applications can be divided into four different systems: mechanical, electrical, chemical, and electrochemical.[2] This project focused on batteries, which belong to the electrochemical energy storage system. A comparison of discharge time at rated power of different electrochemical energy storage systems is shown in Figure 1. Generally, an electrochemical energy storage system has some desirable features, such as low-polluted operation, a long lifetime and low maintenance. Also, their size means that batteries can be installed for use at the situation of different kind of renewable resources.

1.2 Background of battery

The battery is the key word of the project and an important part of our lives. Batteries have always been the bottleneck of portable electronic devices. The capacity of batteries has not been greatly improved for a long time, which can not satisfy the performance of electrical equipment. In addition to portable electronic devices, batteries are a hot topic in the automotive field. Electric vehicles (EV) will help to reduce carbon dioxide emissions.[4] Regardless of which battery technology is considered, the measure of its performance (for example, battery potential, capacity or energy density) is related to the inherent characteristics of the materials that make up the positive and negative electrodes. Cycle life and life depend on the nature of the interface between the electrode and the electrolyte, and safety is a function of the stability of the electrode material and the interface.

1.2.1 Introduction to battery

With the fast development of technologies, power sources have been playing more and more important roles in our life. However, the majority of power comes from non-renewable energy resources. The more non-renewable resources we use, the more pollution we create. The environmental problem has become one of the biggest problems we have to face. The trend of using cleaner power is a reasonable choice. The demand for batteries has increased quickly, although we have been using batteries for a long time in history.

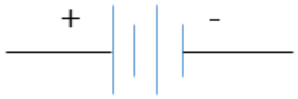

Figure 2. The symbol for a battery in a circuit diagram

Battery is a device for power storage. The symbol for a battery in a circuit diagram is shown in Figure 2. In a narrow sense, it transfers chemical energy to electric energy. Generally, it is used to transfer energy previously reserved to electric energy that can be used in a wide range of applications. Primary batteries can be used only once, because the electrode materials become different from their original state once discharged. The usual example is an alkaline battery used for some portable electronic devices. There is another kind of battery called a secondary battery. Secondary batteries are rechargeable multiple times. The original electrode can be stored again by a reversed current. Jose Alarco said that "In 1938 the Director of the Baghdad Museum found what is now referred to as the 'Baghdad Battery' in the basement of the museum. Analysis dated it at around 250BC and of Mesopotamian origin.".[5] The term "batteries" was first used in 1749 when the Italian physicist Alessandro Volta invented the first battery in the true sense. Volta used discs of copper and zinc as the cathode and anode. A piece of cloth soaked in electrolytes (salty water) was used as a separator: wires connected to the anode and cathode produced a stable and continuous current. However, this true battery is not the battery we use most widely in modern society. The lead-acid battery is the oldest example of a rechargeable battery. This kind of battery is still being used to start car engines today (see Figure 3).

Figure 3. A typical lead-acid battery for cars engine start

Nowadays, batteries come in a large range of sizes and shapes. Different sizes of batteries have different uses in our lives. For example, a large one can be used to start a car's engine, while a tiny one can be used in electronic watches (Figure 4).

Figure 4. Common sizes and shapes of batteries.[6]

Basically, there are two different types of battery cell. The first one is dry cell, while the second one is wet cell. Dry cell batteries typically have the same construction, see Figure 4. At the centre of the battery is a stick called the cathode. This stick is often made of carbon with the electrolyte paste surrounding it. Many kinds of chemicals can be used for the electrolyte, such as ammonium chloride, depending on the type of battery. There are two terminals in the anode of a dry cell battery. One is positive and one is negative. A wet cell battery can be recharged by effectively reversing the chemical process. It is different from a dry cell battery. Wet cells are used widely in automobiles. A lead-acid battery is used to start the vehicle. These batteries contain lead, lead oxide, plates and a liquid electrolyte. The electrolyte

solution contains 65% water and 35% sulphuric acid. After being used for a long time, a wet cell battery can no longer provide electricity like the first time it was used. This happens because the material activity decreases during the charging and discharging cycles. The performance of wet cell batteries becomes worse in a hot climate because the water evaporates out of the electrolyte solution. The wet cell battery was one of the first modern battery types to be developed. A series of improvements has produced the batteries that are commonly used today.

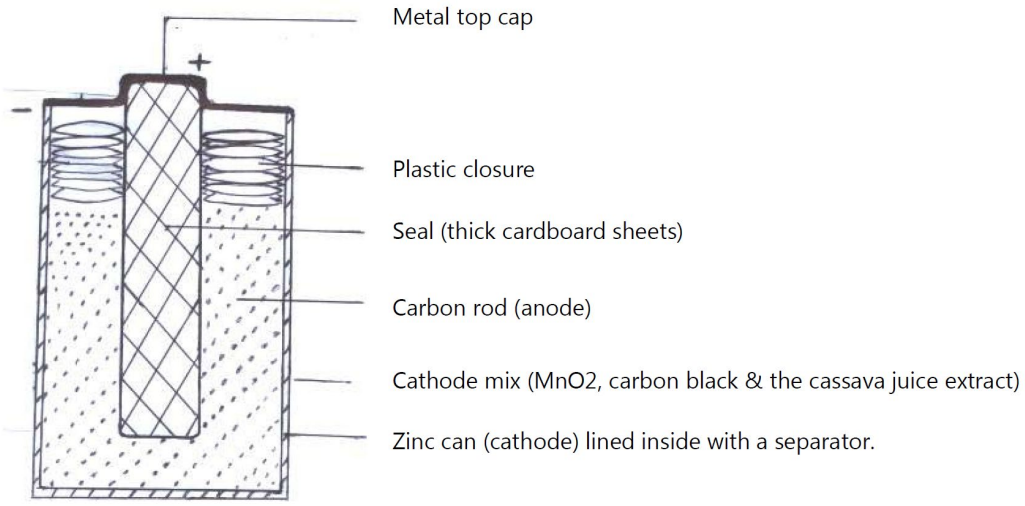

Figure 5. The construction of dry cell.[7]

There are several kinds of commercially important rechargeable battery systems, with lead-acid, alkaline nickel-cadmium, nickel-metal hydride, sodium and lithium batteries dominating the market. They have conquered an important niche in electrical grid applications.[8] The diagram showing the structure of dry cell contains cathode, anode, separator and metal top cap in Figure 5. Dry cell converts the chemical energy to electrical energy and the reaction is irreversible. The zinc is more positive than MnO_2 in reaction, so the electron travels from zinc to MnO_2 and produce power.

The lead-acid battery was invented by Gaston Planté by combining a lead/lead sulphate and lead dioxide/lead sulphate electrode. He demonstrated it before the French Academy of Sciences in 1860. The battery had a low capacity because the electrodes were produced by electrochemical cycling of lead plates in H_2SO_4 solution. Fauré increased the capacity by coating the lead plates with lead

oxide paste to form active masses. Volckmar and Sellon replaced the lead sheets with lead-antimony (PbSb) grids. Barton proposed a method of PbO manufacture by oxidation of molten pulverised Pb and Shimadzu by friction of lead balls in mills. The technology evolved into manufacturing pastes from tri- or tetrabasic lead sulphates, the pasting of grids and the electrochemical formation of electrodes. Thanks to this technology, skeleton and energetic structures are formed in both active masses. The capacity of the negative plates was improved by adding lignosulfonates, BaSO4 and carbon to the paste.[9] A nickel-cadmium battery is a reliable battery with a long lifetime. Industrial nickel-cadmium batteries are available for starter, standby and cycling services because of their lower cost. These are normally pocket plate types which are vented to the atmosphere through resealable vents in each cell to relieve abnormally high internal pressures without spontaneous oxidation of their cadmium negative plates by atmospheric air. Industrial pocket plate cells are suitable for solar photovoltaic systems and can be considered by the system designer.[10] The nickel-metal hydride battery has the advantage in the cycle life. Typically, NiMH batteries can be recharged hundreds of times; however, the limit of the battery life is only 5 years or less. This can make rechargeable NiMH batteries a cost-effective power source for many frequently used battery operated devices found in the home or office [11]. The lithium battery also plays an important role and many different materials are used for its anode and cathode.

Most lithium-ion batteries use organic solvents as the electrolyte, the most common being $LiFP_6$, which has a low electrical resistance, and is typically mixed with carbonates. Solid electrolytes, including polymers and inorganic compounds, are used for solid state batteries, which have advantages in terms of miniaturisation and durability. The most common anode materials are carbon-based compounds and lithium-containing alloys. Both approaches result in the establishment of a reduced lithium activity (compared to lithium metal), which reduces reactivity with the electrolyte and improves safety, but also leads to a lower cell voltage. There are efforts being made in the development of improved electrolyte and anode materials. [12] Silicon has been one the most popular materials for the anode of lithium battery.

1.2.2 Importance of batteries

Batteries have become more and more important with the increasing demand for electrical devices. They are an absolutely necessary part of our lives. Nowadays, many devices need batteries. We bump into batteries in everyday events unconsciously. A battery is used to generate electrical energy. It provides the power for mobile phones, remote control, flashlights, electronic watches and some wireless devices, and it even helps cars to start. The battery has been a reliable way of producing energy while people are on the go. People do not need to carry the fuel to supply the power of the devices they need. The use of batteries also reduces the size of the devices that need power. Batteries have been one of the most convenient ways to store energy. People use batteries so often every day that their existence is ignored.

1.2.3 Types of batteries

Disposable batteries tend to be used to power devices such as remote controls, flash lights, hearing aids and weight scales. Rechargeable batteries tend to supply the power for digital cameras, remote-controlled cars, home-maintenance tools and more. Batteries are also used in medical environments. Hospitals and emergency services use batteries to make it possible to move electrocardiographic heart monitors with patients to provide the vital information of patients. The battery can be used to store extra energy and provide it when required.

1.3 Lithium-ion battery

1.3.1 Introduction to Lithium-ion battery

Lithium batteries are primary batteries. This kind of battery has lithium as an anode. It was invented by Edison. Lithium is an active material. Because of this, its processing, storage and use need specific environmental requirements. Lithium batteries have only been developed relatively recently. With the development of microelectronics technology in the 20th century, the demand for portable electric devices increased rapidly. These devices required batteries. Lithium batteries started to be developed fast. The lithium battery was used for artificial pacemakers because of the stable current it provides. It can be put into body without charging. People started to research the use of different materials for batteries to improve their performance. In 1999, Sony introduced the lithium-ion battery for mobile phones and laptops. The use of this lithium-ion battery successfully reduced the size and weight

of these portable electrical devices. Figure 6 shows how a lithium-ion battery produces electricity.

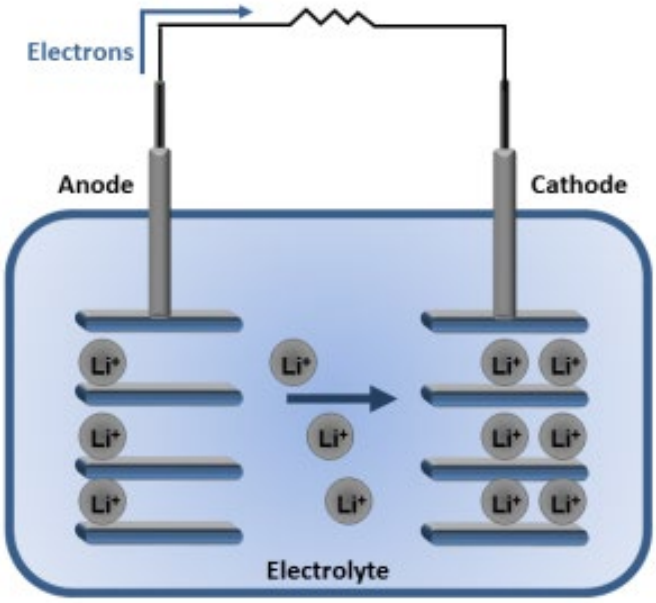

Figure 6. How a lithium-ion battery produces electricity.[13]

It was discovered by researchers at Stanford around 1970 that a range of electron-donating molecules and ions could be intercalated into the layered dichalcogenides, such as M_xTiS_2, and vanadium phosphates/oxides, such as M_xVOPO_4.[14] The first lithium battery was produced between 1972 and 1980. After that, Sony combined LiCoO2 as a cathode with a carbon anode, making the first successful lithium-ion battery.[15] It owes its name to the lithium-ion transfers between the graphite-based anode and the cathode.[16] Compared to the widely used mature battery technologies such as lead-acid or Ni–Cd, the rechargeable lithium-ion battery is still in its early development period, and it will attract a lot of interest for improvement over the next decade. Battery chemistry and cell assembly engineering are the most popular ways to improve battery performance.[17] The energy densities for most of the common rechargeable batteries are shown in Figure 7. The higher specific power means higher working current and the higher specific energy means higher capacity with lower weight. The lithium-ion battery shows higher specific energy and specific power than sodium-based and Li-metal battery.

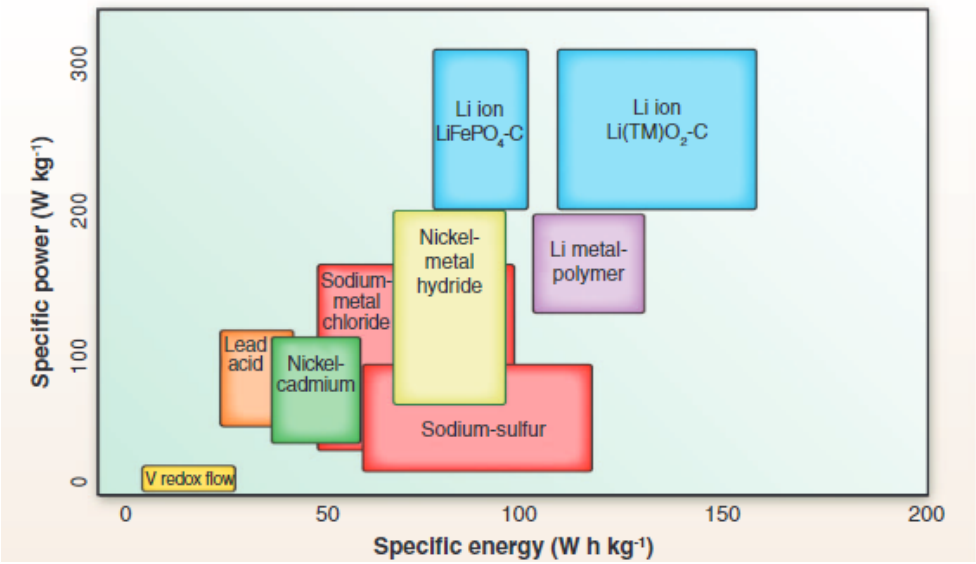

Figure 7. Gravimetric power and energy density for different rechargeable batteries. Most of these energy storage systems are currently being investigated for grid storage applications.

The performance of lithium-ion battery continues to improve, but the energy density and cycle life time are still the main bottlenecks for application in consumer electronics, transport and large-scale renewable energy storage.[18-20]

Lithium-ion batteries have long been a very common source of energy storage. This is because they have higher energy density and lower cost, and this cost is reduced year by year, as shown in Figure 8 (estimated annual cost of lithium-ion batteries, 2010-2018) and Figure 9 (car battery price). In recent years, the two main reasons why these batteries have become a source of considerable research are: 1) they are being studied for use in EVs; and 2) they are being explored for storing excess energy generated by wind and solar power in the grid. In recent years, as the supply of materials has decreased, the high demand for lithium-ion batteries has been met. As shown in Figure 9, the reserve base of lithium-based batteries is close to or lower than that of all other cases. Since 2007, daily electricity consumption has increased significantly, meaning that new batteries must use new materials to meet the growing energy demand. In addition, lithium-ion batteries are usually not recycled because the high cost of doing so is higher than the cost of manufacturing them. This has led to the exhaustion of the limited resources required to keep up with the mass production of these batteries. In addition, the cost of lithium-ion batteries is expected to stop falling in the next few years. This is due to energy and material limitations.

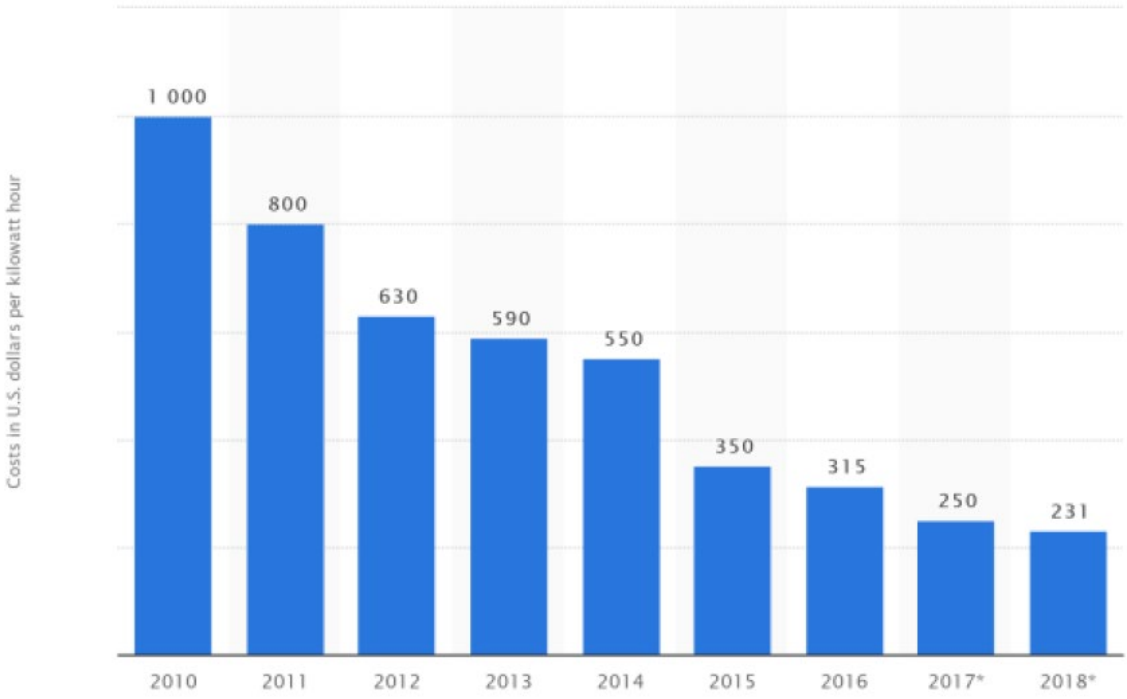

Figure 8. Costs in US dollars per kilowatt hour for lithium-ion batteries.

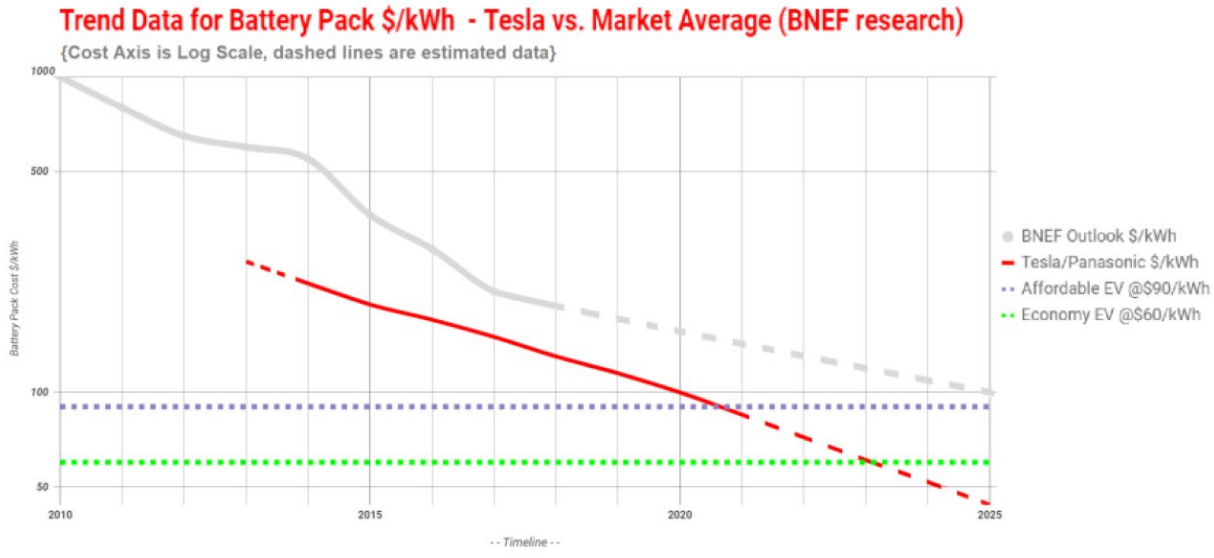

Figure 9. Price trend data for battery packs (Tesla vs. market average).

The use of rechargeable batteries in EV applications has become very popular in recent years[21-23] since renewable energy sources such as solar and wind energy are intermittent in nature and cannot be employed where a continuous and reliable supply

is required.[24] Various energy storages, such as lead acid, NiMH and lithium-ion batteries have been used in EVs.[25] Among them, the lithium-ion battery is widely accepted due to its high energy density, long lifespan and high efficiency.[26, 27] Because of its lucrative features, many investments have already been made to enhance the stability and robustness of lithium-ion batteries.[28] Despite their high primary cost, the market growth of lithium-ion batteries has been increasing steadily and is expected to continue its growth.[29]

Other non-lithium chemistries are being researched at present, and these may compete with lithium batteries. However, alternatives to lithium are limited, because prospective systems need to have high energy density and achieving this requires light metals such as sodium, magnesium and aluminium.

1.3.2 Advantages and disadvantages of lithium-ion batteries

Lithium batteries are used in people's daily lives. They have seven benefits over the old generation of batteries. Firstly, one of the most important advantages is that the lithium battery has high energy density. This means that it can have a high-power capacity without being large, making it suitable for small electrical devices. This is one of the reasons why people use it so widely. Its second advantage is low maintenance. The lithium battery is different from other kinds of batteries. All the maintenance it requires is to ensure that all the cells in the battery are charged equally and that can be done by a good energy management system automatically. The lithium battery has a low self-discharge rate, which is its third advantage compared to other kinds of batteries. So, if you have a fully charged lithium battery and another kind of battery and both are not rechargeable, the lithium one can retain its charge for longer. The forth reason is that the lithium battery can be charged quickly. This is one of the main reasons why this battery is preferred over the others, especially when devices need to be charged frequently. The fifth reason is its smaller size and weight. This characteristic of the lithium battery means that it can be installed to power small and lightweight devices. This benefit makes the lithium battery suitable for more occasions than other types of battery. The sixth advantage is longevity. A long lifetime is a very important characteristic of a battery. It can be charged over and over again without a significant drop in battery capacity. The lithium battery can last longer than others, meaning that it is perfect for devices that need to be used for

a long time before the battery dies. The last advantage is that lithium batteries are much cleaner and safer for the environment. The environment is a popular topic and we cannot ignore the low environmental impact of the lithium battery.

However, the lithium battery has some disadvantages as well. The lithium battery is too expensive for use in cheap applications. In fact, the cost of a lithium battery is much higher than that of other batteries such as a lead-acid battery. Transportation problems have been one of the restrictions of the lithium battery. Although you can carry a small number of lithium batteries with you in your luggage when fly, it causes inconvenience in our lives. A lithium battery needs circuit protection to overcome the safety issue. It can take a series hit when the lithium battery is charged constantly. The lithium battery has circuit protection to make sure that the voltage and current are controlled within safe limits. The additional circuit protection also adds to the cost of the lithium battery.[30] Actually, lithium-ion batteries would also need to reduce the carbon emission when manufacturing, so it is arguable whether or not it is environmentally friendly to promote the use of these batteries.

1.3.3 Background of sodium-ion battery

Sodium-ion batteries are very common and are always being compared with the lithium-ion battery. Sodium-ion batteries are cheap as sodium is abundant in seawater and other natural sources, whereas lithium needs to be mined. Additionally, sodium-ion batteries drain completely, whereas lithium-ion batteries retain 30% of their charge capacity, which is enough to cause an ignition following a short-circuit, which demonstrates that sodium-ion batteries are safer in this respect. Furthermore, unlike lithium, sodium is relatively cheap to recycle. Lithium has a cost of 13,900 USD per metric ton[2], whereas sodium has a cost of 152 USD per metric ton[2] (values are of carbonates in the US in 2017).

Due to the size of the sodium ions (1.0 Å) compared with the lithium ions (0.7 Å), the charging and discharging times of sodium-ion batteries are rather longer than those of lithium-ion batteries. Another difference is their weight, with lithium at around 7 g·mol-1, and sodium about three times heavier, at around 23 g·mol-1, which leads to pure sodium having a capacity of only 1165 mAh·g-1 compared to pure lithium at 3829

mAh·g-1 3. This causes sodium-ion batteries to be less desirable to consumers as the batteries would be larger and heavier, and would take longer to charge.

Another option for energy storage is the sodium sulphur battery. This battery has a large capacity of 750 Wh·kg-1, compared to Li-ion at 100-265 Wh·kg-1 and Na-ion at 90-115 Wh·kg-1. It also has a low cost of 300 USD/kWh. With cheap, easy to obtain, abundant materials and very high energy density and capacity, sodium sulphur batteries appear to be the solution to all the energy storage problems. However, sodium sulphur batteries have molten electrodes, which means that they will not run below the melting point of sodium, which means that they need to operate at temperatures of about 300–400°C. This causes an issue with most applications of these batteries; for short-running batteries such as in cars, sodium sulphur batteries would need to either be kept heated even when not in use, or have an extra alternative battery to run while the sodium sulphur battery heats up. For these reasons, sodium sulphur batteries are generally confined to grid power storage for renewable energy sources. With regard to wind power, there are times where turbines require curtailment; a switching off of the turbines at certain times to comply with grid limits. With the use of sodium sulphur batteries, there can be storage of energy when the turbines are producing an excess, followed by a discharge of this energy into the grid when power from the turbines is low or absent. The high energy density of these batteries and the fact that they would not need to be switched off in this situation leads to sodium sulphur being the predominantly better option for renewable energy surplus storage.

1.4 Nanostructured material as an anode for lithium-ion batteries

The anode is the electrode in batteries that allows electrons to flow in from an outside circuit. It is filled with negative electrons in the batteries and produces electricity. However, it plays the role of a positive terminal in devices that consume electricity.

1.4.1 Nanomaterials for lithium-ion batteries

Most attempts to improve the design of lithium-ion batteries have tackled the problem on the macroscopic scale, but work is now focusing on the nanoscale. Nanomaterials were slow to enter the field of energy storage because of the effective increase in the materials' surface area. Nanomaterials change the reaction pathway and improve the performance of the battery system.[31] Nanotechnology provides benefits in terms of higher capacity and rechargeability,[32] although there is still a long way to go to generate a new complete battery system.

Materials with one or more dimensions on the nanoscale can be called nanomaterials. These materials take any number of forms, including materials which have 1, 2 or 3 dimensions on the nanoscale or bulk materials with features within them that have dimensions on the nanoscale. Nanomaterials are one of the ways to improve the performance of the materials for use in batteries.

Nanochemistry involves the study of nanoscale particles of matter that do not exhibit properties belonging to the macro or molecular states.[33] The first coining of the phrase “nanotechnology”, the wider application of these nanoparticles, is thought to have been by Norio Taniguchi in 1974; he defined it as mainly consisting of the processing of materials by one atom or molecule. This relatively new area of study, nanochemistry, only began to gain research interest in the 1980s after Ekimov’s pioneering paper in which a structure known as quantum dots was first observed,[34] although its importance is as old as universal life. For example, in photosynthesis, nanostructures are able to focus and exploit light in order to produce chemical energy that may be used by the plant or any animal that may consume it.

The human usage of nanomaterials has occurred for many years. Artefacts from the Roman Empire, such as the ‘Lycurgus Cup’, have been found to contain colloidal gold in the glassware, causing a red hue to be observed when light passes through.[35] Further historical usage of nanomaterials can be seen in the form of lustreware, which

are ceramics decorated with typically copper and silver nanoparticles layered on lead-rich glazes associated with the 9th and 10th century Islamic empire. They were used to give colours ranging from yellow-green to amber, depending on the ratio of copper to silver.[36] Certain ratios would give a characteristic gold colour that led some to believe that the technique was in fact a form of alchemy.

There are several potential advantages and disadvantages to using nanomaterials as electrodes for lithium batteries. The advantages include: (i) easy to insert and remove lithium, which improves the cycle life; (ii) higher electrode/electrolyte contact area because of the high surface area, which leads to a higher charge/discharge rate; (iii) short pathway for lithium-ion to travel. Nanomaterials are not easy to make because it is difficult to control the size. Besides the advantages mentions above, there are also disadvantages to using nanomaterials. These include: (i) self-discharging, poor cycling and calendar life because of the high surface area; and (ii) more complex synthesis and difficulties controlling all the nanoparticles.

1.4.2 Nanostructured anode materials

Metals and semiconductors, such as aluminium, tin and silicon, react with lithium through an electrochemical process; in batteries this can be reversed partly, and some of them can provide a much higher specific capacity than the specific capacity offered by graphite, which is used widely as a commercial anode material in lithium-ion batteries.[37] For example, silicon has up to 4200 mAh/g theoretical capacity, which is over ten times the 372 mAh/g for graphite. However, huge volume changes occur within lithium transport.

Although these structural changes are common to the alloying reaction while charging and discharging lithium-ion batteries, there have been many attempts to limit the side effects. The concept of active and inactive nanocomposites is one of the attractive routes. Two materials are mixed commonly, one reacting with lithium, the other acting as an inactive buffer to improve the stability and reversibility of the alloying reaction. By applying this concept, different systems are designed, such as Sn-Fe-C,[38] Sn-Mn-C[39] or Si-C.[40] It has been proved that these kinds of anodes can improve the cycling and specific capacity in lithium cells. The Si-C nanocomposite has attracted interest because the specific capacity is over 1000 mAh/g for more than 100 cycles. After adding the inactive materials, the active materials avoid cracking.

Undoubtedly, nanomaterials contribute to the alloy reaction in lithium-ion batteries.[41]

1.5 Introduction to silicon

Silicon is the most abundant element in the earth's crust after oxygen.[42] Silicon is a chemical element with the symbol Si and the atomic number 14; it is a typical semiconductor with wide industry applications. Silicon atoms have four external electrons; compared with carbon, silicon is more stable and has lower activity. Silicon is a very common element, but it seldom exists in the form of an elemental. It exists in the form of complex silicate or silica and other compounds widely found in rock. In the list of cosmic reserves, silicon is the eighth. In the crust, it is the second richest element, accounting for 25.7% of the total crust, second only to the first – oxygen. Natural silicon contains 92.2% of the isotope 28, 4.7% of silicon 29 and 3.1% of silicon 30. Apart from those stable natural isotopes, various radioactive artificial isotopes are known. Elemental has the physical properties of metalloids, similar to germanium, situated under it in group IV of the periodic table. Silicon is an intrinsic semiconductor in its purest form, although the intensity of its semiconduction is highly increased by introducing small quantities of impurities. Silicon is like a metal in its chemical behaviour.[43] The four electrons that orbit the nucleus in the outermost or "valence" energy level are given to, accepted from or shared with other atoms, as shown in Figure 10. The electrons orbit the nucleus at different distances and this is determined by their energy level. For example, an electron with less energy orbits closer to the nucleus, whereas one with greater energy orbits further away. It is the electrons furthest away from the nucleus that interact with those of neighbouring atoms to determine the way that solid structures are formed.

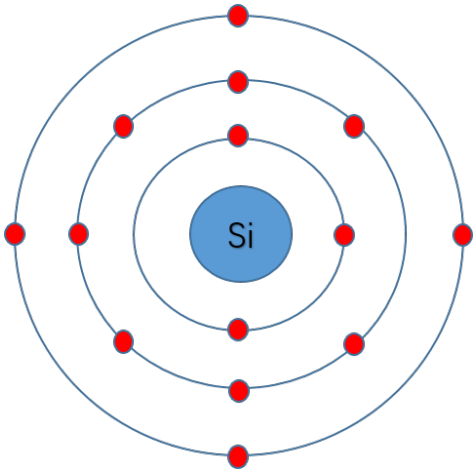

Figure 10. Silicon atomic structure.

Si has been proven to be a potential anode material for replacement of graphite or carbon anode in high-performance lithium-ion battery systems, with its low discharge potential and the highest known theoretical charge capacity, which is up to 4200 mAhg-1.[44] The higher energy capacity makes silicon an attractive material for application in portable electronic devices,[17] EVs and implantable medical devices.[45, 46]

Because of the abundance of silicon and its outstanding capacity, a great deal of attention has been given to using silicon as a lithium-ion battery cell anode material. However, the alloying process of Li and Si was found to be less reversible at room temperature.[47, 48] Micro-scaled silicon has been researched as an anode material for lithium-ion batteries.[49] In the initial cycle, the charge capacity of the bulk silicon anode exceeds 3260 mAh g^{-1}, and the discharge capacity is close to 1170 mAh g^{-1}, corresponding to a Coulomb efficiency of only 35%,[49] shown in Figure 11.

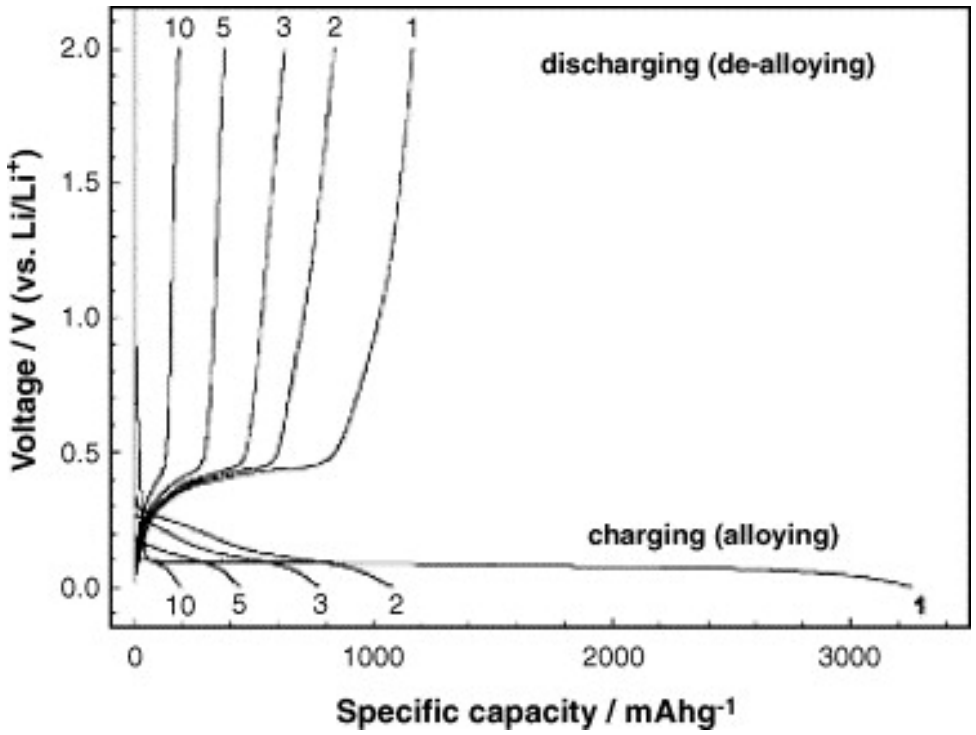

Figure 11. Galvanostatic charge-dischage data for micro-Si (10 µm).[49]

After further cycling, it has been observed that capacity fades after the 5th cycle. The insertion of Li into Si results in a large volume expansion. Figure 11 shows the data for crystal structure, unit cell volume and volume per Si atom for the Li-Si system. From this table, it can be observed that the volume per silicon atom for $Li_{22}Si_5$ is four times higher than the original Si. This can lead to pollution and disintegration of the electrode, and the loss of active material through reduced electronic contact, thereby severely reducing capacity. Although it was initially believed that the low-coulombic efficiency of the bulk Si anode was due to the low alloying process of Li with Si at room temperature, research showed that during the insertion of Li, the poor electronic contacts caused by the huge volume expansion is the real reason for the loss of capacity. The silicon anode shows a huge volume change during charging and discharging. Table 1 and Figure 12 show that lithium insertion during the alloying process will result in the Li_xSi alloy, which has a much larger volume than nanostructured Si.

Table 1. Crystal structure, unit cell volume and volume per Si atom for the Li-Si system

Compound and crystal structure	Unit cell volume	Volume per silicone atom
Silicon cubic	160.2	20.0
$Li_{12}Si_7$	243.6	58.0
$Li_{14}Si_6$	308.9	51.5
$Li_{13}Si_4$	538.4	67.3
$Li_{22}Si_5$	659.2	82.4
Data source: Boukamp *et al*.[50]		

In order to overcome large volume changes to obtain better silicon anode capacity retention and cycle life, various methods have been used. They can be divided into the various methods of preparing silicon anodes reported in the literature:

(i) Nanoscale silicon powder anode
(ii) Si dispersed in an inactive material
(iii) Si dispersed in an active material
(iv) Si anodes with a different binder in lithium-ion cell

Methods ii and iii are popular; they mix Si with an active or inactive material. The more active material will react with lithium first, and the inactive material will play the role of limiting the volume change in this process, as mentioned before in this thesis. In this project, nanoscale silicon anode was focused on as a way to overcome the volume change during charge-discharge.

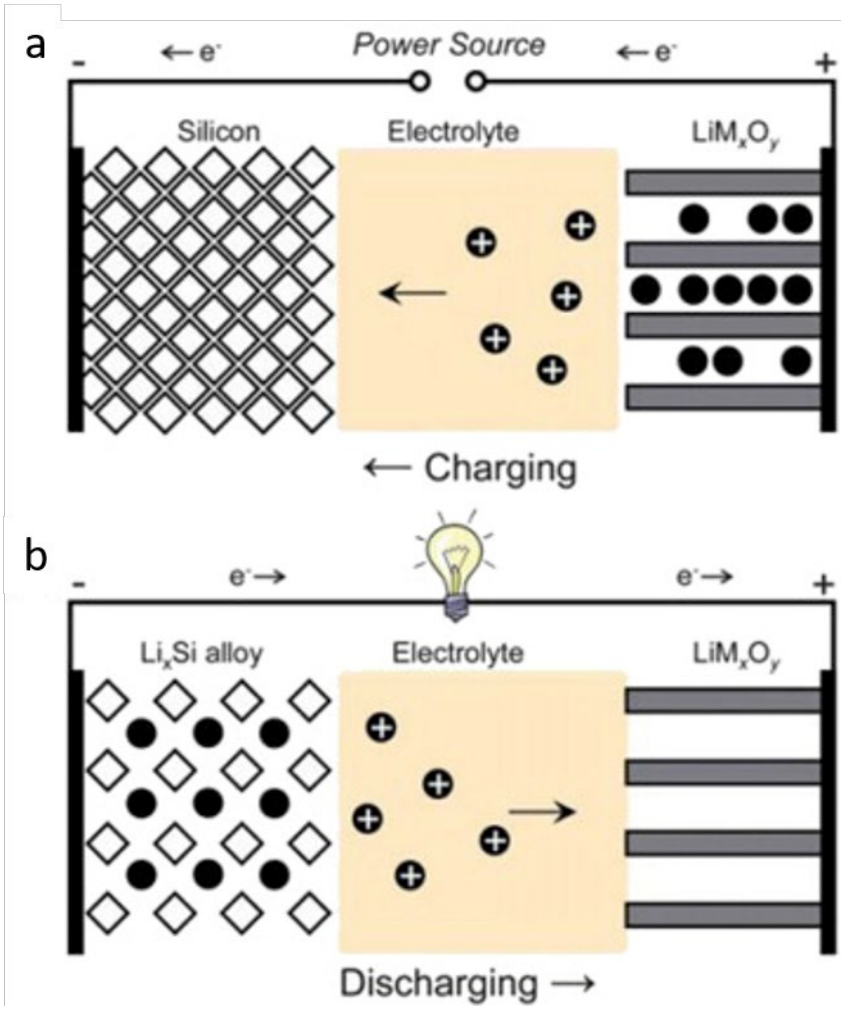

Figure 12. Schematic of a lithium battery containing a Si anode and lithium-based cathode during charging (a) and discharging (b).[51]

Nanostructured silicon has been researched for several years. Many types of nanostructured silicon materials have been researched for application in lithium-ion batteries, such as nanowire,[31] nanotube,[52] nanofilm,[53] three-dimension, solid core-shell structured, hollow core-shell structured,[54] etc.

1.6 Background of biomass silicon material

Silicon has shown a great improvement in stability when used in a nanocomposite for lithium-ion batteries. However, due to the high cost of pure silicon nanoparticles and the difficulties of size control during synthesis. SiO_2 comes into consideration with the advantage of low discharge potential,[55] low cost and favourable availability. It is regarded as an alternative material to replace the high-cost pure silicon.[56] The theoretical specific capacity of SiO_2 is lower than that of Si, but it still has a remarkable specific capacity of 1965 mAh/g, which is approximately five times

higher than that of commercial graphite. This material can be chosen as an anode material for lithium-ion batteries. However, SiO_2 has the same the challenging problem as Si, which is the dramatic volume change during lithium-ion insertion and desertion reaction. Besides this disadvantage, SiO_2 has poor electronic conductivity.[57, 58] Therefore, carbon could be most suitable material with its excellent mechanical elasticity and intrinsic conductivity[59, 60] To reduce the volume change of electrode materials and improve the electronic conductivity of SiO_2 , a composite of SiO_2/C could be used.[61, 62]

As mentioned before, silicon is the second richest element after oxygen on the earth.[42] All plants and animals may be impacted by this element. Although silicon is not recognised as an essential element for plants,[63] the effects of silicon have been observed in many.[64]

Rice husks are composed of SiO_2, organic carbon and metal oxides.[65-67] Silicon plays an important role in rice growth. It can save water and nutrition, and also prevent rice from being attacked by insects and bateria.[68-71] The rice husk develops nanoscale particles and tightly unifies with the organic carbon through natural evolution.[71, 72] However, there are other elements and the distribution between SiO_2 particles and the carbon component is inhomogeneous. The ball milling process is designed to improve the dispersion between SiO_2 and the carbon component, and also to reduce the size of SiO_2 particles, which would help improve the poor electric conductivity of SiO_2.

Table 2. Average content of dry silicon in some foods.

Food	Si (mg/100g)
Cereal	12.25
Oat bran	23.36
Porridge oats	11.39
Data sourced from Powell *et al.*[73]	

SiO_2 has been shown to be prevalent in the husks of grains, including barley, wheat bran, oats and rich bran. [74, 75] The average amount of dry silicon in some foods is shown in Table 2.

Bananas have 5.44 mg of silicon per 100g portion, but only around 5% is bioavailable.[76]

Silicon is also found in beer and brewing, which utilise barley.[77] Barley has a similar structure and content to rice. After the barley is processed, the barley husk is wasted, which is about 20% of the barley. Elementary analysis shows that around 0.4% of barley husk is silicon, as shown in Figure 13.[78] The major contents are carbon and oxygen, then silicon. That is perfect for this design. Barley husk has the potential to be the original material to produce a silicon-based anode material.

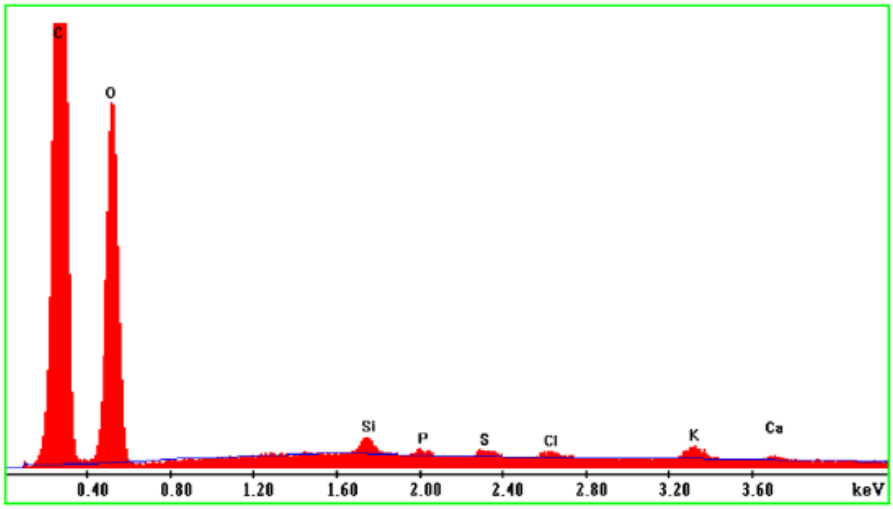

Figure 13. Elementary analysis of barley husk.[78]

1.7 References

1. Dunn, B.; Kamath, H.; Tarascon, J. M., Electrical Energy Storage for the Grid: A Battery of Choices. *Science* **2011,** *334* (6058), 928-935.

2. *Electrical energy storage technology options*; Electric Power Research Institute, Palo Alto, CA: 2010.

3. Granada-Echeverri, M.; Cubides, L. C.; Bustamante, J. O., The electric vehicle routing problem with backhauls. *International Journal of Industrial Engineering Computations* **2020**, 131-152.

4. Talbot, J. A. P., Charged up: the history and development of batteries. https://theconversation.com/charged-up-the-history-and-development-of-batteries-40372 (accessed 19/01/2021)

5. List of battery sizes. https://en.wikipedia.org/wiki/List_of_battery_sizes#/media/File:Button_cells_and_9v_cells_(3).png (accessed 31/05/2020).

6. Igharo, K. O., Construction of a Primary Dry Cell Battery From Cassava Juice Extracts (The Cassava Battery Cell). *Journal of Educational and Social Research* **2012,** *2 (8)*, 18-23.

7. Palacín, M. R., Recent advances in rechargeable battery materials: a chemist's perspective. *Chemical Society reviews* **2009,** *38*, 2565-2575.

8. Pavlov, D.; Pavlov, D., Chapter 1 – Invention and Development of the Lead–Acid Battery. In *Lead-Acid Batteries: Science and Technology*, 2011; pp 3-28.

9. Baay, D. M., Nickel-cadmium batteries. *Electronic Products (Garden City, New York)* **1988,** *31*, 1-15.

10. Energizer, Nickel Metal Hydride (NiMH). *Handbook and Application Manual* **2010,** *7323*, 1-16.

11. Fergus, J. W., Recent developments in cathode materials for lithium ion batteries. *Journal of Power Sources* **2010,** *195*, 939-954.

12. Troiani, J., How do Lithium Ion Batteries Work? A Nanotechnology Explainer. **2013**.

13. Ozawa, K., Lithium-ion rechargeable batteries with LiCoO2 and carbon electrodes: the LiCoO2/C system. *Solid State Ionics* **1994,** *69*, 212-221.

14. Armand, M.; Tarascon, J. M., Building better batteries. *Nature* **2008,** *451*, 652.

15. Tarascon, J. M.; Armand, M., Issues and challenges facing rechargeable lithium batteries. *Nature* **2001,** *414* (6861), 359-367.

16. Kang, B.; Ceder, G., Battery materials for ultrafast charging and discharging. *Nature* **2009,** *458*, 190.

17. Whittingham, M. S., Lithium Batteries and Cathode Materials. *Chemical Reviews* **2004,** *104* (10), 4271-4302.

18. Goodenough, J. B.; Kim, Y., Challenges for Rechargeable Li Batteries. *Chemistry of Materials* **2010,** *22* (3), 587-603.

19. Yong, J. Y.; Ramachandaramurthy, V. K.; Tan, K. M.; Mithulananthan, N., A review on the state-of-the-art technologies of electric vehicle, its impacts and prospects. *Renewable and Sustainable Energy Reviews* **2015,** *49*, 365-385.

20. Shareef, H.; Islam, M. M.; Mohamed, A., A review of the stage-of-the-art charging technologies, placement methodologies, and impacts of electric vehicles. *Renewable and Sustainable Energy Reviews* **2016,** *64*, 403-420.

21. Herrmann, F.; Rothfuss, F., 1 - Introduction to hybrid electric vehicles, battery electric vehicles, and off-road electric vehicles. In *Advances in Battery Technologies for Electric Vehicles*, Scrosati, B.; Garche, J.; Tillmetz, W., Eds. Woodhead Publishing: 2015; pp 3-16.

22. Daud, M. Z.; Mohamed, A.; Hannan, M. A., An improved control method of battery energy storage system for hourly dispatch of photovoltaic power sources. *Energy Conversion and Management* **2013,** *73*, 256-270.

23. Manzetti, S.; Mariasiu, F., Electric vehicle battery technologies: From present state to future systems. *Renewable and Sustainable Energy Reviews* **2015,** *51*, 1004-1012.

24. Rao, Z.; Wang, S.; Zhang, G., Simulation and experiment of thermal energy management with phase change material for ageing LiFePO4 power battery. *Energy Conversion and Management* **2011,** *52* (12), 3408-3414.

25. Saw, L. H.; Ye, Y.; Tay, A. A. O., Integration issues of lithium-ion battery into electric vehicles battery pack. *Journal of Cleaner Production* **2016,** *113*, 1032-1045.

26. Scrosati, B.; Garche, J., Lithium batteries: Status, prospects and future. *J. Power Sources* **2010,** *195* (9), 2419-2430.

27. Speirs, J.; Contestabile, M.; Houari, Y.; Gross, R., The future of lithium availability for electric vehicle batteries. *Renewable and Sustainable Energy Reviews* **2014,** *35*, 183-193.

28. Balakrishnan, P. G.; Ramesh, R.; Prem Kumar, T., Safety mechanisms in lithium-ion batteries. *Journal of Power Sources* **2006,** *155*, 401-414.

29. Chan, C. K.; Peng, H.; Liu, G.; McIlwrath, K.; Zhang, X. F.; Huggins, R. A.; Cui, Y., High-performance lithium battery anodes using silicon nanowires. *Nature Nanotechnology* **2007,** *3*, 31.

30. Poizot, P.; Laruelle, S.; Grugeon, S.; Dupont, L.; Tarascon, J. M., Nano-sized transition-metal oxides as negative-electrode materials for lithium-ion batteries. *Nature* **2000,** *407* (6803), 496-499.

31. P. Atkins, T. O., J. Rourke, M. Weller and F. Armstron, *Inorganic Chemistry*. Oxford University Press: 2010; Vol. 5th edn.

32. A. I. Ekimov and A. A. Onuschenko, *J. Exp. Theor. Phys. Lett*. 1981.

33. I. Freestone, N. M., M. Sax and C. Higgitt, *Gold Bull* **2007,** *40*, 270-277.

34. T. Pradell, J. M., A. Smith and M. Tite,, *J. Archaeol. Sci*. 2008.

35. Winter, M.; Besenhard, J. O., Electrochemical lithiation of tin and tin-based intermetallics and composites. *Electrochim. Acta* **1999,** *45* (1), 31-50.

36. Mao, O., Mechanically Alloyed Sn-Fe(-C) Powders as Anode Materials for Li-Ion Batteries: III. Sn[sub 2]Fe:SnFe[sub 3]C Active/Inactive Composites. *J. Electrochem. Soc.* **1999,** *146* (2), 423.

37. Beaulieu, L. Y.; Dahn, J. R., The Reaction of Lithium with Sn-Mn-C Intermetallics Prepared by Mechanical Alloying. *J. Electrochem. Soc.* **2000,** *147* (9), 3237.

38. J. Graetz, z. C. C. A., R. Yazami, and B. Fultz, Highly Reversible Lithium Storage in Nanostructured Silicon. *Electrochemical and Solid-State Letters* **2003,** *6*, A194-A197.

39. Aricò, A. S.; Bruce, P.; Scrosati, B.; Tarascon, J.-M.; van Schalkwijk, W., Nanostructured materials for advanced energy conversion and storage devices. *Nature Materials* **2005,** *4* (5), 366-377.

40. Feng Ma, J.; Higashitani, A.; Sato, K.; Takeda, K., Genotypic variation in silicon concentration of barley grain. *Plant and Soil* **2003,** *249* (2), 383-387.

41. Lenntech.

42. Boukamp, B. A.; Lesh, G. C.; Huggins, R. A., ALL-SOLID LITHIUM ELECTRODES WITH MIXED-CONDUCTOR MATRIX. *J. Electrochem. Soc.* **1981,** *128* (4), 725-729.

43. Bock, D. C.; Marschilok, A. C.; Takeuchi, K. J.; Takeuchi, E. S., Batteries used to power implantable biomedical devices. *Electrochim. Acta* **2012,** *84*, 155-164.

44. Hu, C.; Ye, H.; Jain, G.; Schmidt, C., Remaining useful life assessment of lithium-ion batteries in implantable medical devices. *J. Power Sources* **2018,** *375*, 118-130.

45. Kim, J. W.; Ryu, J. H.; Lee, K. T.; Oh, S. M., Improvement of silicon powder negative electrodes by copper electroless deposition for lithium secondary batteries. *J. Power Sources* **2005,** *147* (1), 227-233.

46. Weydanz, W. J.; Wohlfahrt-Mehrens, M.; Huggins, R. A., A room temperature study of the binary lithium–silicon and the ternary lithium–chromium–silicon system for use in rechargeable lithium batteries. *J. Power Sources* **1999,** *81-82*, 237-242.

47. Ryu, J. H.; Kim, J. W.; Sung, Y.-E.; Oh, S. M., Failure Modes of Silicon Powder Negative Electrode in Lithium Secondary Batteries. *Electrochemical and Solid-State Letters* **2004,** *7* (10), A306.

48. Boukamp, B. A., All-Solid Lithium Electrodes with Mixed-Conductor Matrix. *J. Electrochem. Soc.* **1981,** *128* (4), 725.

49. Liang, B.; Liu, Y.; Xu, Y., Silicon-based materials as high capacity anodes for next generation lithium ion batteries. *J. Power Sources* **2014,** *267*, 469-490.

50. Wu, H.; Chan, G.; Choi, J. W.; Ryu, I.; Yao, Y.; McDowell, M. T.; Lee, S. W.; Jackson, A.; Yang, Y.; Hu, L.; Cui, Y., Stable cycling of double-walled silicon nanotube battery anodes through solid–electrolyte interphase control. *Nature Nanotechnology* **2012,** *7*, 310.

51. Jung, H.; Park, M.; Han, S. H.; Lim, H.; Joo, S. K., Amorphous silicon thin-film negative electrode prepared by low pressure chemical vapor deposition for lithium-ion batteries. *Solid State Communications* **2003,** *125*, 387-390.

52. Liu, N.; Wu, H.; Mcdowell, M. T.; Yao, Y.; Wang, C.; Cui, Y., A Yolk-Shell Design for Stabilized and Scalable Li-Ion Battery Alloy Anodes. **2012**.

53. Liang, Y.; Cai, L.; Chen, L.; Lin, X.; Fu, R.; Zhang, M.; Wu, D., Silica nanonetwork confined in nitrogen-doped ordered mesoporous carbon framework for high-performance lithium-ion battery anodes. *Nanoscale* **2015,** *7* (9), 3971-3975.

54. Feng, Y.; Liu, X.; Liu, L.; Zhang, Z.; Teng, Y.; Yu, D.; Sui, J.; Wang, X., SiO2/C Composite Derived from Rice Husks with Enhanced Capacity as Anodes for Lithium-Ion Batteries. *ChemistrySelect* **2018,** *3* (37), 10338-10344.

55. Li, W.; Wang, F.; Ma, M.; Zhou, J.; Liu, Y.; Chen, Y., Preparation of SiO2 nanowire arrays as anode material with enhanced lithium storage performance. *RSC Advances* **2018,** *8* (59), 33652-33658.

56. Wang, H.; Wu, P.; Qu, M.; Si, L.; Tang, Y.; Zhou, Y.; Lu, T., Highly Reversible and Fast Lithium Storage in Graphene-Wrapped SiO2 Nanotube Network. *ChemElectroChem* **2015,** *2* (4), 508-511.

57. Wu, L.; Yang, J.; Zhou, X.; Tang, J.; Ren, Y.; Nie, Y., Enhanced Electrochemical Performance of Heterogeneous Si/MoSi2 Anodes Prepared by a Magnesiothermic Reduction. *ACS Applied Materials & Interfaces* **2016,** *8* (26), 16862-16868.

58. Wang, G.; Shen, X.; Yao, J.; Park, J., Graphene nanosheets for enhanced lithium storage in lithium ion batteries. *Carbon* **2009,** *47* (8), 2049-2053.

59. Cao, X.; Chuan, X.; Massé, R. C.; Huang, D.; Li, S.; Cao, G., A three layer design with mesoporous silica encapsulated by a carbon core and shell for high energy lithium ion battery anodes. *Journal of Materials Chemistry A* **2015,** *3* (45), 22739-22749.

60. Yan, N.; Wang, F.; Zhong, H.; Li, Y.; Wang, Y.; Hu, L.; Chen, Q., Hollow Porous SiO2 Nanocubes Towards High-performance Anodes for Lithium-ion Batteries. *Scientific Reports* **2013,** *3* (1), 1568.

61. Epstein, E., *Mineral nutrition of plants: principles and perspectives*. 1972; p 412pp.

62. Ma J F, M. Y. a. T., *Silicon in Agriculture*. 1 ed.; 2001.

63. Li, M.; Yu, Y.; Li, J.; Chen, B.; Wu, X.; Tian, Y.; Chen, P., Nanosilica/carbon composite spheres as anodes in Li-ion batteries with excellent cycle stability. *Journal of Materials Chemistry A* **2015,** *3* (4), 1476-1482.

64. Wang, L.; Xue, J.; Gao, B.; Gao, P.; Mou, C.; Li, J., Rice husk derived carbon–silica composites as anodes for lithium ion batteries. *RSC Advances* **2014,** *4* (110), 64744-64746.

65. Wang, W.; Martin, J. C.; Fan, X.; Han, A.; Luo, Z.; Sun, L., Silica Nanoparticles and Frameworks from Rice Husk Biomass. *ACS Applied Materials & Interfaces* **2012,** *4* (2), 977-981.

66. Gao, B.; Sinha, S.; Fleming, L.; Zhou, O., Alloy Formation in Nanostructured Silicon. *Advanced Materials* **2001,** *13* (11), 816-819.

67. Genieva, S.; Turmanova, S.; Dimitrova, A.; Vlaev, L., Characterization of rice husks and the products of its thermal degradation in air or nitrogen atmosphere. *Journal of Thermal Analysis and Calorimetry* **2008,** *93*, 387-396.

68. Stefani, P. M.; Garcia, D.; Lopez, J.; Jimenez, A., Thermogravimetric analysis of composites obtained from sintering of rice husk-scrap tire mixtures. *Journal of Thermal Analysis and Calorimetry* **2005,** *81* (2), 315-320.

69. Maiti, S.; Dey, S.; Purakayastha, S.; Ghosh, B., Physical and thermochemical characterization of rice husk char as a potential biomass energy source. *Bioresource Technology* **2006,** *97* (16), 2065-2070.

70. Cho, W. C.; Kim, H. J.; Lee, H. I.; Seo, M. W.; Ra, H. W.; Yoon, S. J.; Mun, T. Y.; Kim, Y. K.; Kim, J. H.; Kim, B. H.; Kook, J. W.; Yoo, C.-Y.; Lee, J. G.; Choi, J. W., 5L-Scale Magnesio-Milling Reduction of Nanostructured SiO2 for High Capacity Silicon Anodes in Lithium-Ion Batteries. *Nano Letters* **2016,** *16* (11), 7261-7269.

71. Schwarz, K.; Milne, D. B., Growth-promoting Effects of Silicon in Rats. *Nature* **1972,** *239* (5371), 333-334.

72. Pennington, J. A. T., Silicon in foods and diets. *Food Additives & Contaminants* **1991,** *8* (1), 97-118.

73. Powell, J. J.; McNaughton, S. A.; Jugdaohsingh, R.; Anderson, S. H. C.; Dear, J.; Khot, F.; Mowatt, L.; Gleason, K. L.; Sykes, M.; Thompson, R. P. H.; Bolton-Smith, C.; Hodson, M. J., A provisional database for the silicon content of foods in the United Kingdom. *British Journal of Nutrition* **2005,** *94* (5), 804-812.

74. Jugdaohsingh, R.; Anderson, S. H.; Tucker, K. L.; Elliott, H.; Kiel, D. P.; Thompson, R. P.; Powell, J. J., Dietary silicon intake and absorption. *The American Journal of Clinical Nutrition* **2002,** *75* (5), 887-893.

75. Casey, T. R.; Bamforth, C. W., Silicon in beer and brewing. *Journal of the Science of Food and Agriculture* **2010**, n/a-n/a.

76. Bledzki, A. K.; Mamun, A. A.; Volk, J., Barley husk and coconut shell reinforced polypropylene composites: The effect of fibre physical, chemical and surface properties. *Composites Science and Technology* **2010,** *70* (5), 840-846.

Chapter 2: Experimental detail

This chapter describes the instrument for this project and the techniques used to analyse the sample, such as muon spin spectroscopy, Fourier Transform Infrared Spectroscope, Energy Dispersive X-ray Spectroscopy, X-ray Photoelectron Spectroscopy, X-ray Powder Diffraction, Scanning Electron Microscope, Transmission Electron Microscope, Ultraviolet-Visible/Photoluminescence Spectroscopy, Dynamic Light Scattering and Thermal Gravimetric Analyse/ differential scanning calorimetry. The preparation for muon spin spectroscopy is also included in this chapter.

Contents

2.1 Chemical Analysis

2.1.1 Fourier Transform Infrared Spectroscopy

Fourier Transform Infrared Spectroscopy (FTIR) is useful for identifying functionalised silicon nanoparticles shown in Figure 15. It can produce an infrared absorption spectrum to identify the type of chemical bond. The ligands attached to the silicon nanoparticles can be identified. Here, FTIR measurement was carried out with a Perkin-Elmer Spectrum 100 ATR FTIR spectrometer. A blank crystal was recorded as the initial background. The scan range is between 4000 and 600 cm^{-1}.

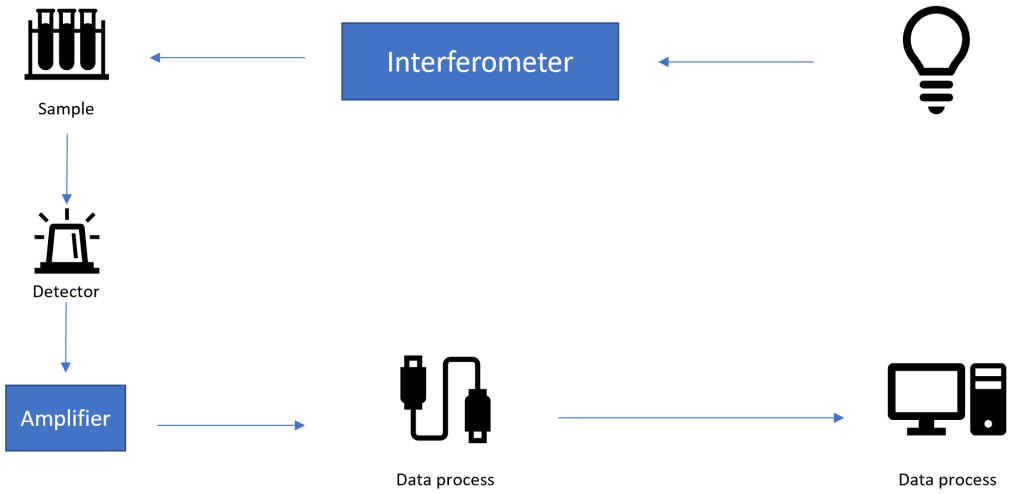

Figure 14. Schematic diagram of Fourier Transform Infrared (FTIR) Spectroscopy.[1]

Electromagnetic radiation that interacts with a substance can be absorbed, transmitted, reflected, scattered or have photoluminescence (PL). This provides significant information on the molecular structure and the energy level transition of that substance.[1-3]

2.1.2 Energy Dispersive X-ray Spectroscopy

Energy Dispersive X-ray Spectroscopy (EDX) is commonly employed for the elemental component analysis of material surfaces. A high-energy electron beam is used to eject electrons from the energy levels bounded by the nucleus of an atom. The energy of the photon emitted is detected by the detector when electrons transfer from the outer energy levels to the vacant inner levels. The emitted energy of the X-ray is a unique parameter of the energy difference between the two levels, and the

structure of the elements. The elemental composition can be obtained.[82] However, this technique is not sensitive enough for atomic ratios, so the data obtained from this technique is generally indicative.

EDX analysis was run by using a JOEL Scanning Electron Microscope (SEM) machine with an EDX detector attached. Points of interest can be selected from the spectrum and the EDX analysis can be performed individually for each spot selected. Materials were coated in gold as a reference for EDX. After gold coating, conduction away from the surface was allowed when observed under the SEM.

2.1.3 X-ray Photoelectron Spectroscopy

X-ray Photoelectron Spectroscopy (XPS) is a useful tool for analysing the elemental composition of the surface of materials. A source of x-ray radiation is used to irradiate the sample. The electrons would be ejected from the atom if their binding energy were less than that of the x-rays. There is an electron detector to measure the kinetic energy of these ejected electrons. The kinetic energy is related to the binding energy; they can be converted by the following equation:

$$E_k = hv - E_b - \emptyset \qquad (2.1)$$

Where Ek is the kinetic energy, hv is the photon energy, ϕ is the characteristic work function of the material and Eb is the binding energy of the electron to the atoms.[4] The photon was applied by a fixed-energy X-ray beam onto the surface of the sample and absorbed by the surface atom. The absorbance causes photo-ionisation of the atom and the emission of an inner shell electron. Then, the kinetic energy distribution of the photoelectrons can be measured by an analyser. This experiment needs an ultra-high-vacuum environment to make sure that the electrons emitted can be collected by the analyser without interacting with gas inside the chamber.

X-ray can distinguish different elements because each element has a unique binding energy that is relative to its own core orbitals. However, hydrogen and helium are not able to be detected by the X-ray source.

As the XPS is a surface analysis technique, the sample should be pressed into a pellet or mounted on a substrate. The pellet sample needs good electrical conductivity in order to keep a grounded connection, whereas the substrate for the mounted sample has to be made of different elements from the ones pending analysis.

The two different ways used to prepare the samples utilised a substrate. The first preparation was by drop casting dispersion of nanoparticles onto a pure gold foil. With gold having a specific elemental trace, unlike all the other elements in my sample, and as it is a good conductor, this substrate helped to obtain a spectrum without any interference. The second method was pressing the powder sample into indium foil. As the powder is unable to stick to the surface of a gold substrate, indium was used as it is a soft metal and this ensured the stability of the prepared sample ready for analysis.

XPS was performed at Harwell XPS, Romm G.63, Research Complex at Harwell (RCaH), Didcot.

2.1.4 X-ray Powder Diffraction

X-ray Powder Diffraction is a powerful method for analysing the structure of nanomaterials. The basic feature of X-ray Powder Diffraction is shown in Figure 15. The X-ray beam encounters the sample; most of the X-rays will destructively interfere with each other and cancel each other out, but in some specific directions, the X-ray beams interfere constructively and reinforce one another. It is these reinforced diffracted X-rays that produce the characteristic X-ray diffraction pattern that is used for crystal structure determination. Diffraction is widely used in chemistry for the characterisation of organic and inorganic areas.

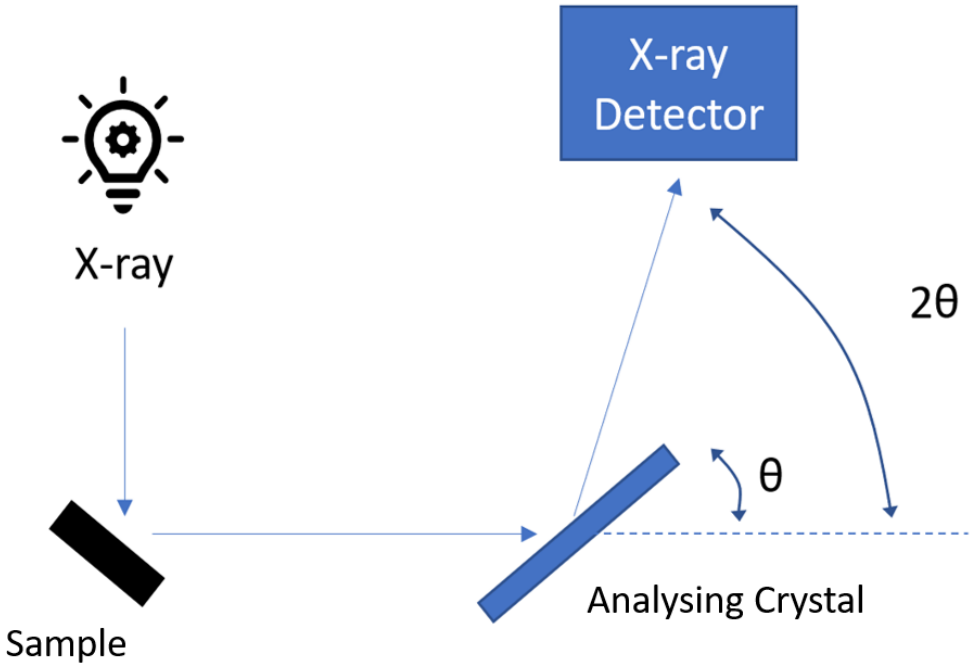

Figure 15. Schematic diagram of a diffractometer system[5]

XRD measurement was performed using Thermo Scientific ARL XTRA Powder Diffractometer.

2.2 Electron microscope

2.2.1 Scanning Electron Microscope

An SEM is designed for directly studying details of the surface of solid materials by tracing a sample in a raster pattern with an electron beam. The main SEM components include a source of electrons, a column down which electrons travel with electromagnetic lenses, an electron detector, a sample chamber and a computer to display the images. A beam of focused low-energy electrons is used as an electron probe that is scanned over the surface of the materials. The electron source and electromagnetic lenses, which is like the structure of a transmission electron microscope, generate and focus the beam.

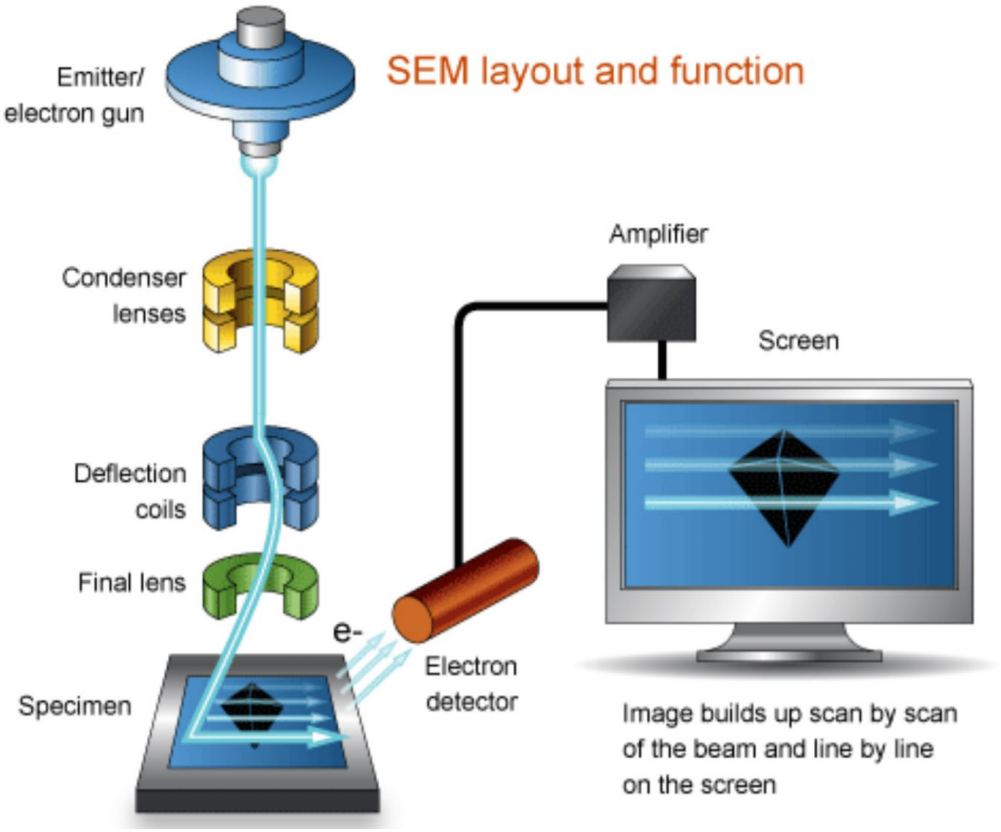

Figure 16. All SEM components[6]

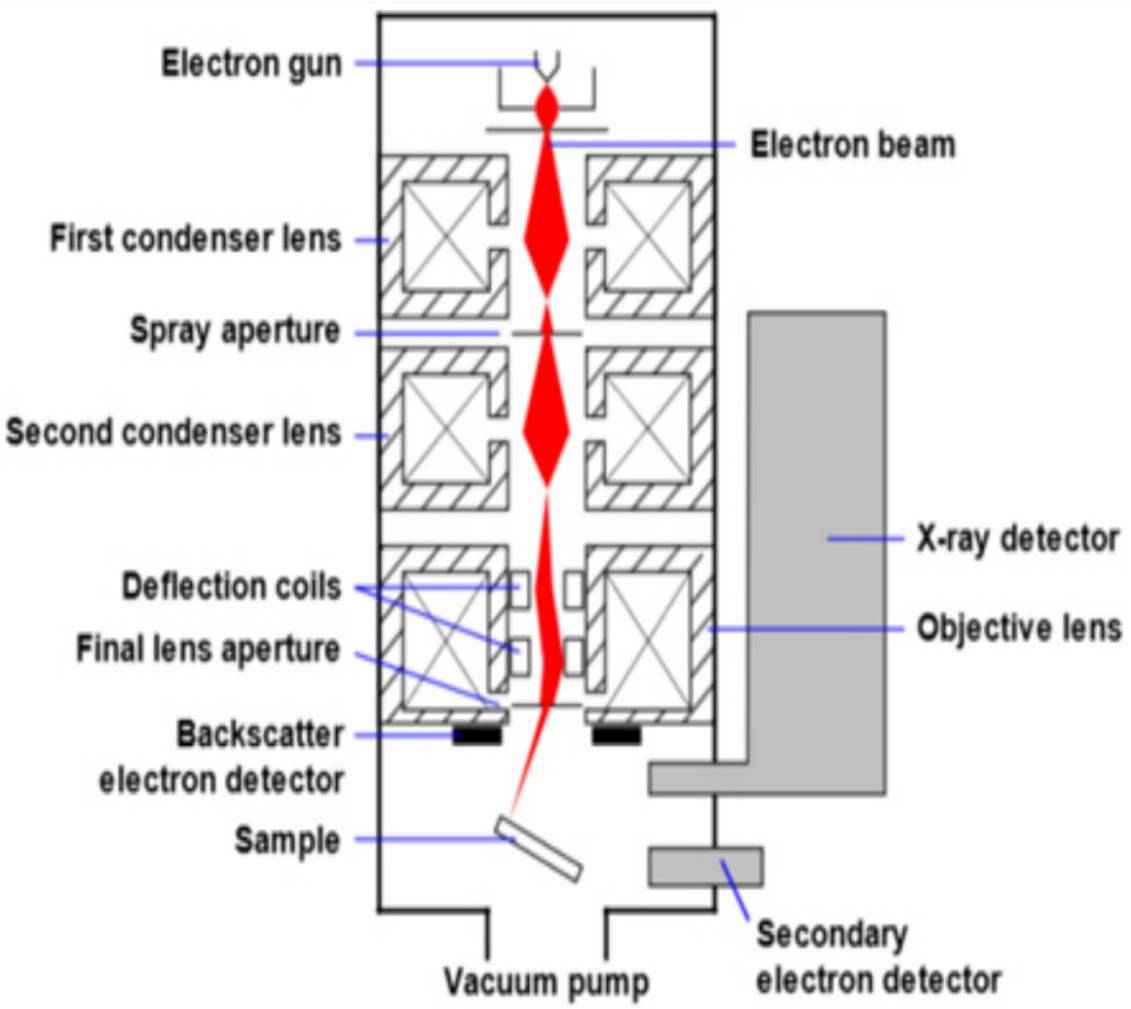

Figure 17. Schematic of scanning electron microscope[6]

SEM measurement was performed using JOEL scanning electron microscope. And the coating of gold was carried out in a Quorum Technologies gold coater CC7640.

2.2.2 Transmission Electron Microscope

A Transmission Electron Microscope (TEM) is a powerful tool that provides an atomic-resolution image, and has a similar structure to SEM. However, it can provide greater detail of the sample than SEM, such as crystallite size and structure. The chemical of a single nanocrystal could be identified directly.[7] TEM is composed of an illumination system, the object lens system, the magnification system, the data record system and the chemical analysis system. The electron gun, which uses a LaB_6 thermal emission source, is usually the most important part of the illumination system.

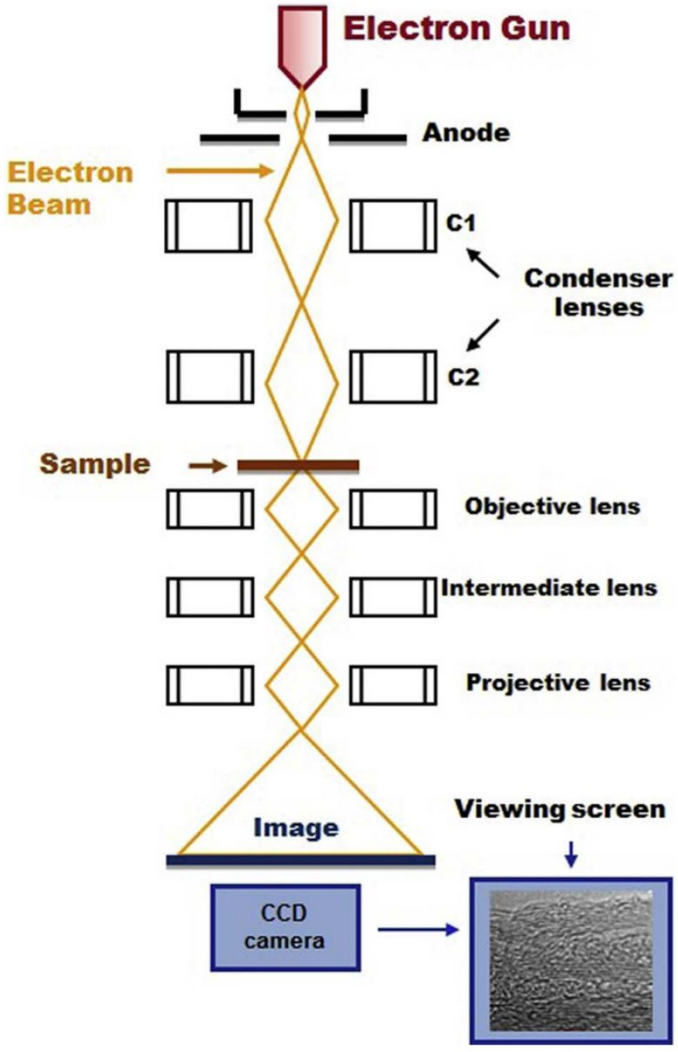

Figure 18. Structure of transmission electron microscope[8]

From Figure 18, it can be observed that the electron gun is the illumination source and it generates an electron beam which travels through the condenser lenses and hits the sample. The condenser lenses are used to control and transfer the beam into the specimen. After hitting the sample, there is an objective lens, an intermediate lens and a projective lens to collect and project the electrons that are not scattered by the sample. A CCD camera is placed at the end of the whole structure to transfer the signal from the electrons to the image. Electrons can pass through or be scattered by the specimen. The bright part shown in the image is the area where the electron beam is not scattered. The dark region is the area where the electrons are stoppered by the sample.

The sample needs to be prepared by dropping a dispersion of the material onto a grid and letting the solvent dry out completely. A thin layer of specimen outside the grid is used for a better-quality image.

2.3 Optical Properties

2.3.1 Ultraviolet-Visible Spectroscopy

Ultraviolet-Visible (UV-Vis) Spectroscopy is a method for measuring the optical absorbance of a substance with a common scan range of 200–800 nm in wavelength. The light generated by the UV light installed inside is absorbed by the molecule when the electronic excitation energy matches the wavelength of the light.

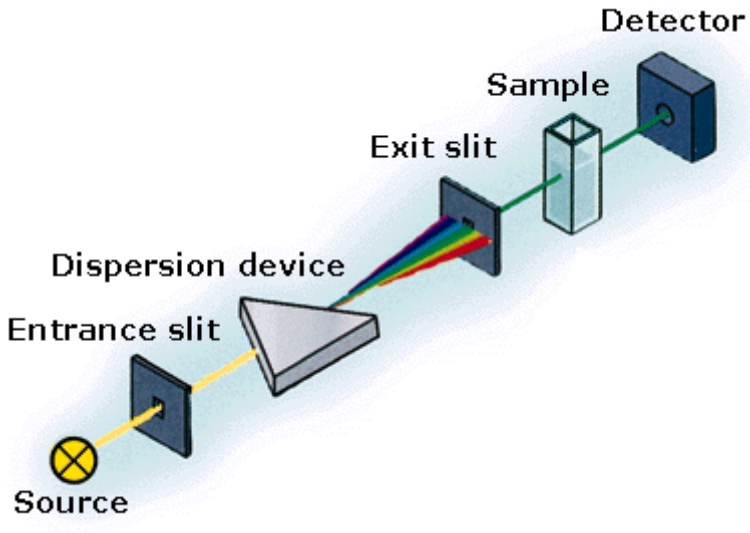

Figure 19. Structure of UV-Vis Spectroscopy[9]

From Figure 19, it can be observed that the light source transmits the light through the entrance slit first and it is then dispersed into different wavelengths of light at different angles. After the exit slit, the amount of light is selected to travel through the sample. The detector behind the sample will collect the signals from the different wavelengths and generate the UV-Vis spectrum. The light energy generated by the UV light installed inside is absorbed by the molecule when the electronic excitation energy matches the wavelength of the light. The spectrum presents this phenomenon as absorbance against wavelength to show the light energy absorbed by the molecule when the wavelength matches the electronic excitation energy. The absorbance of light energy is related to the number of molecules contained in the solution, so a correct property is required to make sure that the values obtained in different concentrations can be compared.

2.3.2 Photoluminescence Spectroscopy

Photoluminescence (PL) Spectroscopy is a measurement to collect and analyse the phonon emitted by the sample after an electron is excited by a light beam and absorbed. When phonons are absorbed, the electronic excitations are created. Finally, the excitations will relax and electrons will return to the ground state. If radiative relaxation happens, the light emitted is call PL. This measurement can be used to analyse the information about photoexcited material.

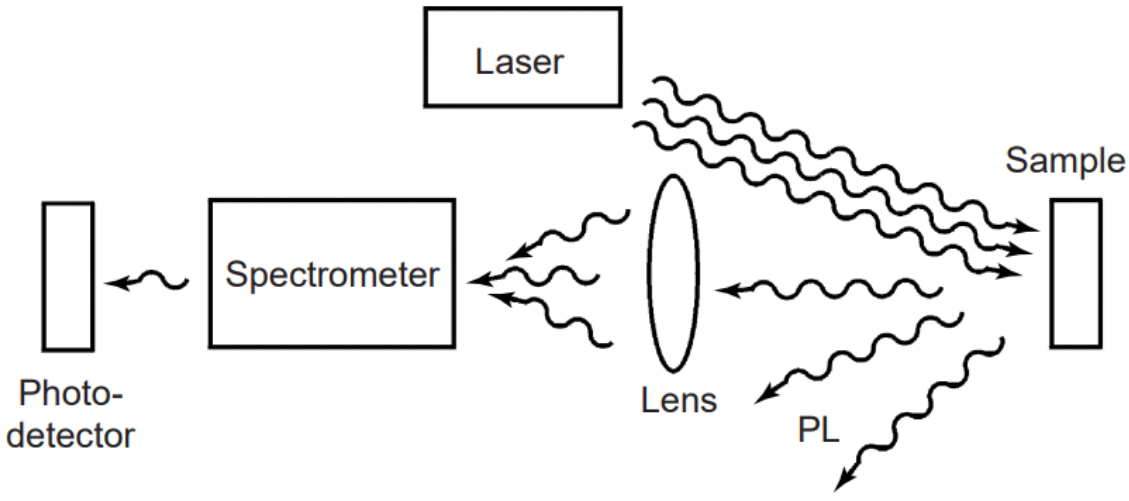

Figure 20. Typical experiment set-up for PL measurement[10]

From Figure 20, it can be observed that the light emitted by the laser hits the sample. Some phonons are absorbed by the electrons at the surface of the sample, and the electrons are excited to higher energy level. The excited-state electrons are unstable, and they will return to the ground state with the PL emitted. The PL travels through the lens and the spectrometer, and is finally collected by the photo detector.

2.3.3 Quantum yield

Quantum yield is the ratio of photons emitted to the photons absorbed in the photoluminescence process:

$$Q = \frac{photon_{em}}{photon_{abs}} \qquad (2.2)$$

The quantum yield requires specific hardware to measure it, but it is simpler to measure the relative quantum yield by comparing the sample to a selected reference with a known quantum yield. Two methods can be chosen to measure the relative quantum yield. The first one is analysing only one solution of fluorophore along with the reference with the same concentration as the sample. The quantum yield is calculated as:

$$Q = Q_R \frac{I}{I_R} \frac{A_R}{A} \left(\frac{n}{n_R}\right)^2 \qquad (2.3)$$

where Q is the quantum yield, Q_R is the quantum yield of the reference used, I is integrated fluorescence intensity, A is absorption, n is the refractive index of the solvent and subscript R refers to the reference used. This method needs less time and is easy to operate, but the result may be unreliable with inaccuracy. The other method requires several samples and reference solutions with a series of concentrations.[11] A slope will be obtained by fitting the line plotted for the integrated fluorescence intensities against the absorptions of the fluorophore solutions to calculate the quantum yield using the equation:

$$Q = Q_R \frac{m}{m_R} \left(\frac{n}{n_R}\right)^2 \qquad (2.4)$$

where Q is the quantum yield, Q_R is the quantum yield of the reference used, m is the slope, n is the refractive index and subscript R refers to the reference used. The plot can be linear only by keeping the absorption measured between 0.01 and 0.1.

The UV-Vis spectrophotometer and fluorescence spectrometer were utilised, along with a quartz cuvette.

2.3.4 Dynamic light scattering

Dynamic Light Scattering (DLS) is a method for measuring the size of particles. It emits a monochromatic light beam into a particle solution, and the light will scatter in all directions. The scattered light can be detected by the photomultiplier with the polariser on both sides of sample, shown in Figure 21. The particle size can be calculated using autocorrelation functions after determining the diffusion coefficient of the particles.

The result from DLS measurement is not as accurate as microscopy, but this measurement is a quick and easy way of checking the size of particle samples. If the sample is used in solution, this method is a good way to measure size, as well as the effect of particles on the surrounding solvent.

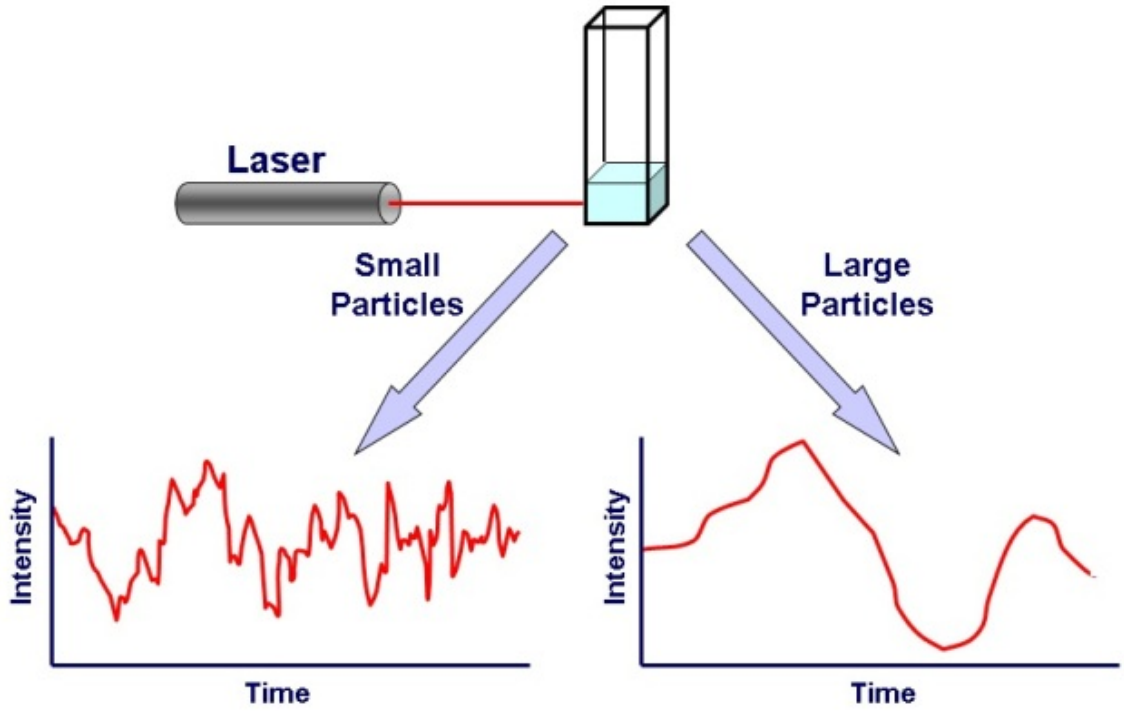

Figure 21. DLS measurements determine particle size from the pattern of intensity Fluctuations in scattered light[12]

DLS measurement was performed using Malvern Zetasizer Nano ZS. The sample was dissolved in solution and diluted to a low concentration contained in a quartz cuvette. A low concentration is helpful to avoid the temporary congregation of nanoparticles, and it also provides a better result for the measurement.

2.4 Thermal Gravimetric Analysis differential scanning calorimetry

Thermogravimetric analysis (TGA) and differential scanning calorimetry (DSC) are useful when considering the thermal stability of materials produced and how many ligands cover the silicon nanoparticles. TGA is a gravimetric trace that provides information about weight change over dynamic and isothermal heat programs. DSC gives images for the heat flow during the heat program running. The heat flow is related to an endothermic process. These two useful techniques can be used together to provide more information on the process shown in DSC.

TGA and DSC analysis was performed using a METTLER-TOLEDO TGA/DSC1. The solid sample was placed in a 40 µL aluminium pan and measurements were taken while heating the sample under the temperature limit set in the program. If the setting temperature was over the melting point of aluminium, a platinum pan was used. The background measurements were taken when running the empty pan with the sample temperature range and heating rate.

2.5 Muon spin spectroscopy

Muon is a powerful technique used for studying magnetic materials,[13] superconductors[14] and other functional materials.[15] It shows unique information about sample structure as the muon acts as a probe that can be implanted into and utilised for every material. Positive and negative muons are produced from the accelerator. The positive muon is important in chemical research; it is a decay product of positive pions, which has lifetime of 26 ns. The produced muon has a lifetime of 2.2 µs, ½ spin and 3.183 times larger magnetic moment than proton. The positive muon can pick up an electron and produce a neutral atom called Muonium ($Mu=\mu^{+}e^{-}$). The muon could be stopped in the specimen of interest, whether it is in a solid, liquid or gaseous state.

µSR is a powerful technique that has been used, for example, in investigations into magnetic materials,[16] superconductors,[17] functional materials[18] and energy

materials.[19] It is a technique that can provide unique information about sample structure and dynamics. In μSR experiments, the local magnetic field felt by the muon is estimated by monitoring the state of the muon spin. When organic radicals are present, this local magnetic field is dominated by the unpaired electron and the information obtained in the experiment reflects what happens to this electron. Therefore, μSR experiments are used to study properties such as the dynamics of molecules and radicals,[20] reaction rates and electron transfer/conduction.[21]

Avoided level crossing muon spin resonance (ALC-μSR) is a technique conducted in an external field along the direction of muon spin, monitoring the time-integrated asymmetry at the same time. The incoming muon goes through the window in the backward detector and is not detected. Only the decay positron is detected in the forward and backward detectors. The field is changed in small steps, and muon polarisation is scanned in each field range.

Transverse field muon spin rotation (TF-μSR) is a technique conducted in an external field applied transverse to the direction of muon spin. Each muon travels through a muon detector, which is a fast-electronic clock started by the detection of muon and stopped by the detection of positron by the one of the positron detectors.

Knowledge of the microscopic conduction rates and mechanisms of these materials would be of much use in our attempts to improve these materials by design. Muon spectroscopy appears to be an elegant method of measuring these microscopic properties, as illustrated by Pratt *et al.,*[22] for conducting organic polymers, materials which are structurally similar to the ligands found in our phenylacetylene functionalised SiNPs. Furthermore, muonium adducted to CC triple bonds in other organic compounds have already been characterised by our group.

In this work, Phenyl-SiNPs in solution state were investigated by both ALC- μSR and TF- μSR, while a model compound, tetrakis(2-phenylethynyl) silane, was employed as reference for comparison. Clear resonances were observed with interesting temperature effects including band broadening and shifting with temperature. In the case of the solution state of the model compound, there are eight possible sites of addition for muonium, creating the possibility of a large number of radicals. Therefore, a clear recognition of the radicals formed is essential for this study. For a complete identification of the prompt radicals formed by muonium addition, the muon-electron

hyperfine couplings in the model compound have been calculated. Together with the TF- μSR data this will provide a direct probe of electron transport in these materials.
The ALC-μSR measurements were undertaken using the high-field muon instrument (HIFI) spectrometer at the ISIS muon facility of the Rutherford Appleton Laboratory (RAL), Oxfordshire, UK.[23] while the TF data was measured using the GPD spectrometer at the Paul Scherrer Institute (PSI), Villigen, near Zurich, Switzerland.[24]

2.5.1 Sample preparation for muon spin experiment

Samples were redissolved in spectroscopic grade THF with concentrations of 200 mM for the model compound and 115 mg/ml for SiNPs, followed by at least three cycles of freeze-pump-thaw to remove O2 in the solution. For measurements at ISIS, the solutions were loaded into titanium sample cells (25 mm diameter) inside a glovebox degassed with an argon prepurge. The sample environment was provided by a closed cycle refrigerator cryostat. At PSI, a high momentum muon beam was available, and samples were sealed immediately after degassing in a glass sample holder, which was placed directly in a gas flow cryostat. In both experiments, the temperature range available for study was limited by the freezing and boiling points of the THF solvent.

The solution needs to be oxygen free by going through several rounds of the freeze-pump-thaw process because muon spectroscopy is sensitive to oxygen. Samples were dissolved in degassed THF. 15 ml of this solution was transferred into a custom-made 250 ml flask called a bulb. The bulb was connected to the freeze-pump-thaw and the solution was frozen using liquid nitrogen. After slowly opening the valve on the bulb, with the help of a roughing pump and a turbo pump, the pressure of the system was lowered to 10-6 mbar. Most of the oxygen inside the sample holder should already have been removed. However, some will still be trapped inside the frozen solution, especially compared to the existing high-vacuum state. With the valve sealed, the solution was heated by a heat gun to let the gas out from the solution. After several rounds of freezing, pumping and warming up, the solution sample was degassed and oxygen-free. Afterwards, the solution was transferred into a HIFI sample holder, shown in Figure 22 inside a glovebox. The sample holder was totally filled up and sealed before mounting.

Figure 22. Sample holder for solution state PA-SiNPs

After oxygen-free solution state sample preparation, the sample hold was inserted into a HIFI at ISIS, shown in Figure 23.

The magnet is a 5T superconducting split-pair, with high field homogeneity over the sample volume and actively compensated stray field. The dilution fridge can set the sample environment from 30 mk to 300 K and the reflector furnace can heat from 300 K to 1500 K. HIFI can give access to more level crossing resonances, many of which are in the 0.5 to 2 T range, for the spectroscopy and molecular dynamics studies.

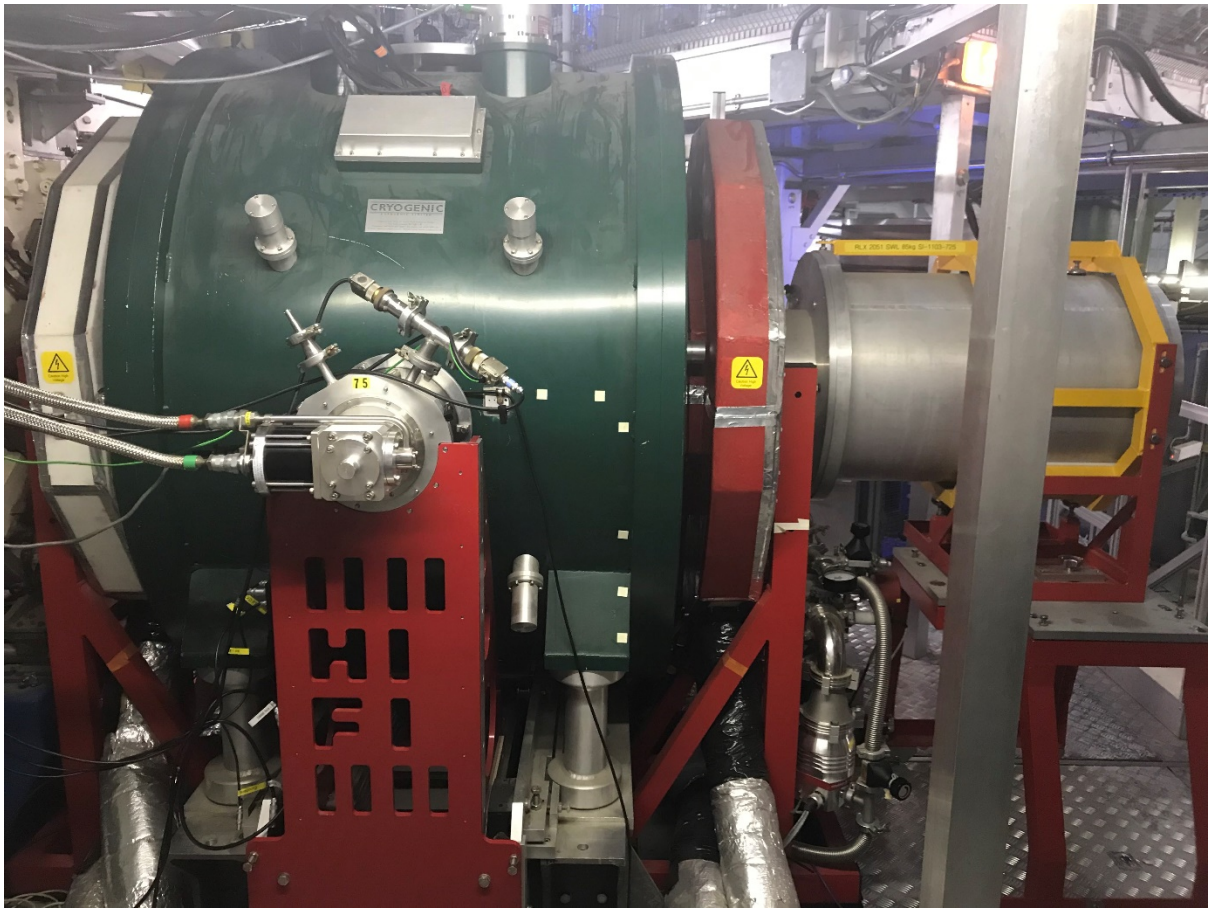

Figure 23. HIFI instrument in ISIS

For the transverse field result, the sample was measured in the GPD at PSI. A 3D view of the GPD instrument at PSI is shown in Figure 24.

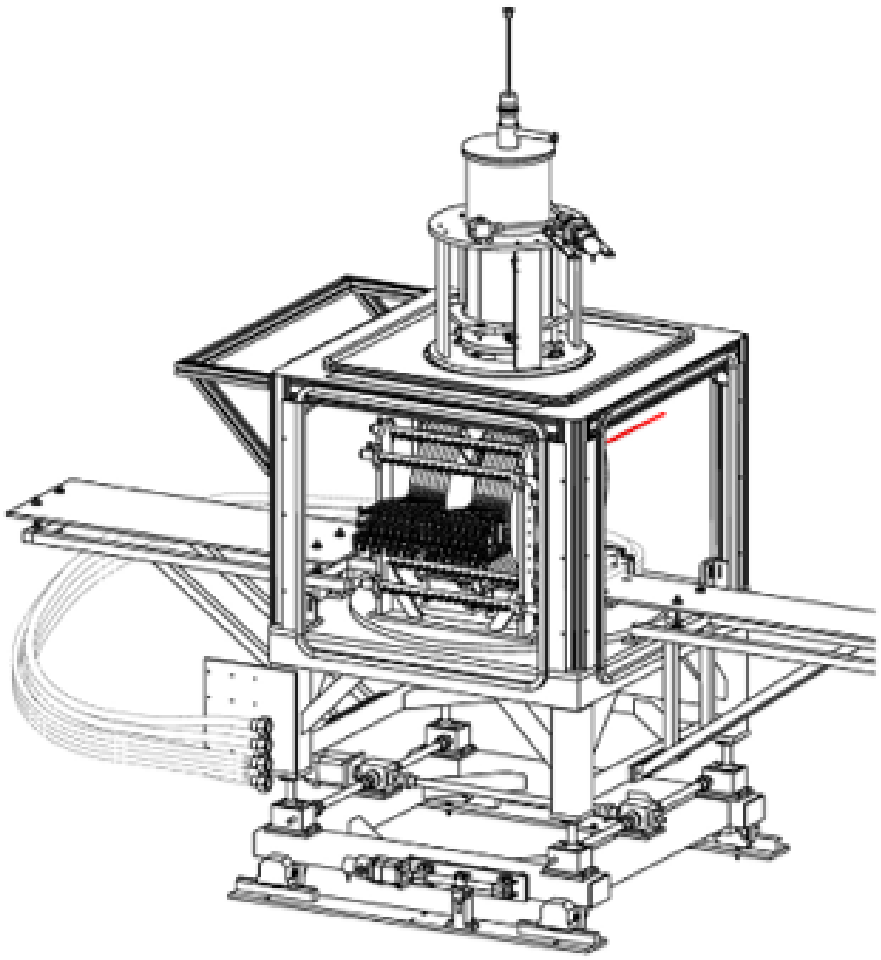

Figure 24. 3D view of GPD instrument at PSI[101]

All Gaussian fitting to the lines shown in the figures in Chapter 4 was performed using the Mantid analysis software.[25]

2.5.2 Computer simulations

Computer simulations were used for identifying and interpreting the data measured for radicals formed by muonium addition. The muon stopping sites in both the model compound and the Phenyl-SiNPs were studied using Density Functional Tight Binding (DFTB) calculations, as implemented in the DFTB+ code,[26] and standard DFT calculations, as implemented in the CASTEP code (see supplementary information).[27] The combination of these computational results with the ALC-μSR and TF-μSR experimental data provides a unique insight into electron transport in these materials.

DFTB+ implements Density Functional Theory Tight Binding (DFTB), which is an electronic structure method that uses the Kohn-Sham approximation to solve the quantum many body problems for electrons. DFTB is more approximate than DFT, as

it truncates the exact Kohn-Sham energy to a second-order approximation and expands the wavefunction in a series of confined atomic orbitals.[28] As a result, a DFTB calculation is computationally much cheaper than a DFT calculation. However, computational speed comes with an accuracy cost, as DFTB+ is not an *ab initio* code: it makes use of parametrisations computed from pure DFT calculations to describe interactions between chemical species.[26]

These parametrisations were stored in the so-called Slater-Koster files, which are computed to cover specific groups of elements. For the simulation of the tetrakis (2-phenylethynyl) silane and the phenylacetylene capped silicon nanoparticles, the well-documented pbc Slater-Koster parameter set pbc was utilised.[29]

As regards the CASTEP calculations, a plane wave cut-off for these calculations was chosen by converging energy and forces. This was done using the automated tool CASTEPconv,[30] to try a range of possible values, with every other condition fixed. The final choices were the values for which any successive refinement yielded a difference in energy and forces lower than a fixed tolerance. This was taken to be smaller than the tolerances used for the self-consistent field and geometry optimisation calculations. In the end, a value of 700 eV was chosen for the CASTEP plane wave cut-off. As regards the k-point grid size, as big molecules are being simulated here, a single-point 1×1×1 k-point grid was used. This produced forces accurate well within an error of 0.05 eV/Å, which as mentioned above was used as the limit tolerance for geometry optimisation. CASTEP calculations were also performed to calculate the values of the hyperfine tensors for the muonium in the muoniated samples.

Geometry optimisations on these structures were performed with a BFGS algorithm, with fixed unit cell parameters, and using both CASTEP and DFTB+, to a tolerance of 0.05 eV/Å for the forces. For CASTEP, the PBE exchange-correlation function was used, in combination with auto-generated ultrasoft pseudopotentials. As regards the DFTB+ calculations, also a self-consistent charge scheme,[30] 3rd order corrections were used.[30]

2.6 References

1. Abi Munajad.; Cahyo Subroto, S., Fourier Transform Infrared (FTIR) Spectroscopy Analysis of Transformer Paper in Mineral Oil-Paper Composite Insulation under Accelerated Thermal Aging. *Energies* **2018,** *11* (2), 364.

2. Cui, H. A.-S., A.; Li, S.; Islan, S. , Correlation between dissolved gases and oil spectral response. *In Proceeding s of the 1st International Conference on Electrical Materials and Power Equipment(ICEMPE)* **2017**.

3. Bakar, N. A. C., H.; Abu-Siaba, A.; Li, S., A review of spectroscopy technology applications in transformer condition monitoring. *In Proceeding s of the 1st International Conference on Electrical Materials and Power Equipment(ICEMPE)* **2016**.

4. Willard HH, M. J. L., Dean JA, Instrumental Methods of Analysis. 506-507.

5. Bunaciu, A. A.; Udristioiu, E. G.; Aboul-Enein, H. Y., X-ray diffraction: instrumentation and applications. *Crit Rev Anal Chem* **2015,** *45* (4), 289-99.

6. My Scope-training for advanced research. https://myscope.training/#/SEM (accessed 3-5-2018).

7. Wang, Z. L., Transmission Electron Microscopy of Shape-Controlled Nanocrystals and Their Assemblies. *The Journal of Physical Chemistry B* **2002,** *104*, 1153-1175.

8. Kivelson, S. A.; Bindloss, I. P.; Fradkin, E.; Oganesyan, V., How to detect fluctuating stripes in the high-temperature. *Rev. Mod. Phys* **2003,** *75*, 1201-1241.

9. Beck, S. Across the Spectrum: Instrumentation for UV/Vis Spectrophotometry. (accessed 23-1-2020).

10. Gfroerer, T. H., Photoluminescence in Analysis of Surfaces and Interfaces. In *Encyclopedia of Analytical Chemistry*, 2006.

11. Williams, A. T. R.; Winfield, S. A.; Miller, J. N., Relative fluorescence quantum yields using a computer-controlled luminescence spectrometer. *Analyst* **1983,** *108* (1290), 1067-1071.

12. Measuring Molecular Weight, Size and Branching of Polymers. (accessed 23-1-2020).

13. Uemura, Y. J., Muon spin relaxation studies on high‐TC superconductors and related antiferromagnets (invited). *Journal of Applied Physics* **1988,** *64* (10), 6087-6091.

14. Drew, A. J.; Hoppler, J.; Schulz, L.; Pratt, F. L.; Desai, P.; Shakya, P.; Kreouzis, T.; Gillin, W. P.; Suter, A.; Morley, N. A.; Malik, V. K.; Dubroka, A.; Kim, K. W.; Bouyanfif, H.; Bourqui, F.; Bernhard, C.; Scheuermann, R.; Nieuwenhuys, G. J.; Prokscha, T.; Morenzoni, E., Direct measurement of the electronic spin diffusion length in a fully functional organic spin valve by low-energy muon spin rotation. *Nature Materials* **2009,** *8* (2), 109-114.

15. Sugiyama, J.; Nozaki, H.; Umegaki, I.; Mukai, K.; Cottrell, S. P.; Shiraki, S.; Hitosugi, T.; Sassa, Y.; Suter, A.; Salman, Z.; Prokscha, T.; Månsson, M., Li-Diffusion in Spinel Li[Ni1/2Mn3/2]O4 Powder and Film Studied with u+SR. *Journal of the Physical Society of Japan* **2018,** *21* (21).

16. Réotier, P. D. d.; Yaouanc, A., Muon spin rotation and relaxation in magnetic materials. *J. Phys.: Condens. Matter* **1997,** *9*, 9113.

17. Hempelmann, R.; Soetratmo, M.; Hartmann, O.; Wappling, R., Muon diffusion and trapping in proton conducting oxides. *Solid State Ionics* **1998,** *107*, 269-280.

18. Sugiyama, J.; Nozaki, H.; Umegaki, I.; Mukai, K.; Miwa, K.; Shiraki, S.; Hitosugi, T.; Suter, A.; Prokscha, T.; Salman, Z.; Lord, J. S.; Månsson, M., Li-ion diffusion in Li4Ti5O12 and LiTi2O4 battery materials detected by muon spin spectroscopy. *Phys. Rev. B* **2015,** *92* (1), 014417.

19. McKenzie, I.; Scheuermann, R.; Sedlak, K.; Stoykov, A., Molecular Dynamics in Rod-Like Liquid Crystals Probed by Muon Spin Resonance Spectroscopy. *The Journal of Physical Chemistry B* **2011,** *115* (30), 9360-9368.

20. Walker, D. C., *Muon and Muonium Chemistry*. Cambridge University Press: Cambridge, 1983.

21. Pratt, F. L.; Blundell, S. J.; Marshall, I. M.; Lancaster, T.; Husmann, A.; Steer, C.; Hayes, W.; Fischmeister, C.; Martin, R. E.; Holmes, A. B., μSR in polymers. *Phys. B: Condensed Matter* **2003,** *326* (1), 34-40.

22. Lord, J. S.; McKenzie, I.; Baker, P. J.; Blundell, S. J.; Cottrell, S. P.; Giblin, S. R.; Good, J.; Hillier, A. D.; Holsman, B. H.; King, P. J. C.; Lancaster, T.; Mitchell, R.; Nightingale, J. B.; Owczarkowski, M.; Poli, S.; Pratt, F. L.; Rhodes, N. J.; Scheuermann, R.; Salman, Z., Design and commissioning of a high magnetic field muon spin relaxation spectrometer at the ISIS pulsed neutron and muon source. *Rev. Sci. Instrum.* **2011,** *82* (7), 073904.

23. Khasanov, R.; Guguchia, Z.; Maisuradze, A.; Andreica, D.; Elender, M.; Raselli, A.; Shermadini, Z.; Goko, T.; Knecht, F.; Morenzoni, E.; Amato, A., High pressure research using muons at the Paul Scherrer Institute. *High Pressure Research* **2016,** *36* (2), 140-166.

24. Arnold, O.; Bilheux, J. C.; Borreguero, J. M.; Buts, A.; Campbell, S. I.; Chapon, L.; Doucet, M.; Draper, N.; Ferraz Leal, R.; Gigg, M. A.; Lynch, V. E.; Markvardsen, A.; Mikkelson, D. J.; Mikkelson, R. L.; Miller, R.; Palmen, K.; Parker, P.; Passos, G.; Perring, T. G.; Peterson, P. F.; Ren, S.; Reuter, M. A.; Savici, A. T.; Taylor, J. W.; Taylor, R. J.; Tolchenov, R.; Zhou, W.; Zikovsky, J., Mantid—Data analysis and visualization package for neutron scattering and μ SR experiments. *Nucl. Instrum. Methods Phys. Res., Sect. A* **2014,** *764*, 156-166.

25. Porezag, D.; Frauenheim, T.; Köhler, T.; Seifert, G.; Kaschner, R., Construction of tight-binding-like potentials on the basis of density-functional theory: Application to carbon. *Physical Review B* **1995,** *51* (19), 12947-12957.

26. Clark, S. J.; Segall, M. D.; Pickard, C. J.; Hasnip, P. J.; Probert, M. J.; Refson, K.; Payne, M. C., First principles methods using CASTEP. *ZKri* **2005,** *220* (5-6), 567-570.

27. Elstner, M.; Porezag, D.; Jungnickel, G.; Elsner, J.; Haugk, M.; Frauenheim, T.; Suhai, S.; Seifert, G., Self-consistent-charge density-functional tight-binding method for simulations of complex materials properties. *Physical Review B* **1998,** *58* (11), 7260-7268.

28. Köhler, C.; Frauenheim, T., Molecular dynamics simulations of CFx (x=2,3) molecules at Si3N4 and SiO2 surfaces. *Surf. Sci.* **2006,** *600* (2), 453-460.

29. Sturniolo, S.; Liborio, L.; Jackson, S., Comparison between density functional theory and density functional tight binding approaches for finding the muon stopping site in organic molecular crystals. *J Chem Phys* **2019,** *150* (15), 154301.

30. Yang; Yu, H.; York, D.; Cui, Q.; Elstner, M., Extension of the Self-Consistent-Charge Density-Functional Tight-Binding Method: Third-Order Expansion of the Density Functional Theory Total Energy and Introduction of a Modified Effective Coulomb Interaction. *J. Phys. Chem. A* **2007,** *111* (42), 10861-10873.

Chapter 3: Preparation of Phenylacetylene capped Silicon Nanoparticles for Muon Study

This chapter describes the synthesis of silicon nanoparticle capped by phenylacetylene. Optical property, thermal property and Scanning electron microscope (SEM) images are included.

Contents

3.1 Overview

Energy shortage and climate change are two of the most serious problems threatening our society. The US Department of Energy (DOE) recognizes thermoelectric technology as one of several potential technological solutions. Specifically, thermoelectric (TE) technology could help to solve the vehicle electrification problem and thus contribute to significantly reducing CO2 emissions. The DOE continues to commit public money to TE technology development.[1]

A TE device is a solid-state energy converter that converts thermal energy directly into electricity. The efficiency of a TE device depends on the performance of its component materials, and it is embodied in a dimensionless figure of merit ZT, which is given by the following expression:[2]

$$ZT = \frac{\sigma S^2 T}{k} \qquad (3.1)$$

where σ is the electrical conductivity, S is the Seebeck coefficient, k is the thermal conductivity and T is the absolute temperature.

Ligand attachment to silicon nanoparticles has the potential to improve the thermal electrical conductivity between particles.[3]

3.2 Synthesis of Phenylacetylene capped Silicon Nanoparticles

Sodium metal (0.7 g) and naphthalene (2.9 g) were sonicated in dry THF (70 ml) for 2 hours to prepare sodium naphthalide. It gives a dark green suspension. Silicon tetrachloride was dispersed in THF and continuously stirred. To this, a solution of lithium phenylacetylide (5 ml, 1 M solution in tetrahydrofuran) was added, followed by further stirring for 30 minutes. After the lithium phenylacetylide was ready, the sodium naphthalide was mixed with the lithium phenylacetylide and silicon tetrachloride, and kept refluxing for 8 hours. All precipitates settled, the clear liquid was decanted off and all solvent was removed under vacuum. This obtained solid was then heated to 373 K under low pressure to remove the remaining naphthalene. The resulting product was redissolved in DCM, and washed with DI water and methanol to remove all the remaining lithium chloride. The organic layer was dried to give phenylacetylene capped silicon nanoparticles, as an orange crystalline solid.

3.3 Characterisation of Phenylacetylene capped Silicon Nanoparticles

Measurements were performed to ensure the characteristics of Phenylacetylene capped silicon nanoparticles, such as FTIR, PL/UV, DLS and TGA/DSC.

3.3.1 Fourier transform infrared spectroscopy

The FTIR spectrum shows the peaks which are characteristic of phenylacetylene capped silicon nanoparticles (see Figure 25). The peak at 3051 cm^{-1} indicates the presence of aromatic C-H, and at 1596 and 1488 cm^{-1} it indicates the presence of aromatic C-C bonds. A sharp peak at 2162 cm^{-1} is observed, which is representative of the C≡C stretching mode. This suggests the alkyne is attached to the silicon nanoparticles. The peaks at 1441 and 1221 cm^{-1}, that are representative of Si-C≡C, also support the suggestion that the alkyne is attached to the silicon nanoparticles. The peaks at 1068 and 1026 cm^{-1} are characteristic of phenylacetylene.

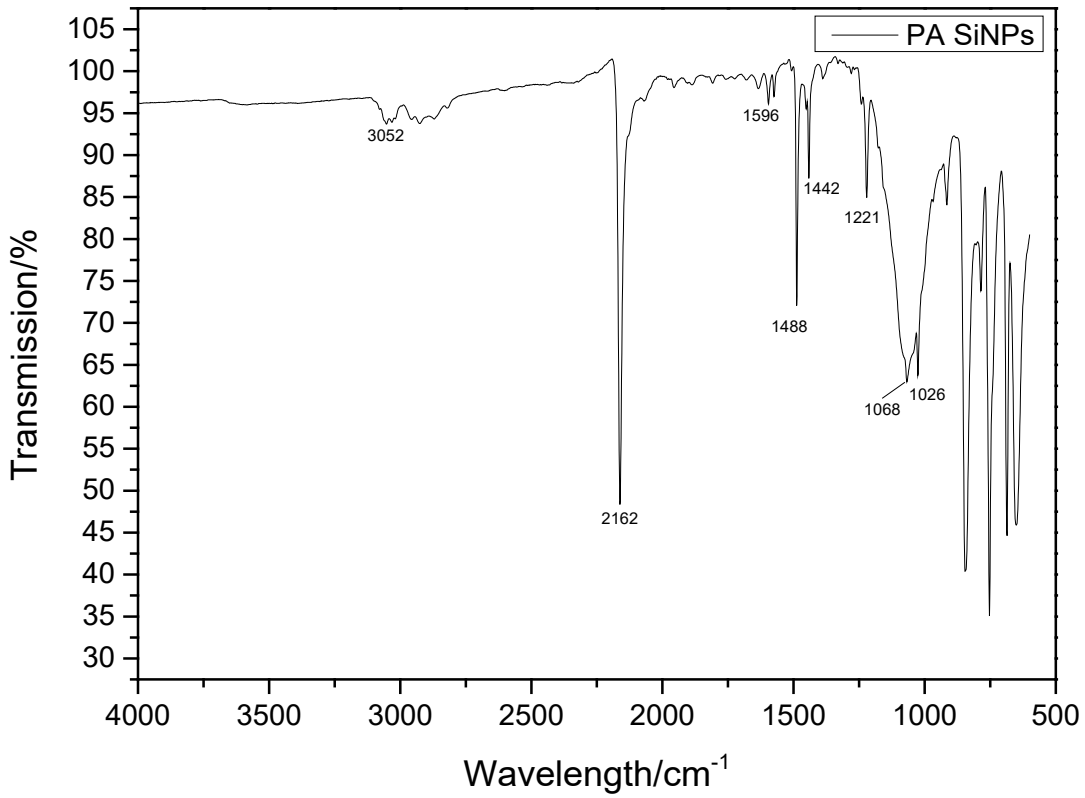

Figure 25. FTIR spectrum of phenylacetylene capped silicon nanoparticles

3.3.2 Photoluminescence spectroscopy/Ultra-visible spectroscopy

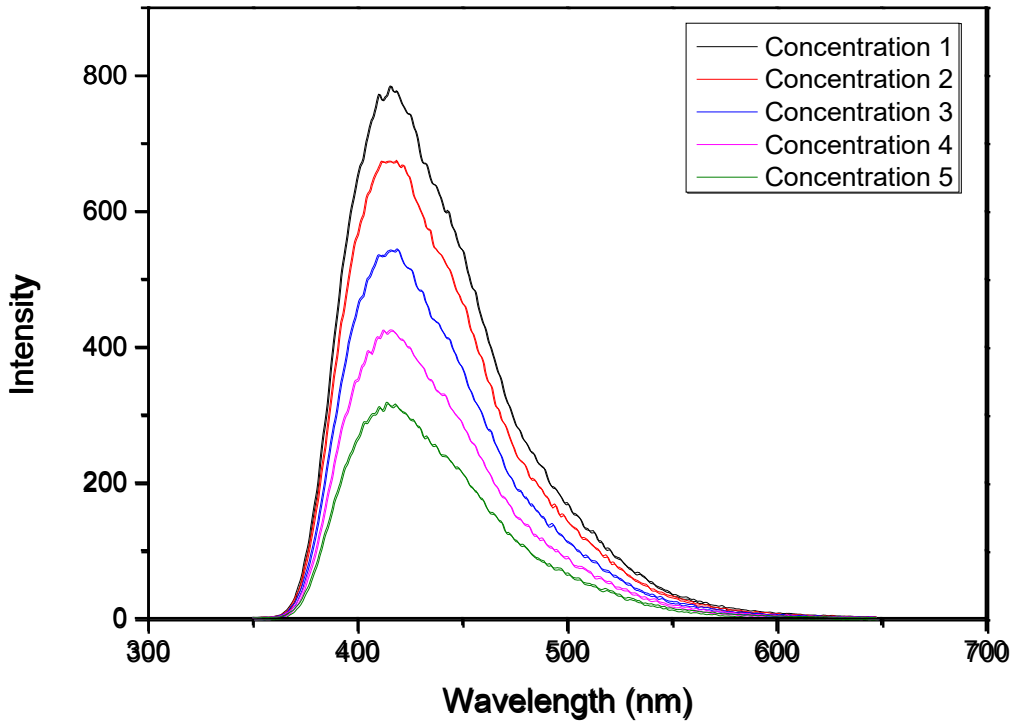

Figure 26. PL spectrum of phenylacetylene capped silicon nanoparticles (excitation wavelength=340 nm, emission bandwidth=10 nm, excitation bandwidth=10 nm).

Figure 26 shows the PL spectrum of phenylacetylene capped silicon nanoparticles at five different concentrations. The UV-Vis spectrum of silicon nanoparticles at the same five concentrations is shown in Figure 27.

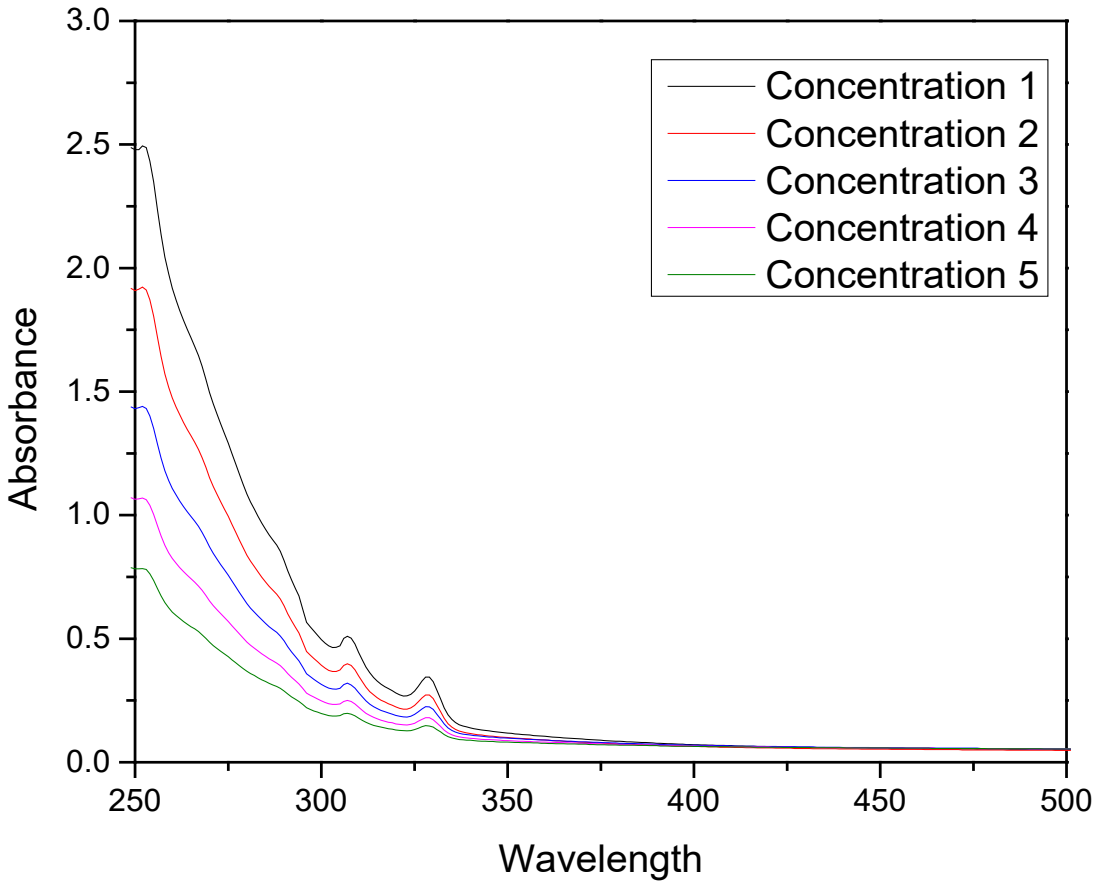

Figure 27. UV spectrum of phenylacetylene capped silicon nanoparticles.

3.3.3 Dynamic light scattering

From the DLS spectrum shown in Figure 28, it can be observed that the size of the phenylacetylene capped silicon nanoparticles is around 6 nm. Three measurements with 15 runs each were taken to obtain an average result. All the phenylacetylene capped silicon nanoparticles are hit by the light. The particle size observed with electron microscopy is often slightly smaller than the hydrodynamic diameter measured by DLS. This observation can be explained by occasional strong aggregation of the particles.[4]

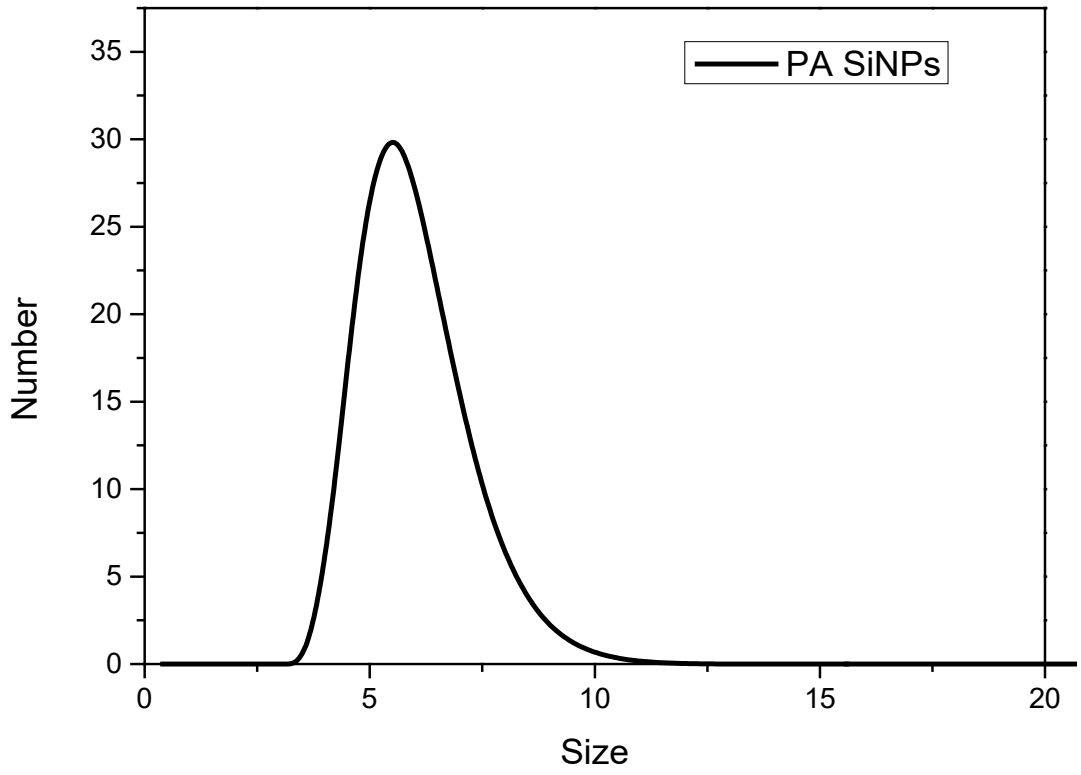

Figure 28. DLS spectra for phenylacetylene capped silicon nanoparticles.

3.3.3 Scanning electron microscope

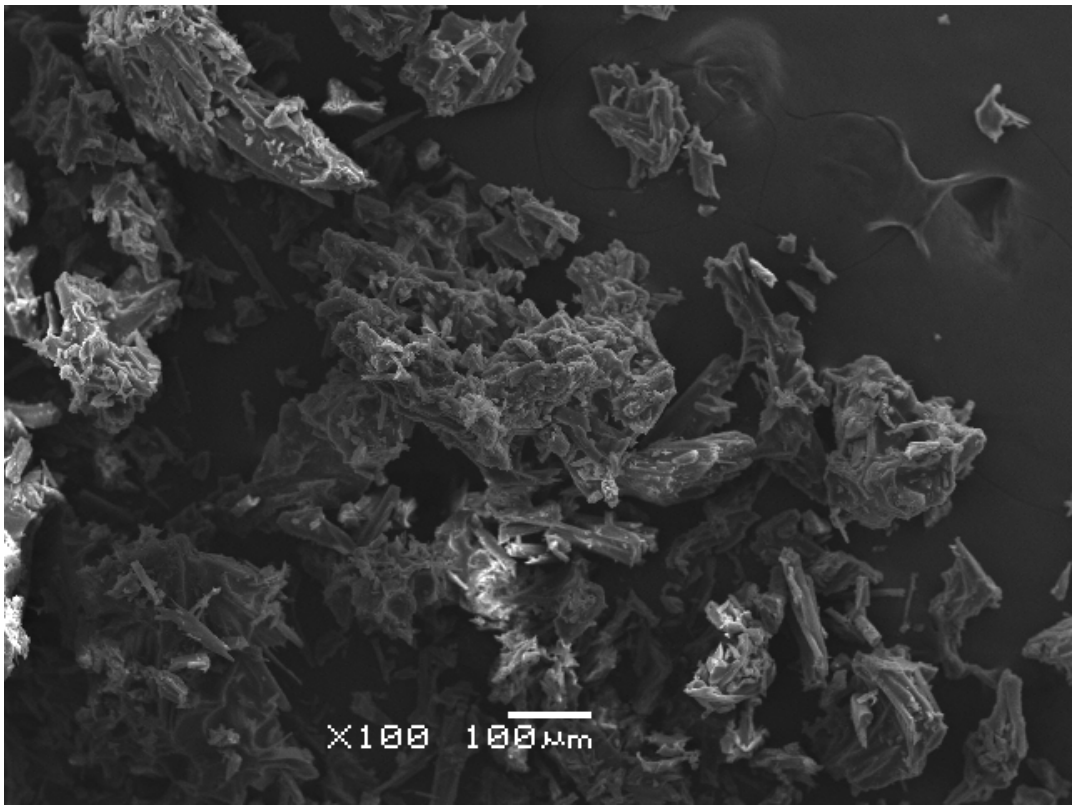

Figure 29. SEM image of phenylacetylene capped silicon nanoparticles.

From the SEM image shown in Figure 29, it can be observed that there is aggregation of the phenylacetylene capped silicon nanoparticles; the scale of SEM makes it difficult to measure the size of the nanoparticles. The STEM image of the silicon nanoparticles is shown in Figure 30.

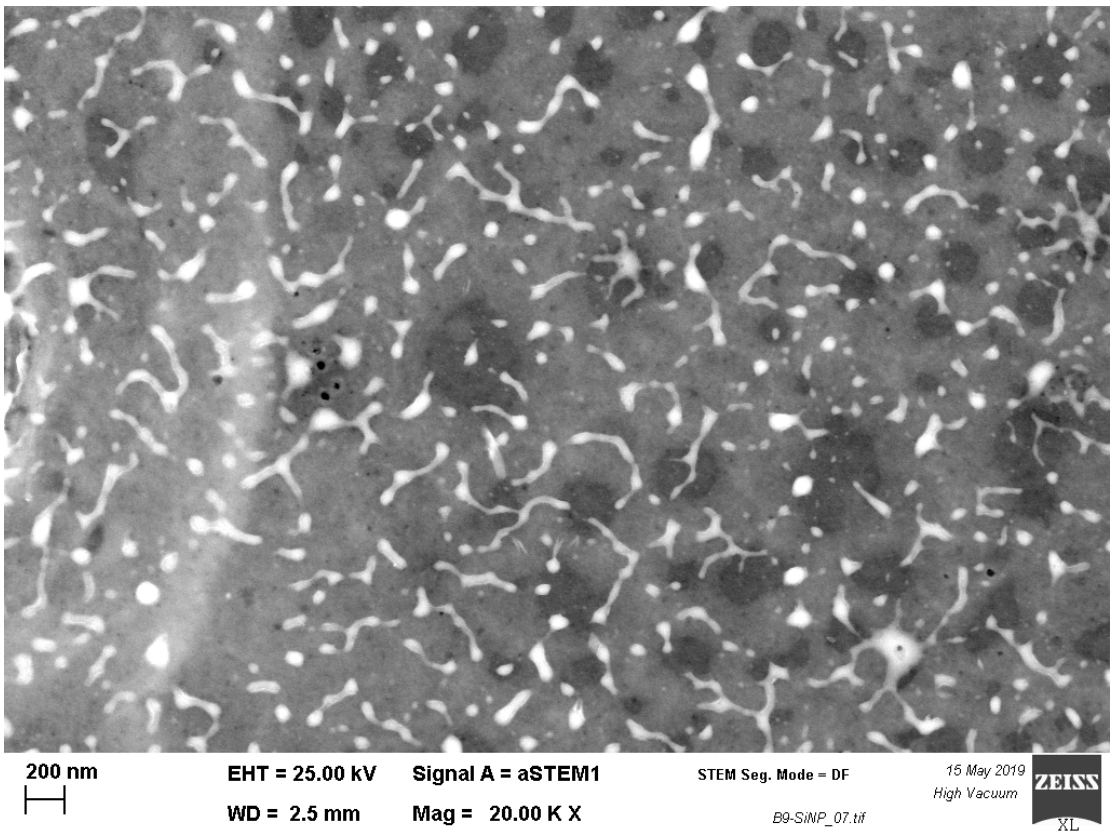

Figure 30. STEM image of phenylacetylene capped silicon nanoparticles (scale of 200 nm).

In the STEM image with a scale of 200 nm, the aggregation of phenylacetylene is shown clearly. Some of the shadows are over 200 nm and some are much smaller than this. A high resolution STEM image is shown in Figure 31. With the scale of 20 nm, it can be observed that the size of the silicon nanoparticles is smaller than 10 nm, which has been proved by the DLS measurement. However, the resolution is limited by the STEM machine.

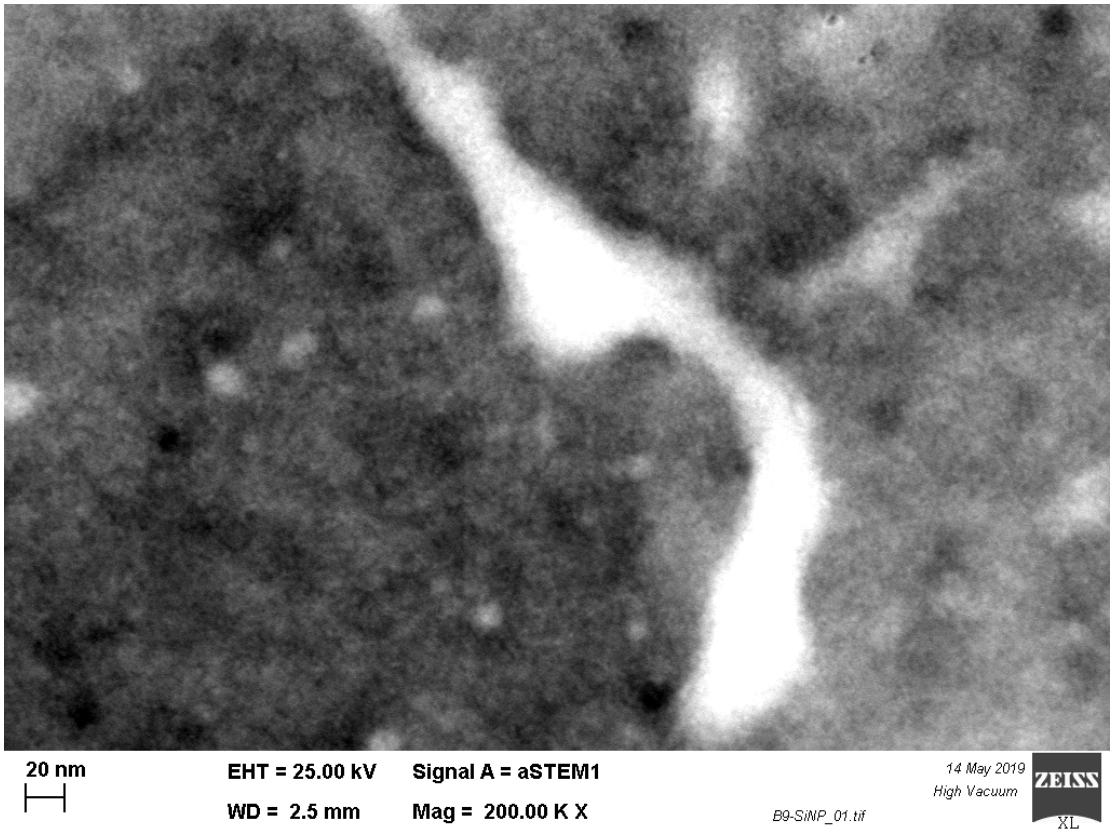

Figure 31. STEM image of phenylacetylene capped silicon nanoparticles (scale of 20 nm).

3.4 Thermal stability

The initially flat heat flow and sample weight lines show stability up until ~200°C. After this, there is a negative heat flow which may be explained by the liquidation of the PASiNP. This is supported by the gradual decrease in weight. The continued reduction in weight suggests that degradation proceeds gradually. This enabled the heat flow to reach a maximum of approximately 1.6 Wg-1 at 330°C. The rate of degradation increased between 250 and 325°C, but then steadied until ~450– 600°C, and then again between 900 and 1150°C. As expected, each of these features was followed by an increase in heat flow.

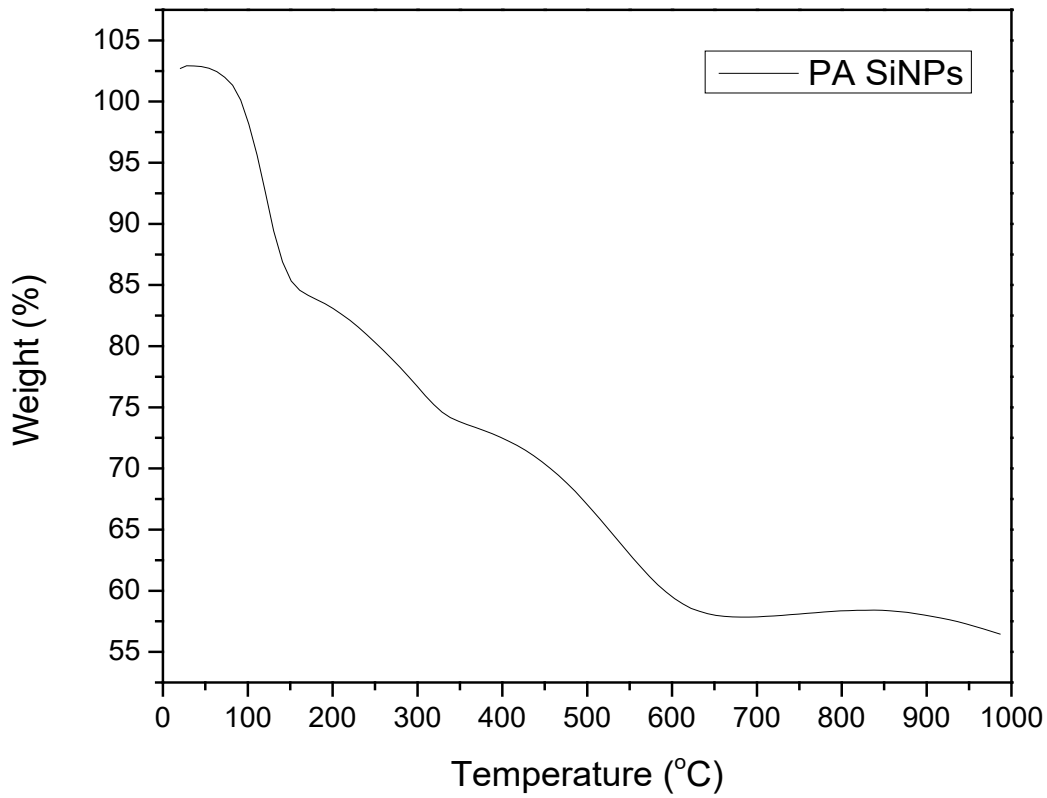

Figure 32. TGA of phenylacetylene capped silicon nanoparticles (scale of 20 nm).

The DSC trace shown in Figure 33 fluctuates at the beginning because of the evaporation of the solvent. The solid-liquid phase transition is also represented before 165°C. Meanwhile, the weight on the TGA trace shown in Figure 32 remains close to 100°C. After this feature, the heat flow into the sample begins to decrease, which shows that the sample starts to undergo degradation. In this region a minimum is observed in TGA, showing a higher rate of weight loss at this point. The DSC trace reaches a maximum at 330°C, showing completion of the initial degradation. After 350°C, an increase in the heat flow into the sample is shown in the DSC trace. The weight continues to reduce at the temperature point and this trend becomes more rapid at around 500°C. After 650°C, there is only little change in weight. The overall weight loss at 1000°C is 45%.

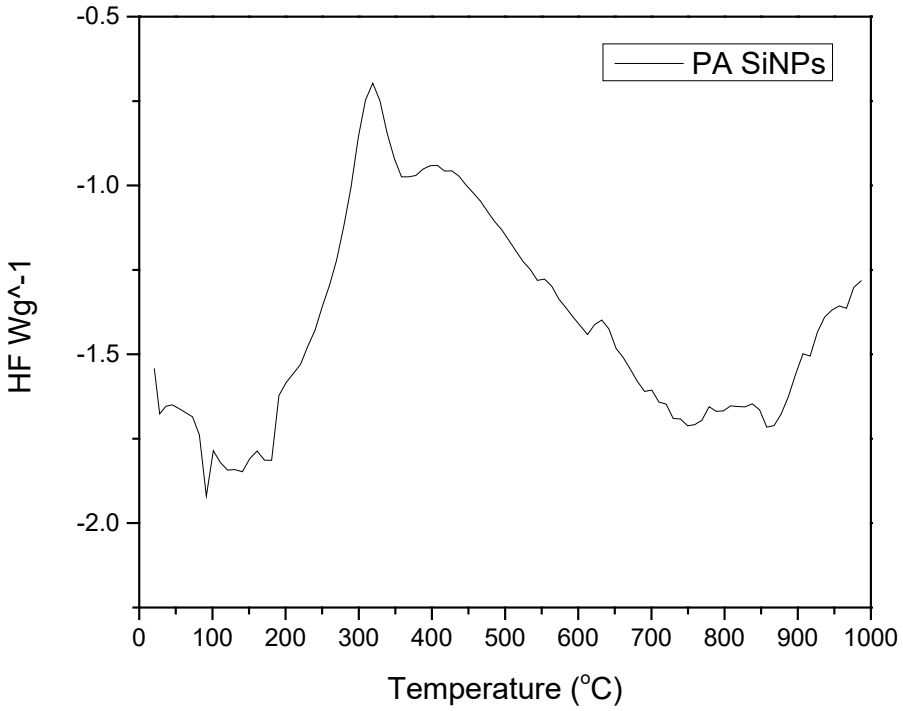

Figure 33. DSC of phenylacetylene capped silicon nanoparticles (scale of 20 nm).

3.5 References

1. Hendricks, T.; Choate, W. T. *Engineering Scoping Study of Thermoelectric Generator Systems for Industrial Waste Heat Recovery*; US Department of Energy: 2006.

2. Ashby, S.; Thomas, J. A.; Garcia-Canadas, J.; Min, G.; Corps, J.; Powell, A. V.; Xu, H.; Shen, W.; Chao, Y., Bridging Silicon Nanoparticles and Thermoelectrics: Phenylacetylene Functionalization. *Faraday Discuss.* **2014,** *176*, 349-361.

3. Belomoin, G.; Therrien, J.; Smith, A.; Rao, S.; Twesten, R., Observation of a magic discrete family of ultrabright Si nanoparticles. **2002,** *80*, 841-843.

4. Richard K. Baldwin, K. A. P., Jayne C. Garno, Phillip P. Power, Gang-yu Liu, and Susan M. Kauzlarich, Room Temperature Solution Synthesis of Alkyl-Capped Tetrahedral Shaped. *J. Am. Chem. Soc* **2002,** *124* (7), 1150-1151.

Chapter 4: Muon Study on phenylacetylene capped silicon nanoparticles

Phenylacetylene capped silicon nanoparticles (Phenyl-SiNPs) have attracted interest as a novel thermo-electric material. This chapter reports and discusses the results from Muon Spin Spectroscope. Combined muon spectroscopic and computational study of this material in solution state are included.

Contents

4.1 Overview

Energy shortage and climate change are two of the most serious problems threatening our society. The US Department of Energy (DOE) recognizes thermoelectric technology as one of several potential technological solutions. Specifically, thermoelectric (TE) technology could help to solve the vehicle electrification problem and thus contribute to significantly reducing CO2 emissions. The DOE continues to commit public money to TE technology development.[1]

A TE device is a solid-state energy converter that converts thermal energy directly into electricity. The efficiency of a TE device depends on the performance of its component materials, and it is embodied in a dimensionless figure of merit ZT, which is given by the following expression:[2]

$$ZT = \frac{\sigma S^2 T}{k} \qquad (4.1)$$

where σ is the electrical conductivity, S is the Seebeck coefficient, k is the thermal conductivity and T is the absolute temperature.

Nanostructured silicon is a promising semiconductor material for thermoelectric devices. Silicon has major advantages in its low cost, relative abundance and low toxicity,[3, 4] and many silicon-based materials have been investigated for potential thermoelectric applications.[5] In particular, phenylacetylene capped silicon nanoparticles (SiNPs), synthesized via the micelle reduction method,[2, 6] have the potential to become efficient thermoelectric materials, where transport of electrons is possible via conjugated ligands. Previous characterization measurements for this system provided electric conductivity in the region of 18 S·m-1, thermal conductivity 0.1 Wm-1K-1 and a Seebeck coefficient of 3228 µVK-1 at 300 K.[2]

Beams of 100% spin polarised positive muons are produced by high energy collisions between protons in particle accelerators and stopped in the sample under study. Muons are unstable particles with a mean lifetime of ~2.2 µs, with their decay positrons emitted preferentially in the polarisation direction. The time evolution of the polarisation can therefore be followed with great sensitivity by simply monitoring the time dependence of the decay positron distribution. Muons may thermalize in materials either as the positive muon, with a spin of ½ and a mass of approximately one ninth that of a proton or may bind an electron to form muonium (Mu), a light

isotope of the H atom. Chemically, Mu is almost identical to H and will undergo the same chemical reactions in the sample material. In this experiment it is the addition reaction that is of interest, to form a final state muoniated species.

A number of muon spectroscopic techniques are available, the choice depending on the information required. In this study, both avoided level crossing muon spin resonance (ALC-μSR) and transverse field muon spin rotation (TF-μSR) experiments have been carried out.

ALC-μSR is a technique where an external magnetic field is applied along the direction of the muon polarisation. This polarization is monitored as the applied field is scanned, with a loss of polarization measuring a level crossing resonance. Resonances occur when states with opposite muon spin become near-degenerate in energy, and are characterized by the selection rules (ΔM = 0, 1, 2), where M is the quantum number for the z-component of the total angular momentum of the muon, electron, nuclear system. For the case when ΔM = 0 (Δ0), a muon-proton spin flip-flop, the resonance field(BΔ0) given by the formula below:[5]

$$B^{\Delta_0} = \frac{1}{2}\left|\frac{A_\mu - A_p}{\gamma_\mu - \gamma_p} - \frac{A_\mu + A_p}{\gamma_e}\right| \qquad (4.2)$$

These resonances are seen for radicals in solid, liquid and gaseous phases.

For the ΔM = 1 resonance (Δ1), a muon spin flip transition occurs, the value of the external magnetic field at which this resonance is seen is given by:[5]

$$B^{\Delta_1} = \frac{1}{2}\left|\frac{A_\mu}{\gamma_\mu} - \frac{A_\mu}{\gamma_e}\right| \qquad (4.3)$$

where for isotropic media Aμ and Ap are the isotropic muon and proton hyperfine interaction constants in MHz, and can be used to estimate the vibrationally averaged electron spin density at the nucleus.[7] γμ, γp, and γe are the muon, proton, and electron gyromagnetic ratios, 135.5 MHz T^{-1}, 42.57 MHz T^{-1}, and 2.8025×104 MHz T^{-1}, respectively.[7] Since the peak position is related to the hyperfine couplings of the muon and the proton in the radical and, the hyperfine coupling constants being characteristic of the particular muoniated radical, one could use this for assigning the observed resonances to the appropriate radical species.[8]

In the previous work,[9] the ALC-μSR technique was employed to investigate Phenyl-SiNPs system in the solid state, where the preliminary results showed a

reduction in the measured line width of the resonance above room temperature, suggesting an activated behaviour for the system.[9]

The Fermi contact term, part of the hyperfine coupling, Aμ, may more straightforwardly be studied by carrying out a measurement where the external field is applied transverse to the direction of the muon spin. Relatively high fields are used that fall within the so-called

Pashen-Back regime. The frequency spectrum of a system under these circumstances is characterised by a strong diamagnetic peak and a pair of resonance peaks placed symmetrically about the diamagnetic peak, with the value of Aμ simply being determined by the splitting between these two measured lines. Software WIMDA was used to correlate line pairs in the measured data to obtain values for Aμ.[10]

Knowledge of the microscopic conduction rates and mechanisms in these materials would be useful in our attempts to improve these materials by design. μSR has been shown to be an elegant method for measuring microscopic conduction rates and mechanisms in conducting organic polymers,[11] which are materials structurally similar to the ligands found in phenylacetylene functionalized SiNPs. Further, muonium adducts to Carbon-Carbon triple bonds in other organic compounds have already been characterized.[12]

In this work, Phenyl-SiNPs in solution state are investigated by both ALC-μSR and TF-μSR, while a solution of the model compound tetrakis(2-phenylethynyl)silane is employed as a reference for comparison.

4.3 Computer Simulations

In the case of the model compound, there are eight possible sites of addition for the muonium in each of the phenylacetylene molecules bonded to the silicon atom, which would result in potentially eight different organic radicals. As regards the Phenyl-SiNPs, the potential addition sites for the muons are in the same phenylacetylene molecules, which are now attached to the silicon nanoparticles.

The molecular structure of the model compound, with its potential muon addition sites indicated in red, is shown in Figure 34. The eight potential addition sites for the muon correspond to all the regions of unsaturation in the organic ligand. When the

muon reacts with one of these unsaturated centres, it forms the muoniated radical, which has an unpaired electron that may be distributed throughout the molecule and may interact with the muon via the hyperfine coupling. In this work, the focus was placed on the calculation of the Fermi contact term part of the hyperfine tensor (Aμ), which can be compared to experimental results.

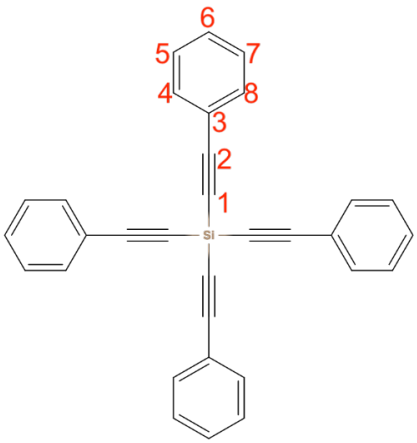

Figure 34. The tetrakis(2-phenyethynyl)silane molecule with the potential muon addition sites.

Table 3. Calculated values for the hyperfine contact term for the muon in the addition sites 1-8.

Sites	Contact Term (MHz)
1	483.8851
2	530.8176
3	517.8782
4	423.0317
5	504.2006
6	380.0408
7	508.2964
8	436.5915

The calculated contact terms for the muonium in the addition sites 1-8 of the model compound are shown in Table 3. The comparison of these values with the experimental results from TF-μSR (Figure 5), suggests that muonium is likely to be attached to C8. The values of the experimental results from TF-μSR also allow us to rule out the addition of the muon to any part of the silicon nanoparticle.

Regardless of the temperature dependence, Figures 5 (c) and (d), show that the Aμ is smaller in the Phenyl-SiNPs than in the model compound. This is likely to be indicating that the total spin density at the muon site is smaller when the muon is in a ligand attached to a nanoparticle, than when the muon is attached to the same organic ligand in the model compound.

The mean diameter of the experimentally produced Phenyl-SiNPs is 6 nm.[10] However, nanoparticles of that size are well beyond the simulation capabilities of DFT codes. Hence, it was necessary to develop an adequate model for the Phenyl-SiNP that was large enough to represent the properties that were experimentally observed and yet small enough to be computationally manageable.

To test this, a series of calculations on Si nanoparticles of different sizes, with different numbers of muoniated ligands attached to them, were performed. The model nanoparticles were built by using the Wulff construction method, and given a certain target radius. Their geometry was relaxed with DFTB+; then the ligands were attached radially to some surface atoms, and the geometry was relaxed again. Finally, for the systems simulated with CASTEP, the geometry was relaxed a third time to compensate for the small differences in potential between DFT and DFTB calculations. Particles were generated with radius between 3 and 6 Angstrom, and with 1 to 5 organic ligands attached to them. Figure 35 and Figure 36 show the schematic pictures of the type of systems that were simulated:

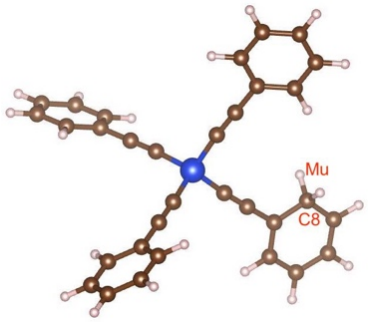

Figure 35. Muonated tetrakis(2-phenyethynyl)silane molecule, with muon on C8.

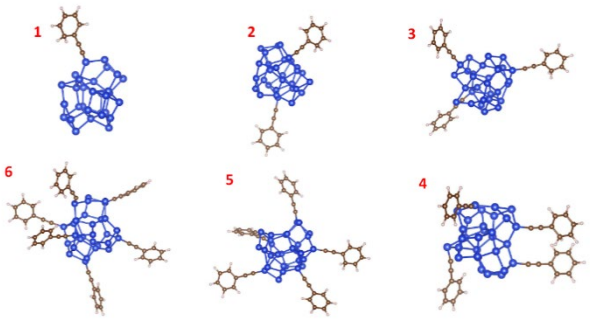

Figure 36. Nanoparticle systems simulated with DFTB+ to determine an appropiate nanoparticle siz tob e simulated with CASTEP

These initial calculations were done with the DFTB+ code, because it allows for the efficient treatment of relatively large systems. The modelled nanoparticles proved to have stable electronic structures and relaxed reasonably fast. Hence, nanoparticles of 6 ang. with six ligands were adopted as the systems used to simulate the Phenyl-SiNPs.

DFTB+, however, does not have a module to calculate values of hyperfine coupling tensors. Hence, to investigate the changes in values of the Fermi contact term (Aμ) of the muon, in the model compound and the Phenyl-SiNPs, CASTEP calculations were also performed on a 6 ang. Phenyl-SiNPs with six ligands attached to them. The muon in the 6 ang. Phenyl-SiNPs was placed in the Carbon C8 of one of the organic ligands, which is the same carbon where the muon was attached in the model compound.

4.4 Results and discussion

FTIR spectra gives evidence of successful capping of SiNPs with phenylacetylene. In Figure 4, the data shows a peak at 3052 cm^{-1} which is characteristic of aromatic C-H bonds. The peaks at both 1596 and 1487 cm^{-1} are representatives of aromatic C-C bonds. Also, the clearly visible sharp peak at 2159 cm^{-1} is characteristic of the C≡C bond suggesting that the terminal side of the alkyne is attached to silicon.

Another supporting evidence is the features characteristic of Si-C≡C peaks at 1451 and 1220 cm^{-1}. The model compound sample has the same rings attached to silicon, so the features are similar to the SiNPs, see the inset in Figure 37.

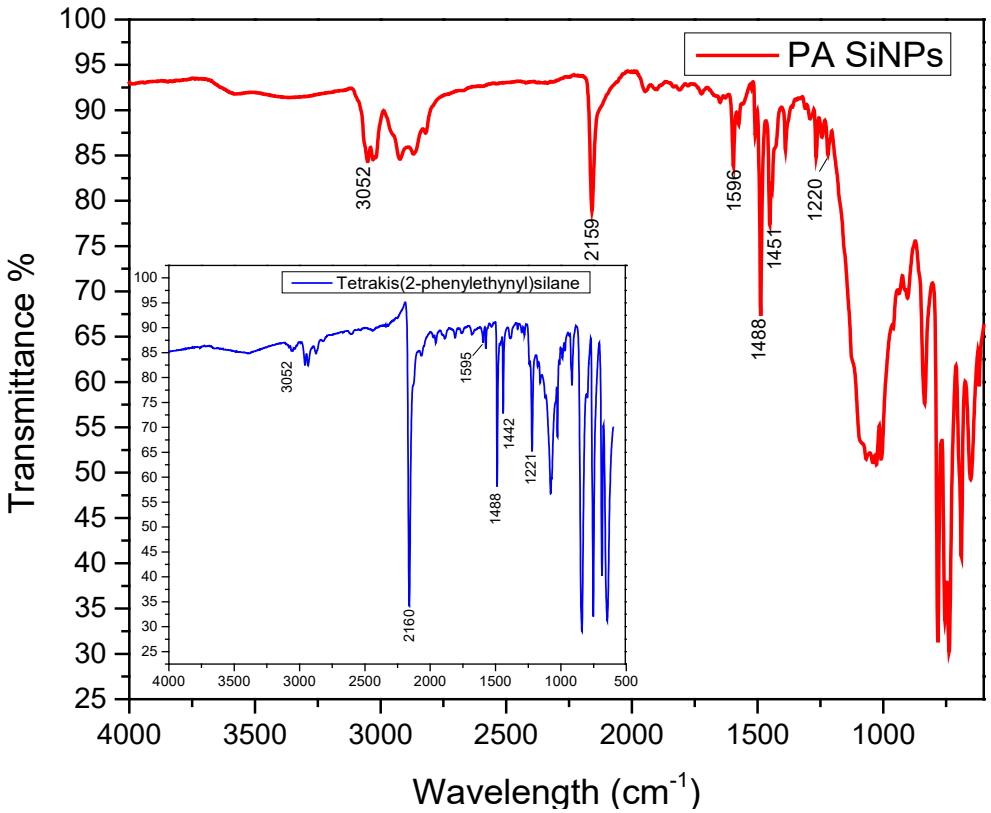

Figure 37. FTIR of phenylacetylene capped SiNPs. Inset, FTIR of tetrakis(2-phenylethynyl)silane.

The hyperfine parameters of the muon can be observed in the results of high transverse field (TF-μSR) experiments. Figure 38 (a) and (b) show the radical frequency correlation amplitude against hyperfine frequency at 300 K, whereas Figure 38 (c) and (d) show the temperature dependence of the muon's Fermi contact term, for the Phenyl-SiNPs and the model compound respectively. From the TF-μSR spectra shown in Figure 38, it can be seen that the peak positions at 300 K are around 350 MHz for Phenyl-SiNPs (Figure 38(a)), and around 450 MHz for the model compound (Figure 38(b)). Moreover, as the temperature increases, the TF-μSR peaks for the Phenyl-SiNPs move towards lower frequency values, whereas the model compound peaks move slightly towards higher frequency values. On the linear fittings, one can see that the slopes are -0.08 MHz/K and 0.036 MHz/K in Figure

38(c) and (d) respectively. The change of the frequency values for Phenyl-SiNPs has an absolute value of approximately 10 MHz, while the increasing of the frequency values for the model compound has an absolute value of approximately 4 MHz. These changes expressed as a percentage of the values of the frequencies at low temperatures, are of around 1% for the model compound and around -30% for the Phenyl-SiNPs.

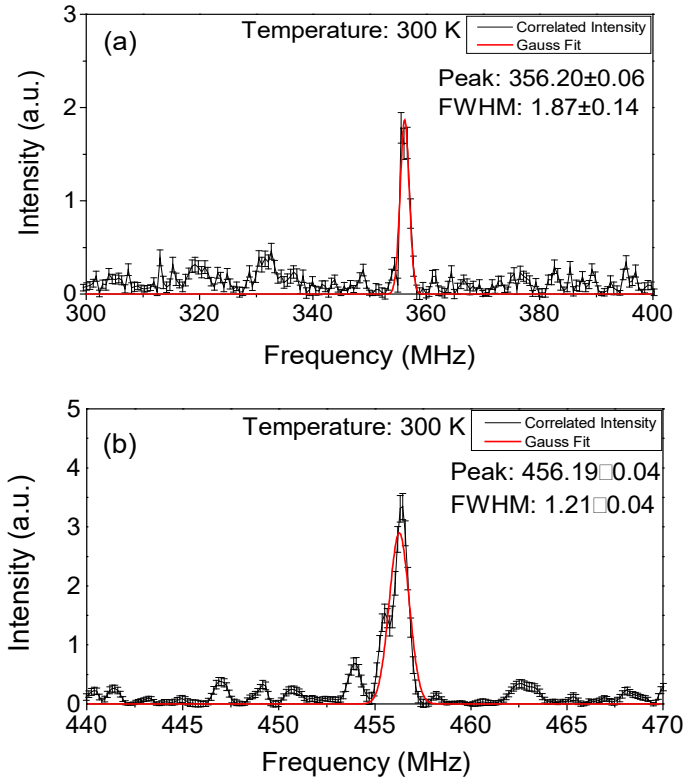

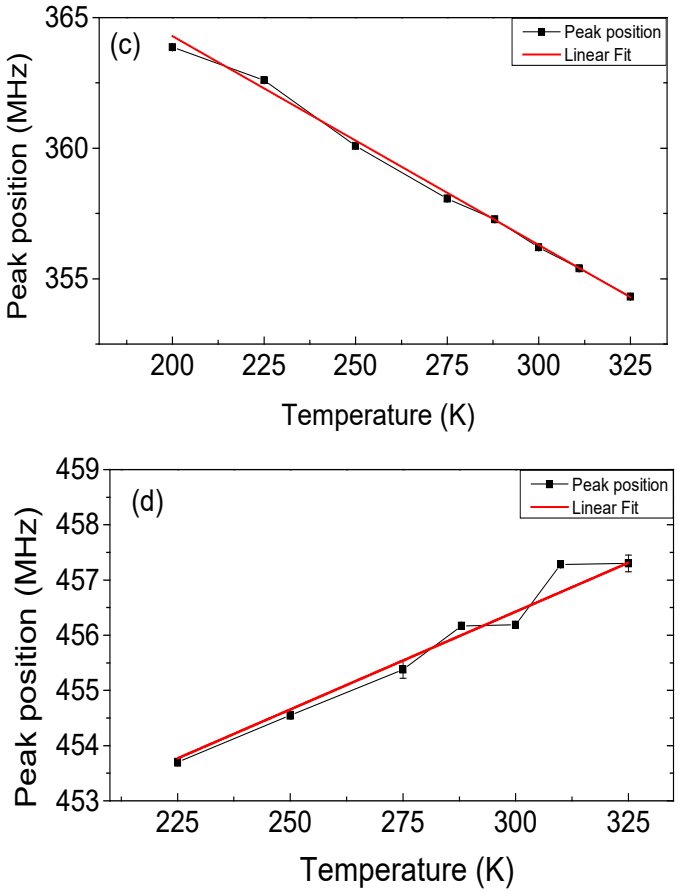

Figure 38. TF-μSR of Phenyl-SiNPs (a) and tetrakis(2-phenylethynyl)silane (b) at 300 K; The temperature dependance of Phenyl-SiNPs (c) and tetrakis(2-phenylethynyl)silane (d).

The change, therefore, is more relevant for the Phenyl-SiNPs. The changes are not only opposite in value, they are also very different in relative size, suggesting that the nanoparticles have much stronger thermoelectric behaviour than the compund model. The radical frequency correlation amplitude data for all the temperatures considered are displayed in Figure 39.

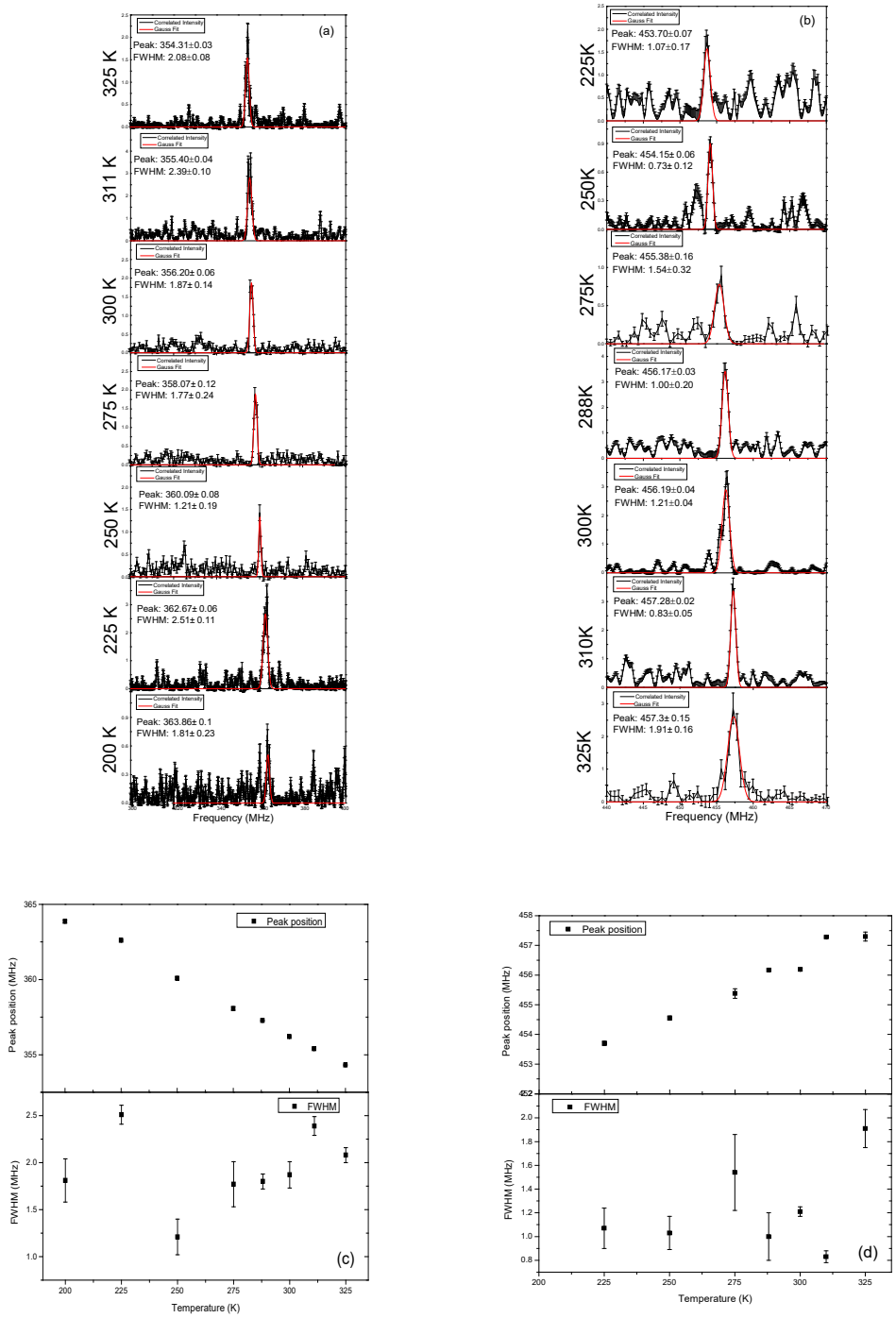

Figure 39. The TF-μSR of phenylacetylene capped SiNPs (a) and tetrakis (2-phenylethynyl) silane (b). The trend of TF-μSR peak position and FWHM for phenylacetylene capped SiNPs is shown in (c) and tetrakis (2-phenylethynyl) silane is shown in (d).

ALC-μSR results for both the nanoparticle and the model compound are shown in Figure 40. Clear Δ0 resonances associated to the Ipso hydrogens formed by the

addition of muon to the benzene rings, were observed in these samples, with interesting temperature effects including band broadening and resonance-peak shifting with temperature.

Table 4. ALC peak resonance position, width, intensity for SiNPs and molecule sample

Temp (K)	SiNPs resonance position (Gauss)	SiNPs width (Gauss)	SiNPs intensity	Molecule resonance position (Gauss)	Molecule width (Gauss)	Molecule intensity
200	17813	108.97	-0.00238	16675	95.63	-0.0009
225	17751	94.98	-0.00182	16621	104.61	-0.0013
250	17685	95.34	-0.00180	16569	80.97	-0.0013
275	17625	129.9	-0.00231	16503	92.18	-0.0013
300	17553	119.84	-0.00148	16478	97.48	-0.0017
325	17471	95.32	-0.00158	16399	62.48	-0.0040

Gaussian fitting shown in the Figure was performed by Mantid.[2] Figure 40 (a) and (b) show ALC-μSR spectra of Phenyl-SiNPs and the model compound taken at various temperatures. The ALC-μSR resonances are observed at values of the magnetic field of around 1.75 T for SiNPs and of around 1.65 T for the model compound sample. The temperature dependence of these ALC-μSR resonant peaks are plotted in Figure 40 (c) for SiNPs and in Figure 40 (d) for the model compound. The summary of the peaks is shown in Table 4.

In the temperature range from 200 K to 325 K, both the molecular sample and the nanoparticles show very similar trends, with the peak position decreasing as temperature increases (see Figure 40(c), (d) and Figure 41). With the aid of linear fittings, one can find the slopes are -2.7 G/K and -2.2 G/K in Figure 40(c) and (d) respectively. However, with the model compound sample, a very distinct difference is observed at temperature between 300 K and 325K: there is a significant strengthening and sharpening of the resonance at the higher temperature. All other

temperatures appear to show very similar resonances within the signal to noise of the present spectra.

This observed difference is likely to be due to the differences in dynamics of the two samples, particularly the barrier to rotation of the phenyl group, which is dependant on the bond order of the bonds between the phenyl ring and the nanoparticle or the Si atom in the model compound. Even though one tends to write these chemical formulae with the bonds between the phenyl ring and the silicon centre as a single bond followed by a triple bond and another single bond, the bond order in reality will be different due to any delocalisation of electrons. If we are to assume a smaller amount of delocalisation of the unpaired electron in the model compound compared to the nanoparticle, one would expect a higher barrier to phenyl rotation in the case of the nanoparticle compared to the model compound. Therefore, it is likely that we are observing this energy barrier around 325 K, in the case of the model compound while that for the nanoparticle would be predicted to be higher due to conduction.

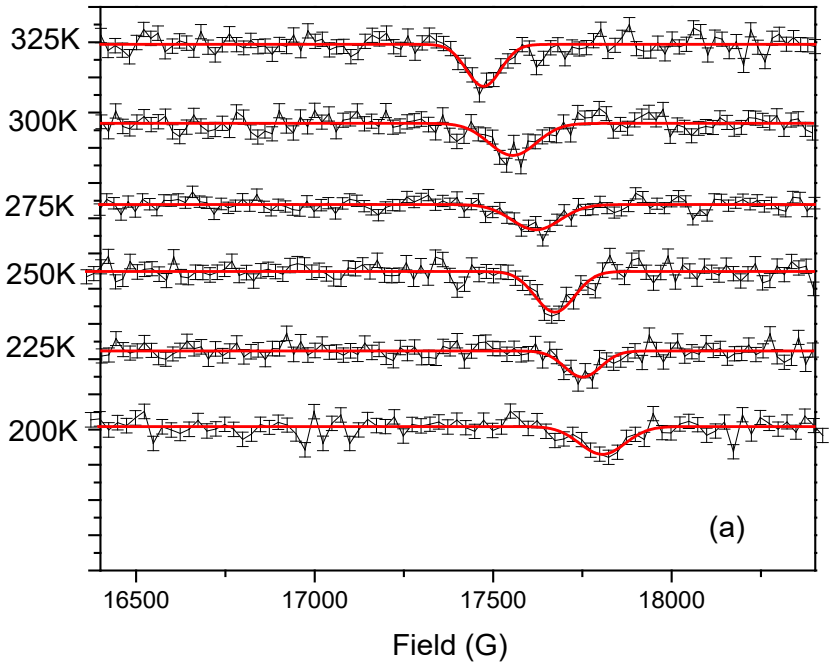

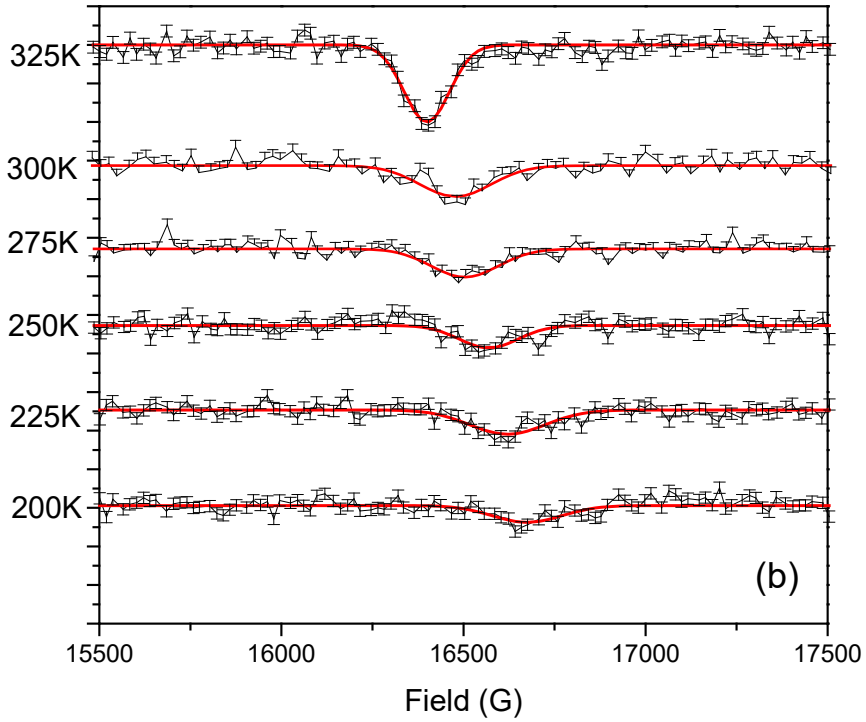
325K
300K
275K
250K
225K
200K
(b)
15500
16000
16500
17000
17500
Field (G)

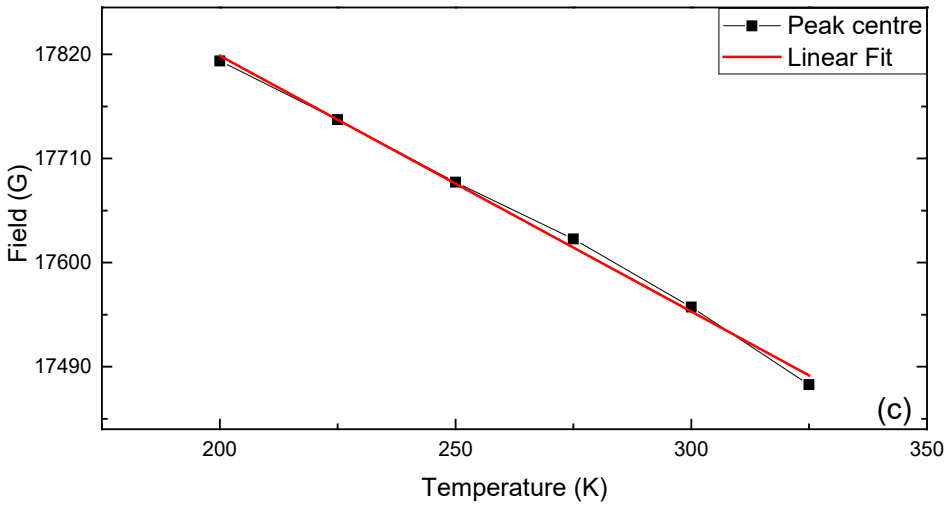
Peak centre
Linear Fit
17820
17710
17600
17490
Field (G)
(c)
200
250
300
350
Temperature (K)

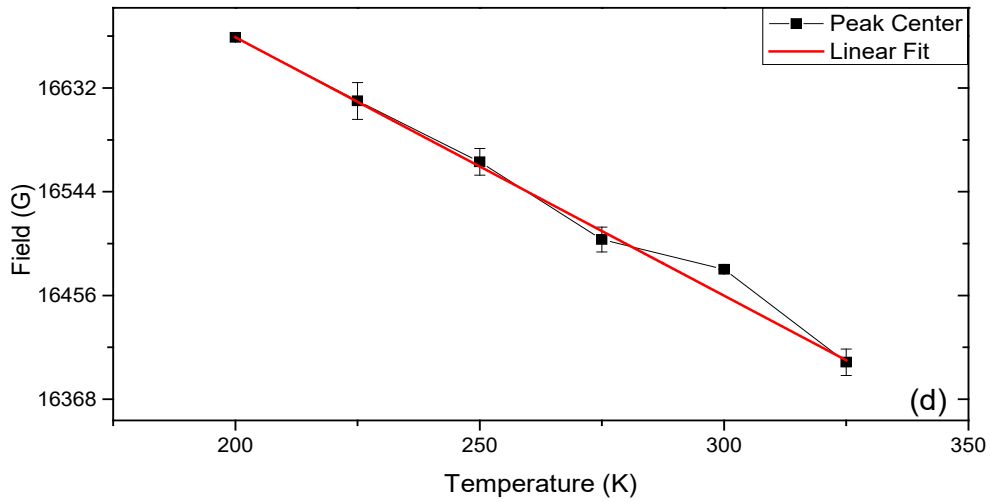

Figure 40. ALC-μSR of Phenyl-SiNPs (a) and tetrakis(2-phenylethynyl)silane (b). The temperature dependence of Phenyl-SiNPs (c) and tetrakis(2-phenylethynyl)silane (d).

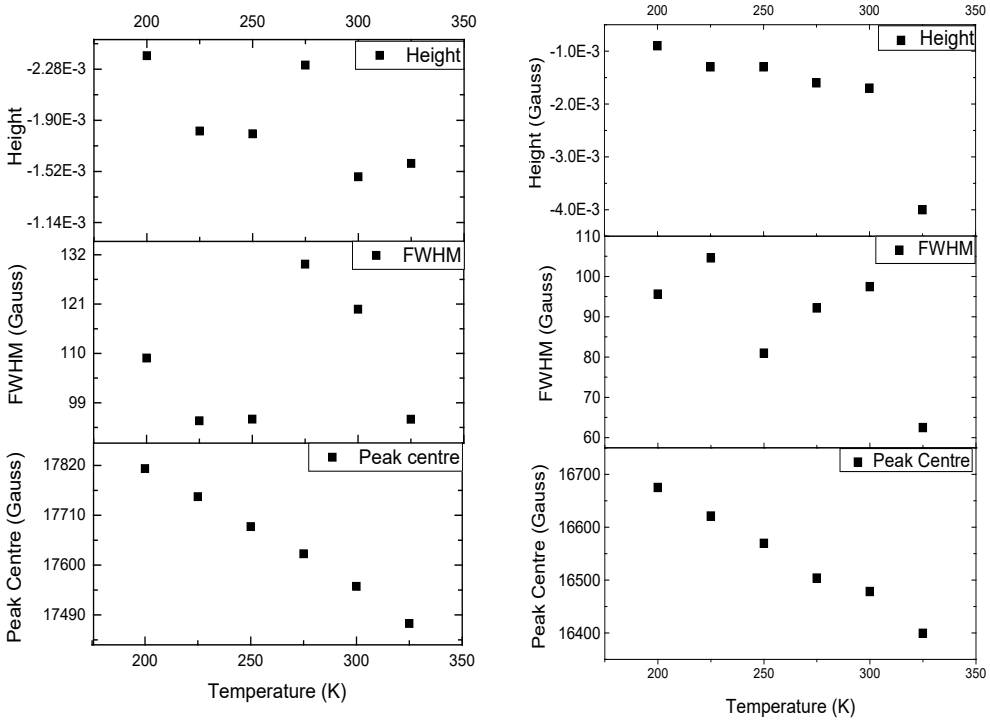

Figure 41. The trend of ALC-μSR height, FWHM, and peak position: phenylacetylene capped SiNPs (left) and tetrakis (2-phenylethynyl) silane (right). Note that for the Phenyl-SiNPs the Δ_0 line likely arises from coupling to the ring proton bonded to C5 in Figure 1, while for the model compound coupling is to the ipso-proton.

With observed values of Aμ from TF-μSR and Δ0 field from ALC-μSR at 300 K, the calculated values of Ap using equation (2) are 28.68 MHz and 147.89 MHz for

the Phenyl-SiNPs and the model compound respectively. Calculated values at other temperatures are listed in the Table 5.

Table 5 Calculated values for SiNPs and model compound at other temperatures

SiNPs

Temperature (K)	B^{Δ}_0 (T)	A_μ (MHz)	A_p (MHz)
200	1.78	362.86	30.72
225	1.776	362.6	31.21
250	1.768	360.09	30.20
275	1.763	358.07	29.11
300	1.756	356.2	28.68
325	1.746	354.31	28.53

Molecule

Temperature (K)	B^{Δ}_0 (T)	A_μ (MHz)	A_p (MHz)
225	1.662	453.7	142.83
250	1.657	454.55	144.59
275	1.650	455.38	146.71
300	1.648	456.19	147.89
325	1.640	457.3	150.47

For the model compound and the Phenyl-SiNPs, computer simulations have determined that site of addition for the muonium is in carbon C8 of one of the organic ligands bonded to the silicon atom or the silicon nanoparticle.

Table 6 presents and compares the CASTEP results obtained for the model compound and the Phenyl-SiNPs. It can be seen that, in agreement with the experimental results, the computed value of the Aμ for the Phenyl-SiNPs is smaller than the computed value of Aμ for the model compound. The modelling results also show that this decrease in the value of the Aμ is correlated with a decrease in the total electronic and spin density at the muon site when we go from the model

compound to the Phenyl-SiNPs. Furthermore, we used computational modelling to propose a plausible model for the experimentally observed effects of the temperature in the values of the Fermi contact terms of the muon in the model compound and the muoniated Phenyl-SiNPs.

The ALC-μSR results shown in Figure 40 are related to a Δ0 transition, which is the coupling between the muon and proton, and is represented by the Fermi contact term AH. The trends with temperature for the values of the Δ0 peaks for the model compound and the Phenyl-SiNPs observed in those experiments were the same. However, in the case of the TF-μSR experiments shown in Figure 5, the values of the Fermi contact term of the muon hyperfine coupling constant, Aμ, were estimated, which gives an estimate of the unpaired electron density at the muon site. These experiments show that the trends with temperature, for the values of Aμ in the model compound and the Phenyl-SiNPs, are different. As we discussed previously, in the analysis of Figure 38, the relative change in the value of Aμ is the relevant quantity to consider. In the case of Phenyl-SiNPs, the relative change in the value of Aμ - expressed as a percentage of its value at low temperatures, decreases by 30% with increasing in temperature, which indicates a decrease in the unpaired electronic density at the muon site. In the case of the model compound, the relative change in the value of Aμ increases by only 1%. The decrease in unpaired electron density at the muon site with decreasing temperature for the Phenyl-SiNPs may be interpreted as an increase in conduction away from the muon site, which is similar to what is observed for conduction in metals, due to a reduction in the phonon excitations.[24]

Table 6. CASTEP results for the tetrakis (2-phenylethynyl) silane and the Pheny-SiNPs

System	Total charge (e)	Total electronic density (e)	Spin up (hbar/2)	Spin down (hbar/2)	Total spin (hbar/2)	Aμ (MHz)
6 ang. Phenyl-SiNPs	0.310	0.680	0.360	0.320	0.04	323.97
tetrakis(2-phenylethynyl)silane	0.306	0.694	0.375	0.319	0.056	436.59

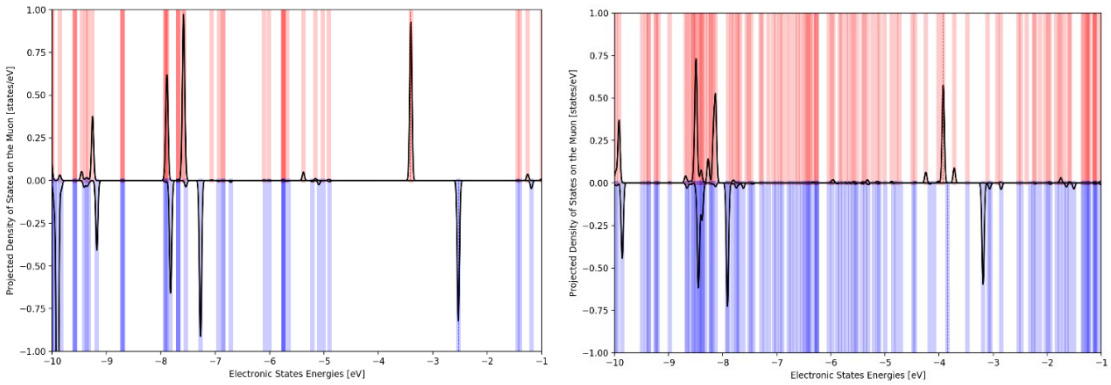

Figure 42. The calculated electronic energy states of the tetrakis(2-phenylethynyl) silane muoniated molecule (left) and those of the muonated 6 ang (right).The calculated electronic energy states of the tetrakis(2-phenylethynyl) silane muoniated molecule (left)

As mentioned in Chapter 2, the muon stopping sites in both the model compound and the Phenyl-SiNPs were studied using Density Functional Tight Binding (DFTB) calculations in the DFTB+ code, and standard DFT calculations in the CASTEP code. The calculation was performed with the aid from Dr Leandro Miguel Liborio and Dr Simone Sturniolo. Figure 42 shows the calculated electronic energy states of the model compound (left) and those of the muoniated 6 ang. Phenyl-SiNPs with six ligands attached to it (right). These calculations were done with CASTEP. The red and blue vertical stripes represent the electronic energy states for the up and down spin channels, and the black plots superimposed on these electronic energy states- represent the projected electronic states associated to the muon. The dotted vertical lines are the calculated Fermi energies.

The electronic structure of the model compound shows a peak on the density of states at the Fermi energy in both channels, which indicates that there is a strong component of muon states at those energy levels. As muoniated model compound tetrakis(2-phenylethynyl) silane is a radical that has one unpaired electron in its highest occupied molecular orbital (HOMO), the combination of muon and electronic states at the Fermi level is what explains the relatively large values of the Aμ in this model compound.

Furthermore, the electronic structure of the model compound shows a semiconductor-type minimum band-gap of approximately 1 eV in the down spin channel. No sensible increase in temperature will be able to allow the electrons in the HOMO to jump to the next energy levels and, therefore, the value of the Aμ of the muon is unlikely to go down.

As regards the muoniated Phenyl-SiNPs, its electronic states resemble more the band structure of a metallic system, where there are several bands all close together in energy in its electronic structure. We expect these discrete states to come closer and closer to a continuum as the particle gets bigger, as metallic behaviour at the surface of Si nanoparticles is a known phenomenon.[25] However, in this case the projected density of states associated with the muon are not exclusively at the Fermi level anymore, rather they are smeared above and below it. This combination of distributed muon states and metallic behaviour help explain why the Aμ in muoniated Phenyl-SiNPs is smaller than in the model compound.

The electronic structure of the muoniated Phenyl-SiNPs systems also offers a qualitative explanation of the temperature dependence of Aμ. For the real nanoparticles, the energy states at the Fermi level will likely form a continuum and, as the temperature increases, it

would be easier for an electron in a band close to the Fermi level to jump to the next energy level, as the levels will all be quite close to each other. If the new occupied level had a smaller contribution to the hyperfine coupling it would end up lowering the total coupling.

Moreover, the calculated electronic structures of the model compound and muoniated Phenyl-SiNPs systems also help explain the ALC-μSR results presented in Figure 40.

The metallic-type electronic structure of the Phenyl-SiNPs is correlated with a larger electronic delocalization of its unpaired electron when compared to the unpaired electron in the tetrakis(2-phenylethynyl) silane model compound, whose electronic structure has a relatively large band gap that would make electronic delocalization more difficult. The larger electronic delocalisation in the Phenyl-SiNPs can affect affect the the bonds between the phenyl ring and the Si nanoparticle: rather than having a single-triple-single bond order, the electronic delocalisation may produce a different bond order that will likely affect the single bonds and increase the energy barrier for the phenyl rotation in the Phenyl-SiNPs, which is what is observed in the ALC-μSR results presented in Figure 40.

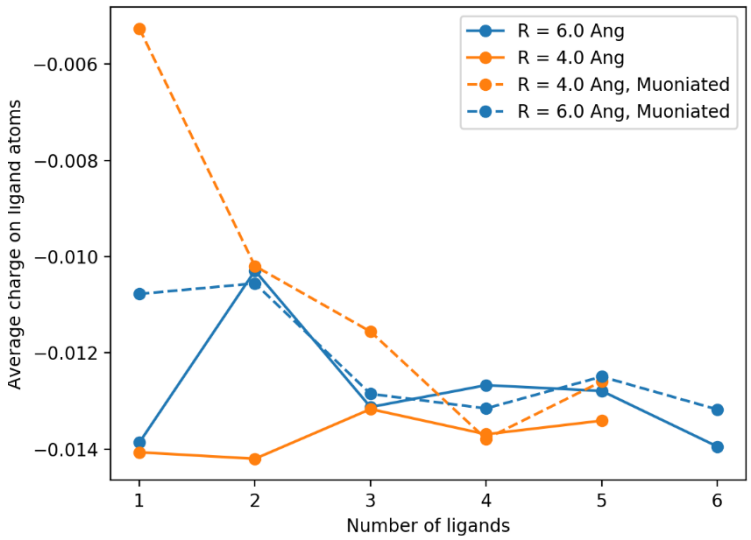

Figure 43. DFTB+ average Mulliken charges of the organic ligands as a function of the average radius of the silicon nanoparticles and the number of attached organic ligands. Nanoparticles with average diameters of 5 and 6 Å are shown.

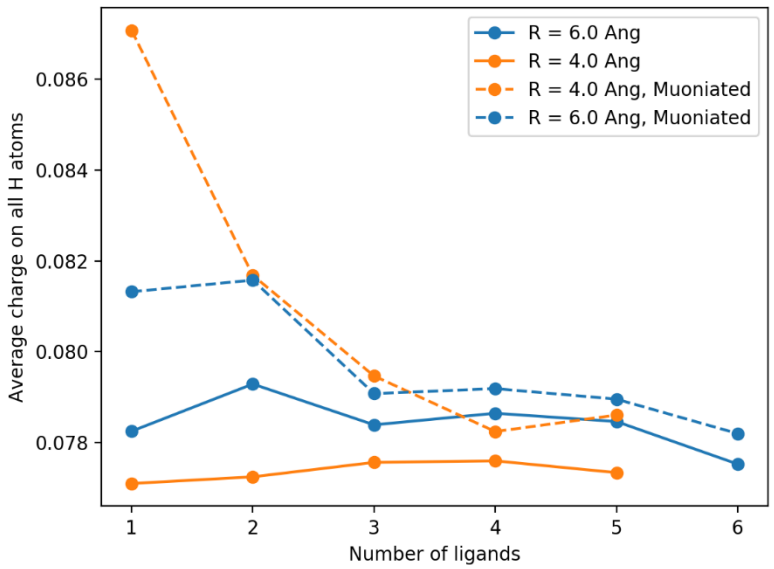

Figure 44. DFTB+ average Mulliken charges of the hydrogen atoms in the organic ligands as a function of the average radius of the silicon nanoparticles and the number of attached organic ligands. Nanoparticles with average diameters of 5 and 6 Å are shown. A maximum of 5 organic ligands could be attached to the 5 Å Si nanoparticles

The purpose of our simulations is to model the effect of transforming the silicon atom in the model compound into a silicon nanoparticle with a high surface coverage of organic ligands. Hence, we had to develop an adequate physical model for the Phenyl-SiNPs that was, on one hand, large enough to represent the properties that were experimentally observed and, on the other hand, small enough to be computationally manageable.

As the main property that we are simulating in this work is the Fermi contact terms A_μ and A_p of the muon and ipso hydrogen, we analysed the electronic charge in the organic ligands and, in particular, in the hydrogen atoms, as a function of the Phenyl-SiNPs size.

We built the nanoparticles using the Wulff construction method, which gives the crystal shape under equilibrium conditions.[26, 27] In this construction, the distance of a facet from the crystal centre is proportional to the surface energy of that facet, and the inner convex hull of all facets form the Wulff shape. For the construction of our nanoparticles, we used the (100), (111), (322) and (320) facets, and radii of 3 to 6 Å Then we radially attached 1 to 6 organic ligands to Si atoms in the nanoparticle. These ligands were distributed around the nanoparticle using a repulsion algorithm,[28] which secures the maximum possible angular distance between these ligands. Due to their size, no more than five organic ligands could be attached to the 5 Å Si nanoparticles.

Figure 43 and Figure 44 show the DFTB+ average Mulliken charges, expressed in atomic units, of the organic ligands, and their corresponding hydrogen atoms, attached to Phenyl-SiNPs. The nanoparticles shown have average diameters of 4 and 6 Å and an increasing number of organic ligands attached to them. The nanoparticles with an average diameter of 6 Å and 6 organic ligands attached to them have average Mulliken charges converged to a tolerance smaller than 0.005(e). These 6 ang. nanoparticles are composed of 30 silicon atoms, which is a size at which Si nanoparticles start showing properties which are characteristic of a nanoparticle-like state, i.e.: a state that is in-between the single Si atom and crystalline Si.[29, 30] Hence, we adopted these 6 Å 6 ligands Phenyl-SiNPs as representative of the experimental Si nanoparticles.

The geometries of the Phenyl-SiNPs were relaxed using first DFTB+ and then CASTEP, using the parameters indicated in the previous subsection.

4.5 Conclusions

In summary, μSR measurements have shown that there is a difference in the electronic structure of the Phenyl-SiNPs and the tetrakis(2-phenylethynyl) silane model compound. In particular, the μSR measurements have shown that the spin density on the muon is greatly reduced for the Phenyl-SiNPs system compared to the model compound. The low temperature values of the of Aμ are of the order of 450 MHz and 350 MHz for the model compound and the Phenyl-SiNPs respectively. Furthermore, the changes of the relative values of Aμ with temperature in the Phenyl-SiNPs are 30 times larger than in the model compound. This suggests that the Phenyl-SiNPs have much stronger thermoelectric behaviour than the model compund.

A computational study using both DFTB+ and CASTEP supports these results, while also offering a qualitative explanation for the change in the bonding between the Si nanoparticles and the Phenyl rings and for the temperature dependence of Aμ in both the Phenyl-SiNPs and the model compound. Calculations indicate that the Phenyl-SiNPs have a metal-type electronic structure, while the model compound have a semiconductor-type electronic structure. This variation in the electronic structure of both systems, suggests a mechanism for enhanced electron transport in the Phenyl-SiNPs system.

This combined μSR and computation study has therefore provided insight into the enhanced thermoelectric properties of Phenyl-SiNPs, and has also allowed us to propose a microscopic mechanism that explains this thermoelectric behaviour.

4.6 Reference

1. Réotier, P. D. d.; Yaouanc, A., Muon spin rotation and relaxation in magnetic materials. *J. Phys.: Condens. Matter* **1997,** *9*, 9113.

2. Hempelmann, R.; Soetratmo, M.; Hartmann, O.; Wappling, R., Muon diffusion and trapping in proton conducting oxides. *Solid State Ionics* **1998,** *107*, 269-280.

3. Drew, A. J.; Hoppler, J.; Schulz, L.; Pratt, F. L.; Desai, P.; Shakya, P.; Kreouzis, T.; Gillin, W. P.; Suter, A.; Morley, N. A.; Malik, V. K.; Dubroka, A.; Kim, K. W.; Bouyanfif, H.; Bourqui, F.; Bernhard, C.; Scheuermann, R.; Nieuwenhuys, G. J.; Prokscha, T.; Morenzoni, E., Direct measurement of the electronic spin diffusion length in a fully functional organic spin valve by low-energy muon spin rotation. *Nat. Mater.* **2009,** *8* (2), 109-114.

4. Sugiyama, J.; Nozaki, H.; Umegaki, I.; Mukai, K.; Miwa, K.; Shiraki, S.; Hitosugi, T.; Suter, A.; Prokscha, T.; Salman, Z.; Lord, J. S.; Månsson, M., Li-ion diffusion in Li4Ti5O12 and LiTi2O4 battery materials detected by muon spin spectroscopy. *Phys. Rev. B* **2015,** *92* (1), 014417.

5. McKenzie, I.; Scheuermann, R.; Sedlak, K.; Stoykov, A., Molecular Dynamics in Rod-Like Liquid Crystals Probed by Muon Spin Resonance Spectroscopy. *The Journal of Physical Chemistry B* **2011,** *115* (30), 9360-9368.

6. Walker, D. C., *Muon and Muonium Chemistry*. Cambridge University Press: Cambridge, 1983.

7. Hendricks; , T.; Choate, W. T. *Engineering Scoping Study of Thermoelectric Generator Systems for Industrial Waste Heat Recovery*; US Department of Energy: 2006.

8. Ashby, S.; Thomas, J. A.; Garcia-Canadas, J.; Min, G.; Corps, J.; Powell, A. V.; Xu, H.; Shen, W.; Chao, Y., Bridging Silicon Nanoparticles and Thermoelectrics: Phenylacetylene Functionalization. *Faraday Discuss.* **2014,** *176*, 349-361.

9. Kang, Z.; Liu, Y.; Lee, S. T., Small-sized silicon nanoparticles: new nanolights and nanocatalysts. *Nanoscale* **2011,** *3* (3), 777-91.

10. Buriak, J. M., Organometallic chemistry on silicon and germanium surfaces. *Chem. Rev.* **2002,** *102* (5), 1271-1308.

11. McKenzie, I., The positive muon and [small mu]SR spectroscopy: powerful tools for investigating the structure and dynamics of free radicals and spin probes in complex systems. *Annu. Rep. Prog. Chem., Sect. C: Phys. Chem.* **2013,** *109* (0), 65-112.

12. Baldwin, R. K.; Pettigrew, K. A.; Garno, J. C.; Power, P. P.; Liu, G.-y.; Kauzlarich, S. M., Room Temperature Solution Synthesis of Alkyl-Capped Tetrahedral Shaped Silicon Nanocrystals. *J. Am. Chem. Soc.* **2002,** *124* (7), 1150-1151.

13. Roduner, E.; Stolmár, M.; Dilger, H.; Reid, I. D., Reorientational Dynamics of Cyclohexadienyl Radicals in High-Silica ZSM-5. *J. Phys. Chem. A* **1998,** *102* (39), 7591-7597.

14. Clayden, N. J., Muons in chemistry. *Phys. Scr.* **2013,** *88* (6), 068507.

15. Bian, T.; Peck, J. N.; Cottrell, S. P.; Jayasooriya, U. A.; Chao, Y., Hybrid Silicon Nanostructures with Conductive Ligands and Their Microscopic Conductivity. *J. Electron. Mater.* **2017,** *46* (5), 3221-3226.

16. Pratt, F. L., WIMDA: a muon data analysis program for the Windows PC. *Phys. B* **2000,** (289-290), 710-714.

17. Pratt, F. L., Muon spin relaxation as a probe of electron motion in conducting polymers Muon spin relaxation as a probe of electron motion in. *J. Phys.: Condens. Matter* **2004,** *16*, S4779.

18. Oganesyan, V. S.; Cammidge, A. N.; Hopkins, G. A.; Cotterill, F. M.; Reid, I. D.; Jayasooriya, U. A., Muon Spin Rotation Studies of Enediynes. *J. Phys. Chem. A* **2004,** *108* (10), 1860-1866.

19. Lord, J. S.; McKenzie, I.; Baker, P. J.; Blundell, S. J.; Cottrell, S. P.; Giblin, S. R.; Good, J.; Hillier, A. D.; Holsman, B. H.; King, P. J. C.; Lancaster, T.; Mitchell, R.; Nightingale, J. B.; Owczarkowski, M.; Poli, S.; Pratt, F. L.; Rhodes, N. J.; Scheuermann, R.; Salman, Z., Design and commissioning of a high magnetic field muon spin relaxation spectrometer at the ISIS pulsed neutron and muon source. *Rev. Sci. Instrum.* **2011,** *82* (7), 073904.

20. Khasanov, R.; Guguchia, Z.; Maisuradze, A.; Andreica, D.; Elender, M.; Raselli, A.; Shermadini, Z.; Goko, T.; Knecht, F.; Morenzoni, E.; Amato, A., High pressure research using muons at the Paul Scherrer Institute. *High Pressure Res.* **2016,** *36* (2), 140-166.

21. Porezag, D.; Frauenheim, T.; Köhler, T.; Seifert, G.; Kaschner, R., Construction of tight-binding-like potentials on the basis of density-functional theory: Application to carbon. *Physical Review B* **1995,** *51* (19), 12947-12957.

22. Clark, S. J.; Segall, M. D.; Pickard, C. J.; Hasnip, P. J.; Probert, M. J.; Refson, K.; Payne, M. C., First principles methods using CASTEP. *ZKri* **2005,** *220* (5-6), 567-570.

23. Aradi, B.; Hourahine, B.; Frauenheim, T., DFTB+, a Sparse Matrix-Based Implementation of the DFTB Method. *J. Phys. Chem. A* **2007,** *111* (26), 5678-5684.

24. Elstner, M.; Porezag, D.; Jungnickel, G.; Elsner, J.; Haugk, M.; Frauenheim, T.; Suhai, S.; Seifert, G., Self-consistent-charge density-functional tight-binding method for simulations of complex materials properties. *Physical Review B* **1998,** *58* (11), 7260-7268.

25. Köhler, C.; Frauenheim, T., Molecular dynamics simulations of CFx (x=2,3) molecules at Si3N4 and SiO2 surfaces. *Surf. Sci.* **2006,** *600* (2), 453-460.

26. Sturniolo, S.; Liborio, L.; Jackson, S., Comparison between density functional theory and density functional tight binding approaches for finding the muon stopping site in organic molecular crystals. *J Chem Phys* **2019,** *150* (15), 154301.

27. Yang; Yu, H.; York, D.; Cui, Q.; Elstner, M., Extension of the Self-Consistent-Charge Density-Functional Tight-Binding Method: Third-Order Expansion of the Density Functional Theory Total Energy and Introduction of a Modified Effective Coulomb Interaction. *J. Phys. Chem. A* **2007,** *111* (42), 10861-10873.

28. Arnold, O.; Bilheux, J. C.; Borreguero, J. M.; Buts, A.; Campbell, S. I.; Chapon, L.; Doucet, M.; Draper, N.; Ferraz Leal, R.; Gigg, M. A.; Lynch, V. E.; Markvardsen, A.; Mikkelson, D. J.; Mikkelson, R. L.; Miller, R.; Palmen, K.; Parker, P.; Passos, G.; Perring, T. G.; Peterson, P. F.; Ren, S.; Reuter, M. A.; Savici, A. T.; Taylor, J. W.; Taylor, R. J.; Tolchenov, R.; Zhou, W.; Zikovsky, J., Mantid—Data analysis and visualization package for neutron scattering and μ SR experiments. *Nucl. Instrum. Methods Phys. Res., Sect. A* **2014,** *764*, 156-166.

29. Pratt, F. L.; Blundell, S. J.; Marshall, I. M.; Lancaster, T.; Husmann, A.; Steer, C.; Hayes, W.; Fischmeister, C.; Martin, R. E.; Holmes, A. B., μSR in polymers. *Phys. B* **2003,** *326* (1), 34-40.

30. Cros, A., Silicon surfaces: metallic character, oxidation and adhension. *J. Phys. France* **1983,** *44* (6), 707-711.

Chapter 5: Si-based anode material for lithium-ion battery

The following chapter describes the synthesis of hollow structured Si@TiO_2 and the techniques used to test the assembled batteries. A description of the LAND battery test system and CHI-660E electrochemical workstation is presented. The results of X-ray Electron Spectroscopy, Scanning Electron Microscope and X-ray Powder Diffraction are also discussed.

Content

5.1 Background

Silicon has very high energy capacity in theory; a comparison between silicon and common anode materials is shown in Table 7. Graphite is an anode material used widely in our daily lives. The theoretical specific capacity is 372 mah/g. Alloy-type anodes have a better ability to store Li than graphite anodes. However, silicon has up to ten times more graphite, up to 4200 mah/g, which is the highest known theoretical specific capacity. Li, Sn and Al have been widely studied as anode materials in research.[1-3]

Table 7. Comparison of different anode materials.

Anode materials	**C**	**Li**	**Si**	**Sn**	**Sb**	**Al**	**Mg**	**$Li_4Ti_5O_{12}$**	**Bi**
Lithiated phase	**LiC_6**	**Li**	**$Li_{4.4}Si$**	**$Li_{4.4}Sn$**	**Li_3Sb**	**LiAl**	**Li_3Mg**	**$Li_{12}Ti_5O_{12}$**	**Li_3Bi**
Theoretical specific capacity (mAh g^{-1})	**371**	**3862**	**4200**	**994**	**660**	**993**	**3350**	**175**	**385**
Theoretical volume capacity (mAh cm^{-3})	**837**	**2047**	**9786**	**7246**	**4422**	**2681**	**4355**	**613**	**3765**
Volume change (%)	**12**	**100**	**320**	**260**	**200**	**96**	**100**	**1**	**215**

With such high energy capacity, silicon will expand while cycling[4] (see Figure 45). Silicon has the highest theoretical specific capacity, but also the highest volume change. If the diameter of a silicon nanoparticle is over 150 nm, it will crack and fracture. The battery will be broken after that. Sizes smaller than 150 nm silicon nanoparticles will also expand. The design of a yolk-shell silicon nanoparticle would help to dissolve the expansion problem.

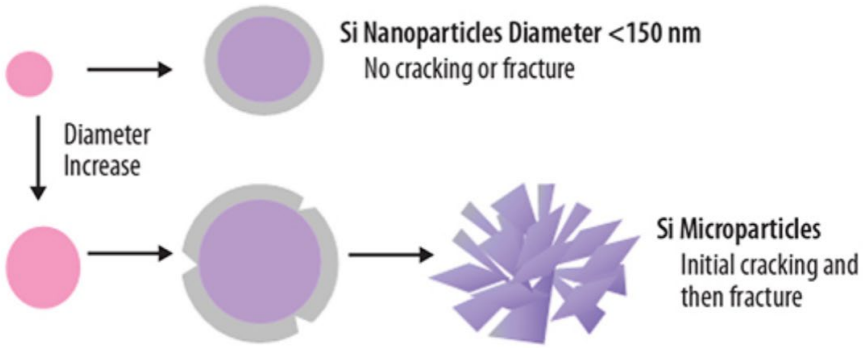

Figure 45. Different cracking or fracture with different sizes of silicon nanoparticles

5.2 Synthesis of hollow structured Si@TiO_2

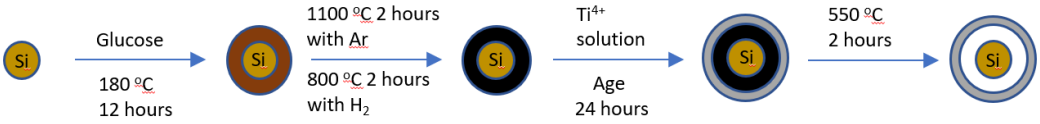

Figure 46. Synthesis of hollow structured Si@TiO_2

To overcome the disadvantage of silicon, a titanium dioxide shell is designed to wrap the silicon nanoparticles. The procedure is shown in Figure 46.

Materials used for the synthesis are listed below:

Glucose, silicon nanoparticle (60 nm, Thermo Fisher), Titanium Isoproproxide, Ethanol, DI water.

Si@TiO_2 was prepared in a normal environment with the following procedure:

70 g glucose and 0.7 g silicon nanoparticles are mixed and sonicated in 70 ml DI water to get a dark brown suspension because silicon nanoparticles will not dissolve in DI water. The dark brown suspension needs to be transferred into a Teflon reaction still and fixed into a stainless stell autoclave, then put the autoclave into the oven and heat at 180 °C for 8 hours. After heating, centrifuge the product 3 times at 10000 rpm for 10 min is required to wash

away the extra glucose. The dark brown slurry left after centrifuging was dried under vacuum for 4 hours to get dry powder. After that, 20 ml of titanium isoproproxide contained Ti^{4+} and 30 ml of ethanol were mixed and sonicated to make sure that the Si@C is spread properly and then age the mixture for 12 hours. The aged suspension needs to be washed three times with centrifuge to remove the extra Ti^{4+}. The white mass left after wash was dried in the oven at 40 ºC for 4 hours to get white powder. The white powder is heated in the furnace at 550 ºC for 2 hours with 5 ºC heating rate to get final product which is brown and white solid.

Owing to its low structural strain and non-toxicity, TiO_2 has gained immense attention as a safe electrode material for lithium-ion batteries (LIBs). It has been reported to be a superb anode material because of its great chemical stability.[5, 6] Titanium is used as part of anode materials with high specific capacity materials, such as Li and Al, to improve the stability of this kind of anode material[1, 3] In this study, Ti^{4+} in ethanol was used to react with oxygen to give a TiO_2 shell outside the silicon nanoparticles. This shell is a safe electrode and helps prevent the extension of silicon while charging and discharging.

5.3 Synthesis of adjusted hollow structured Si@TiO_2

Based on the battery performance achieved from the previous recipe, the specific capacity was lower than expected and similar to TiO_2. The TiO_2 shell outside the silicon core is too thick. The XPS survey also proved this, see Figure 49. The amount of Ti^{4+} needed to be reduced to obtain a thinner shell. Then the adjusted procedure is shown below.

Materials used for the synthesis: Glucose, silicon nanoparticle (60 nm, Thermo Fisher), Titanium Isoproproxide, Ethanol and DI water.

The amounts used in the synthesis of Si@TiO_2 were adjusted. The updated procedure is shown below:

70 g glucose and 0.7 g silicon nanoparticles are mixed and sonicated in 70 ml DI water to get a dark brown suspension because silicon nanoparticles will not dissolve in DI water. The dark brown suspension needs to be transferred into a Teflon reaction still and fixed into a stainless stell autoclave, then put the autoclave into the oven and heat at 180ºC for 8 hours. After heating, centrifuge the product 3 times at 10000 rpm for 10 min is required to wash away the extra glucose. The dark brown slurry left after centrifuging was dried under

vacuum for 4 hours to get dry powder. After that, 5 ml of titanium isoproproxide contained Ti^{4+} and 30 ml of ethanol were mixed and sonicated to make sure that the Si@C is spread properly and then age the mixture for 12 hours. The aged suspension needs to be washed three times with centrifuge to remove the extra Ti^{4+}. The white mass left after wash was dried in the oven at 40°C for 4 hours to get white powder. The white powder is heated in the furnace at 550 °C for 2 hours with 5 °C heating rate to get final product which is brown and white solid.

5.4 Characteristics of Si@TiO_2

5.4.1 X-ray Photoelectron Spectroscopy

XPS is a surface technique. The XPS survey spectrum obtained from pure silicon nanoparticles is shown in Figure 47, and the XPS survey spectrum of Si@C with high resolution of Si 2p, O1s and C1s is shown in Figure 48. The XPS survey spectrum of Si@TiO_2 (high amount of TiO_2) and a high resolution of Si 2p and Ti 2p is shown in Figure 49, and the XPS survey spectrum of Si@TiO_2 (low amount of TiO_2) and high a resolution of Si 2p and Ti 2p is shown in Figure 50.

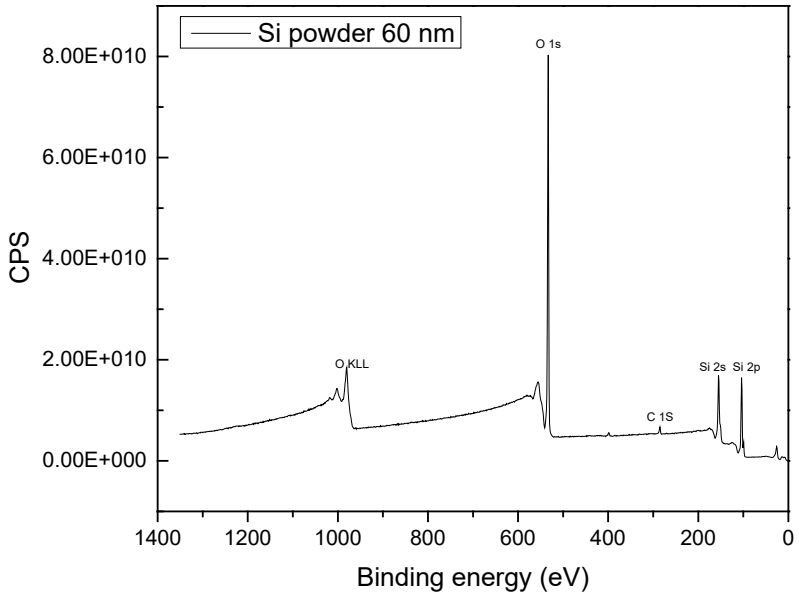

Figure 47. XPS survey spectrum obtained from Si powder (Step: 1 eV)

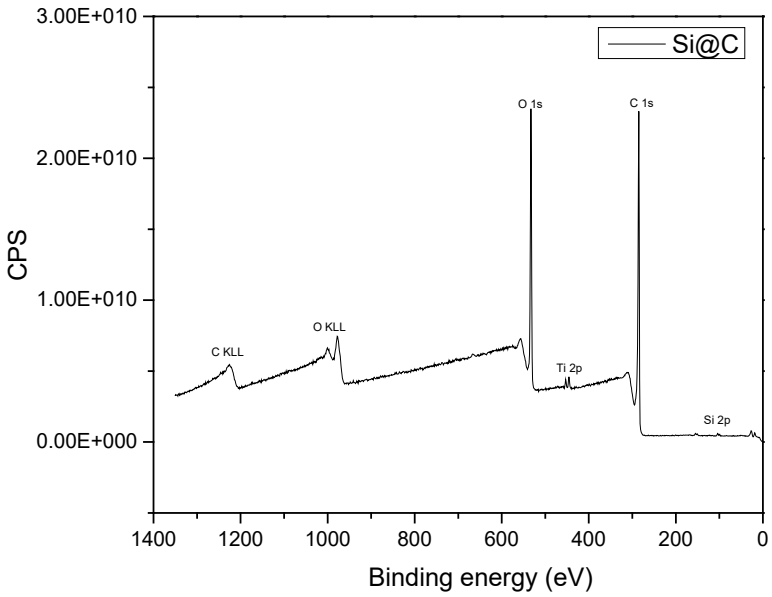
Si@C
O 1s
C 1s
C KLL
O KLL
Ti 2p
Si 2p
CPS
Binding energy (eV)

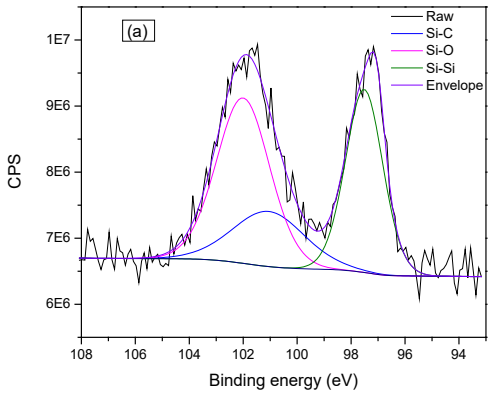
(a)
Raw
Si-C
Si-O
Si-Si
Envelope
CPS
Binding energy (eV)

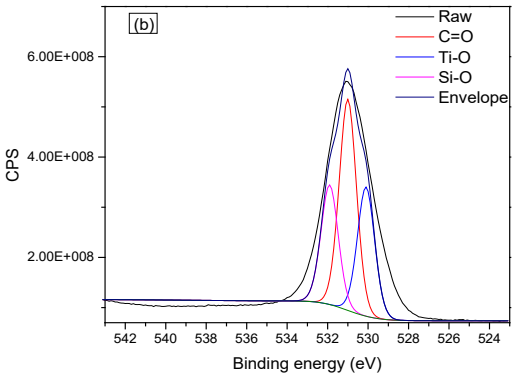
(b)
Raw
C=O
Ti-O
Si-O
Envelope
CPS
Binding energy (eV)

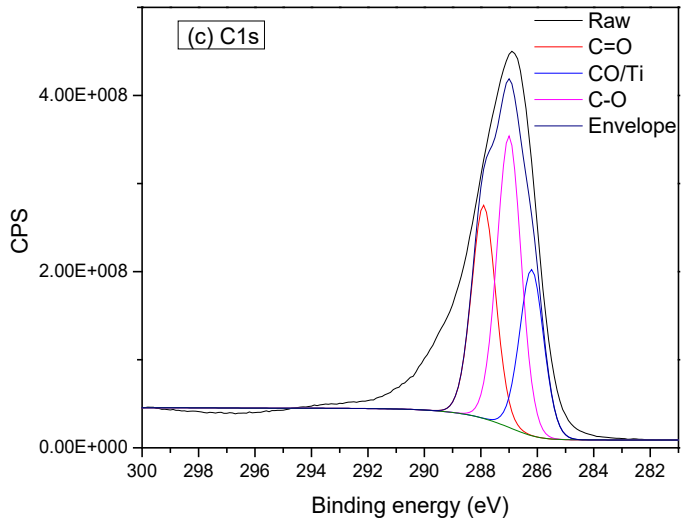

Figure 48. XPS survey spectrum obtained from Si@C with 1 eV step (a) high resolution spectrum obtained from Si@C showing Si2p region with 0.1 eV step (b) high resolution spectrum obtained from Si@C showing of O1s with 0.1 eV step (c) high resolution spectrum obtained from Si@C showing C1s region with 0.1 eV step

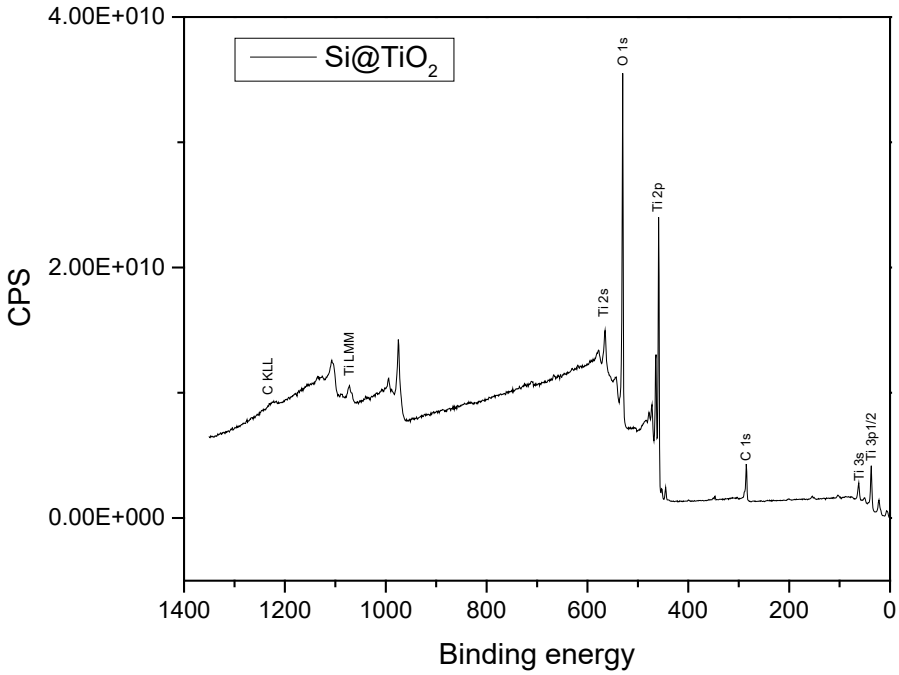

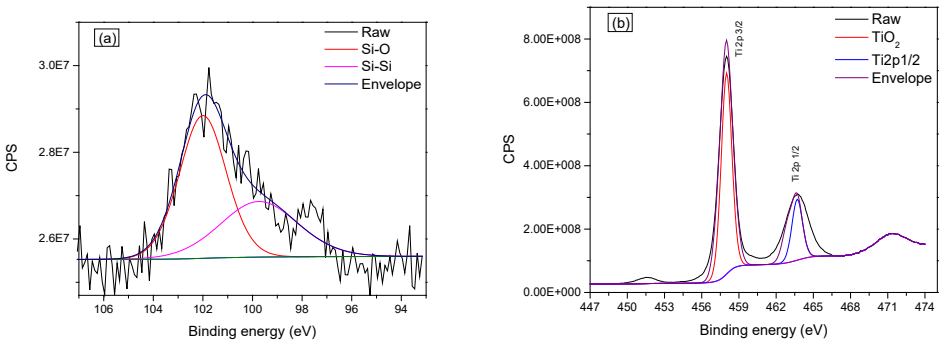

Figure 49. XPS survey spectrum obtained from Si@TiO_2 with 1 eV step (a) High resolution spectrum obtained from Si@TiO_2 showing Si2p region with 0.1 eV step (b) High resolution spectrum obtained from Si@TiO_2 showing Ti2p3/2 and Ti2p1/2 region with 0.1 eV step

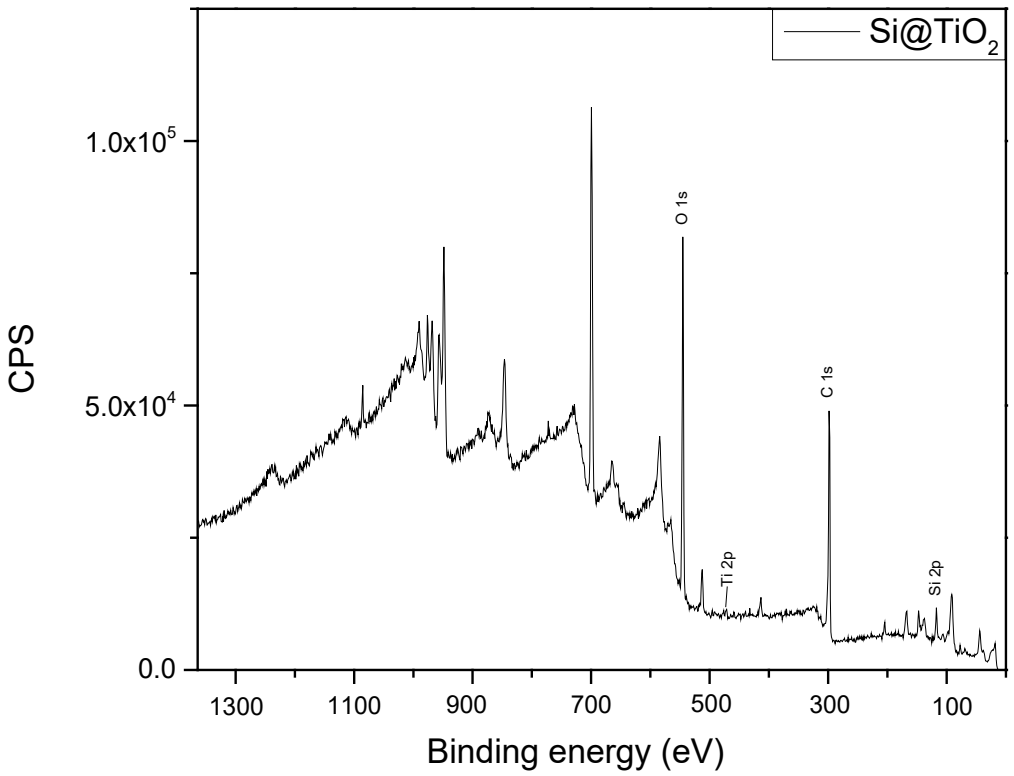

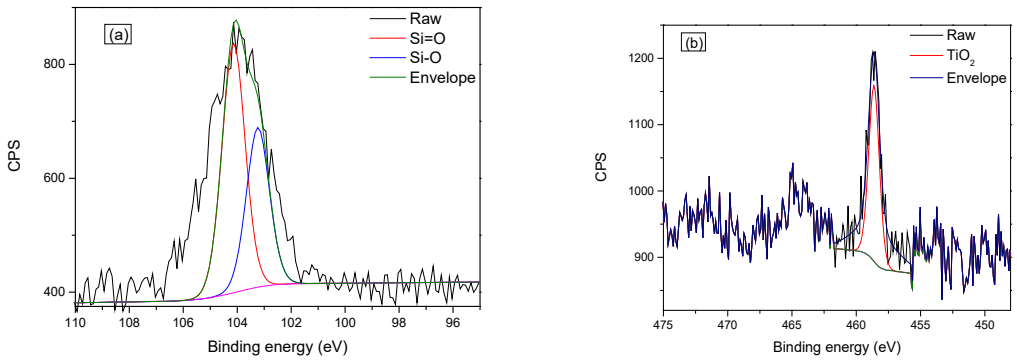

Figure 50. XPS survey spectrum obtained from Si@TiO_2 with less amount of titanium (a) High resolution obtained from Si@TiO_2 with less amount of titanium showing Si2p region with 0.1 eV step (b) High resolution obtained from Si@TiO_2 with less amount of titanium showing Ti2p3/2 region with 0.1 eV step

Figure 47 shows the XPS survey of pure 60 nm silicon nanoparticles with step of 0.1 eV. The major peaks are O1s and Si2s and Si2p. After heating silicon nanoparticles and glucose in oven at 180°C, there was a thick carbon shell outside the silicon nanoparticles. This is shown in Figure 48: a strong C1s peak appears and covers the signal from Si. XPS is a technique to detect the surface of materials. C1s is 77.46% and O1s is 21.55%. The signal from silicon is weak, and the percentage of silicon is 0.98% because the XPS is not able to analyse more than 5-10 nm. This proves that there should be a thick shell outside the silicon nanoparticle. But the sample is polluted by Ti during synthesis, there is Ti peak shown in the spectra.

The Si@C was aged with titanium isoproproxide and heated to 550°C in a furnace without air protection to react all the carbon with oxygen to obtain a hollow structured Si@TiO_2. From Figure 49, it can be observed that the Ti peak is much stronger than the C peak. There are Ti2p3/2 and Ti2p1/2, shown in Figure 49(b). Compared with Si2p, shown in Figure 49(a), the Si:Ti ratio is around 1:9. Silicon is 2.25% and Ti is 18.44%. The evidence shows that the carbon reacts with oxygen and a thick titanium dioxide shell is wrapped outside the silicon nanoparticles. However, the signal of Si is still covered. When analysing the XPS survey spectrum with the battery performance, it can be seen that the amount of Si is much lower than the amount of titanium. The specific capacity of titanium dioxide is around 200 mah/g. The high percentage of silicon may increase the specific capacity of the battery. The amount of titanium was therefore reduced to obtain a thinner shell outside the silicon nanoparticles. Figure 50 shows the XPS survey spectra after reducing the amount of titanium

isoproproxide when ageing. A signal from silicon is detected, and the signal from Ti is much lower than from Ti 2p. The atomic percentage of silicon was calculated as 8.75%, over 90 times more than the atomic percentage of Ti, which is 0.2%. This is evidence that the shell is thinner than in the previous sample.

5.4.2 X-ray Powder Diffraction

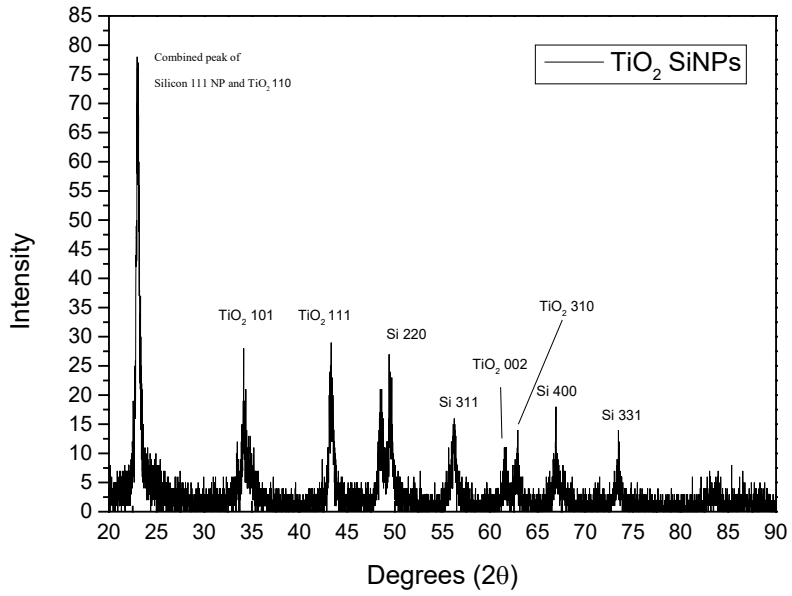

Figure 51. XRD spectrum obtained from Si@TiO2

The observations made using XPS are also visible in the XRD spectrum, shown as TiO_2. Silicon 111 NP, Si 220 and Si 400 are visible in Figure 51, which with the observation from XPS could prove that the silicon nanoparticles are wrapped by TiO_2.

5.4.3 Scanning Electron Microscope

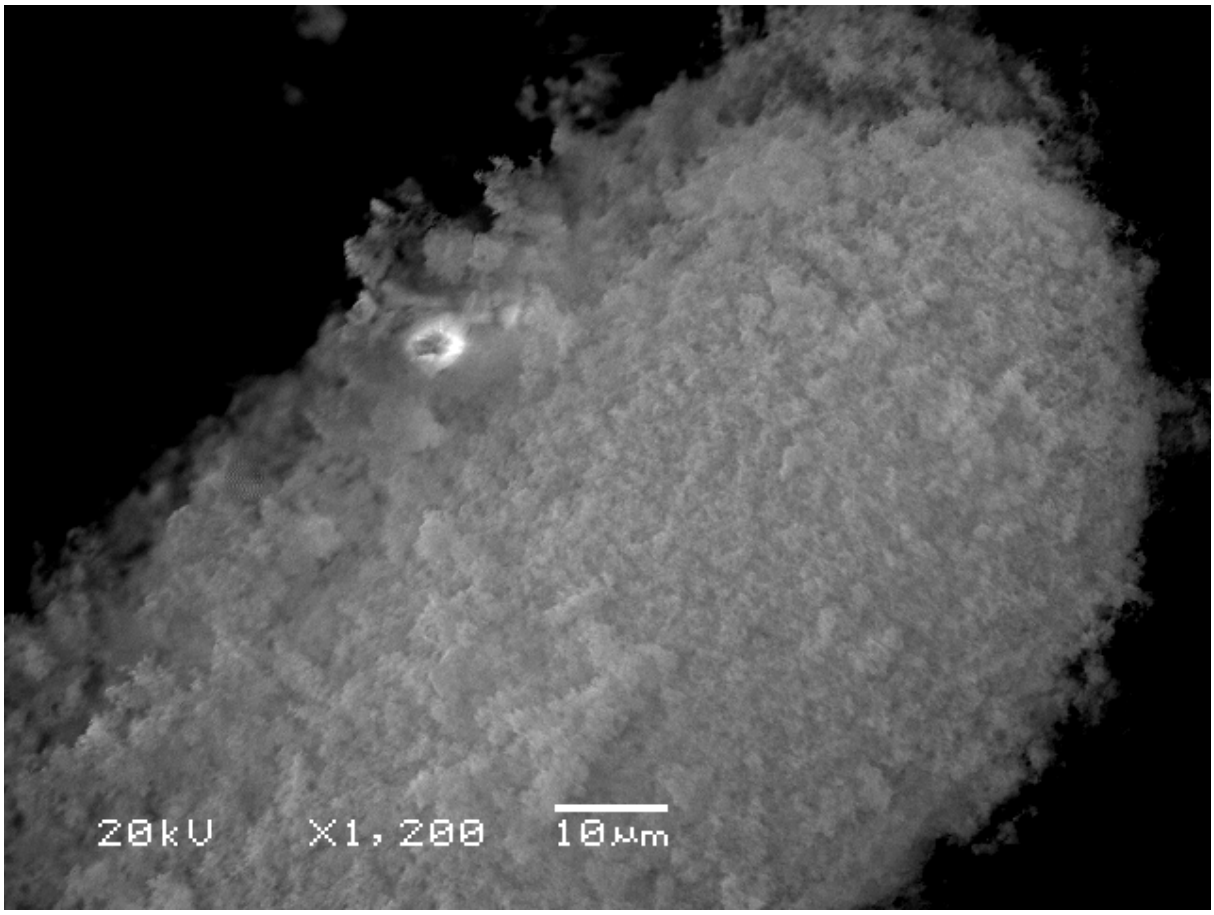

Figure 52. SEM image of raw 60 nm Si nanoparticles used for the synthesis

SEM was utilised to determine the size and shape of Si@TiO_2. It shows that TiO_2 might wrap multiple silicon nanoparticles together. From the image for the Si@TiO_2, multiple sizes of nanoparticles are obtained because not only one silicon nanoparticle is wrapped by the TiO_2 shell. If more than one nanoparticle is wrapped by the TiO_2 shell, its size and shape will be changed. The SEM image of raw silicon nanoparticles is shown in Figure 52. The size of the raw silicon nanoparticles used for the synthesis is only 60 nm; the resolution of SEM is not able to provide a clear image of these particles.

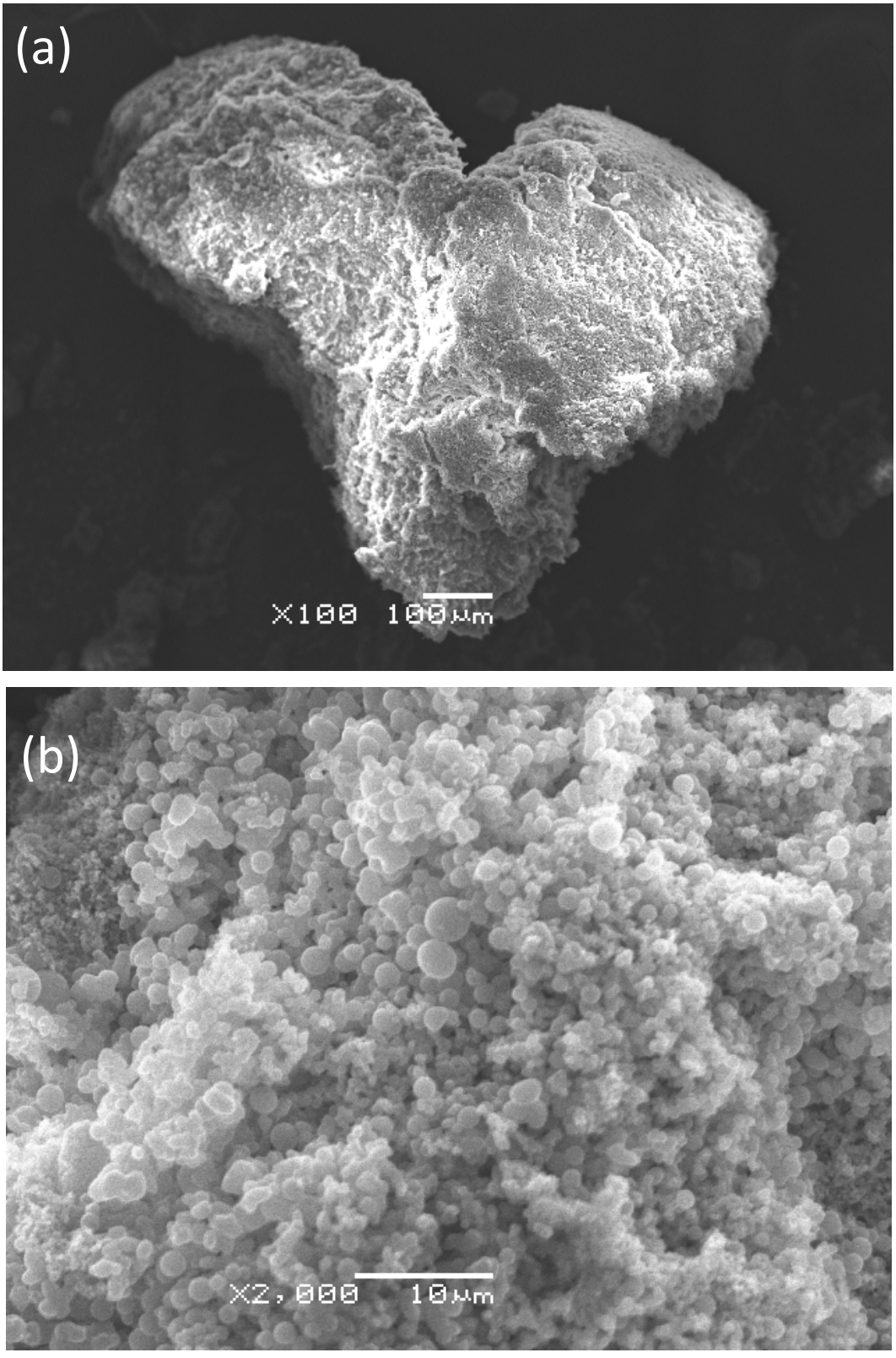

Figure 53. SEM images of Si@C. Si@C is the product after burning glucose and Si nanoparticles in the oven at 180°C, (a) SEM image with 100 µm scale, (b) SEM image with 10 µm scale

The 60 nm silicon nanoparticles were mixed with DI water and glucose. The mixture was heated to 180ºC for 12 hours. There was a thick carbon shell outside the silicon nanoparticles, around 500 nm in size. The SEM image is shown in Figure 53. The particles are larger than the raw material. This is also proved by the XPS survey of Si@C, where the percentage of C is 77.46%. The shell is so thick that the XPS can not receive a signal from the silicon nanoparticles inside.

The next step is ageing Si@C with titanium isoproproxide; the SEM image from Si@C@TiO_2 is shown in Figure 54. A thick titanium dioxide shell is not expected because it would not improve the battery performance. From the SEM image, it can be observed that the size is similar to that of Si@C. The titanium dioxide shell will be only several nannometers, so it is hard to tell the difference after ageing with titanium isoproproxide. The Si@C@TiO_2 was heated to 550ºC without any air protection. The solution of titanium isoprorpoxide contains Ti^{4+}, which will react with oxygen to give a TiO_2 shell. The ageing process is in solution, so not all the Ti^{4+} will change to TiO_2. This step will help to avoid Ti^{4+} and part of the carbon will react with oxygen as well. After burning away the carbon between silicon nanoparticles and TiO_2, the size will be similar to the previous Si@C or Si@C@TiO_2, but many anatase shells also merged with each other, thus forming connected yolk-shell Si@TiO_2 clusters, like biological tissue that contains many adjacent cells.[7]

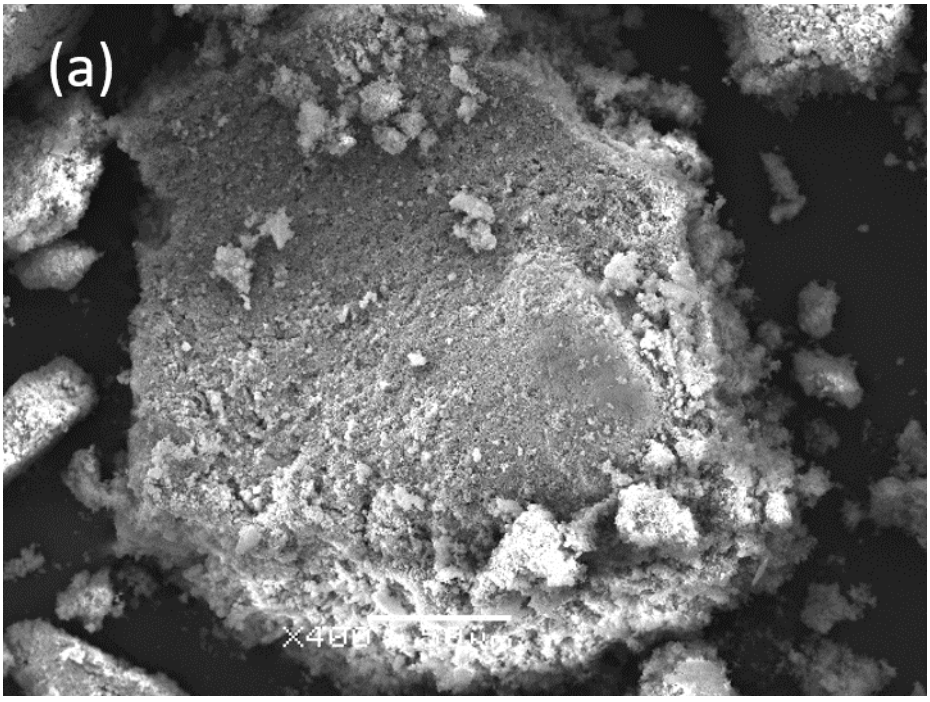

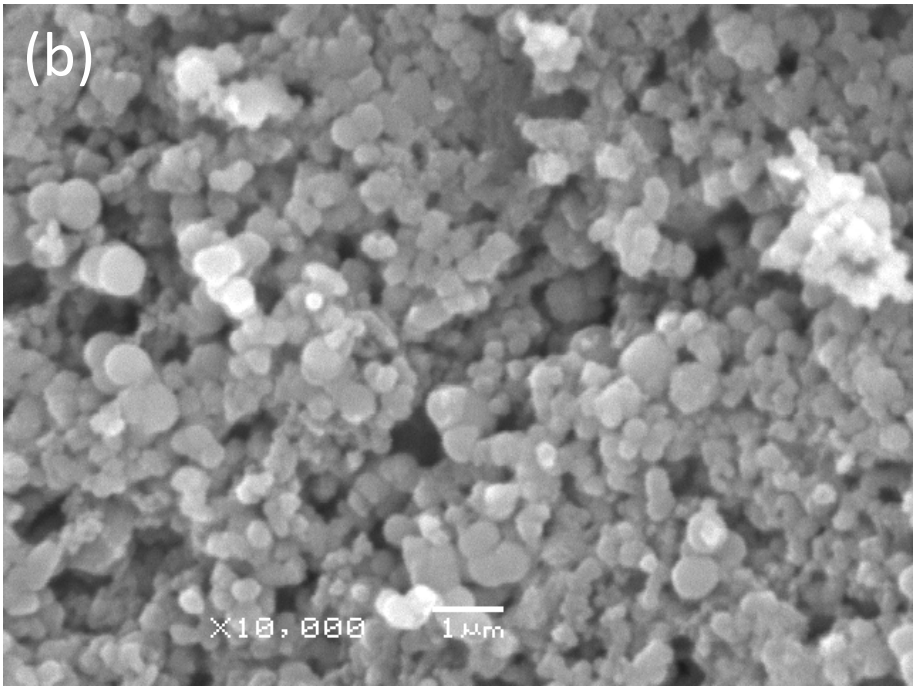

Figure 54. SEM images of Si@C@TiO_2 after ageing the Si@C with titanium isoproproxide with different scales, (a) SEM image with 50 µm scale, (b) SEM image with 10 µm scale

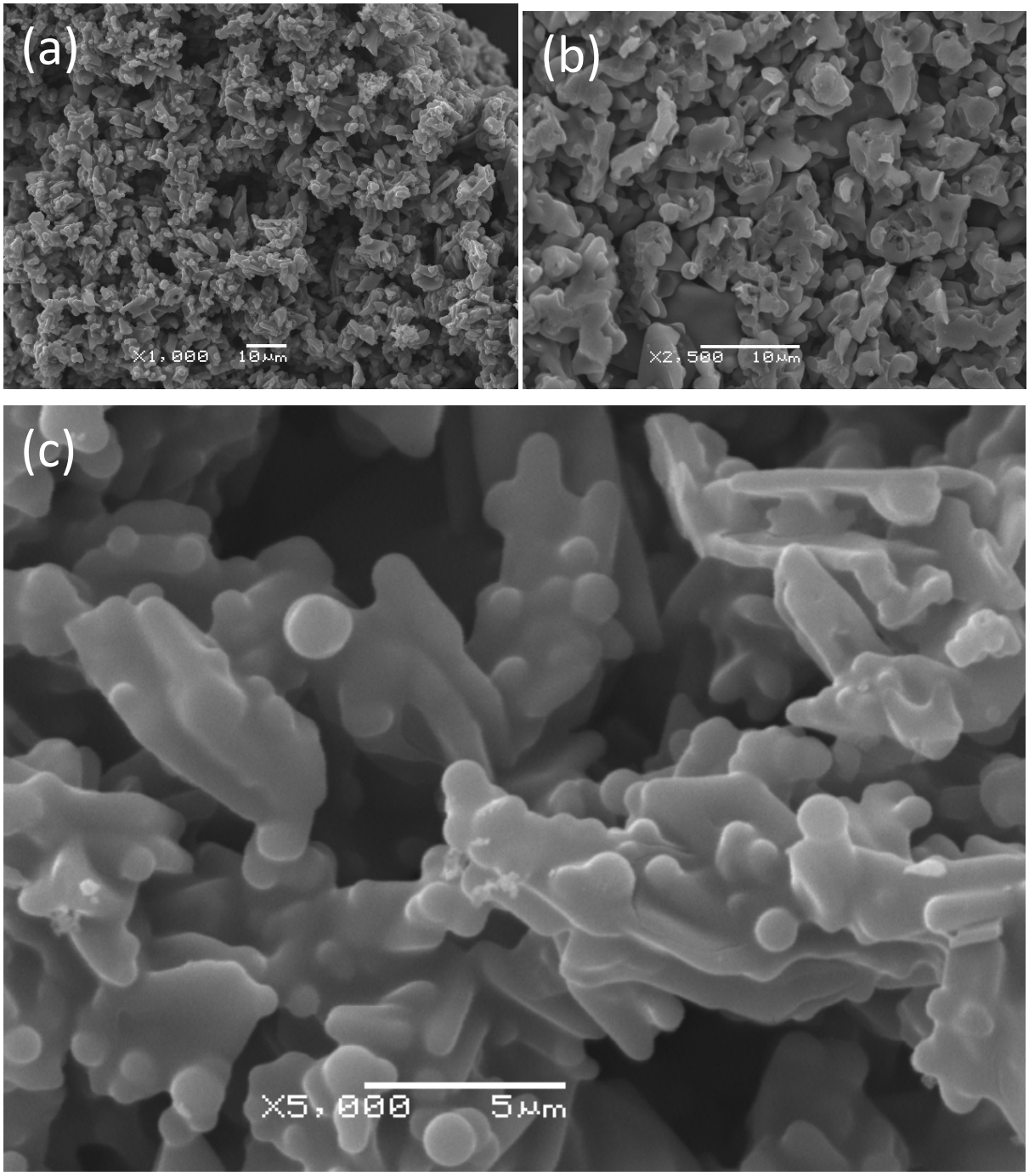
(a)
X1,000 10µm
(b)
X2,500 10µm
(c)
X5,000 5µm

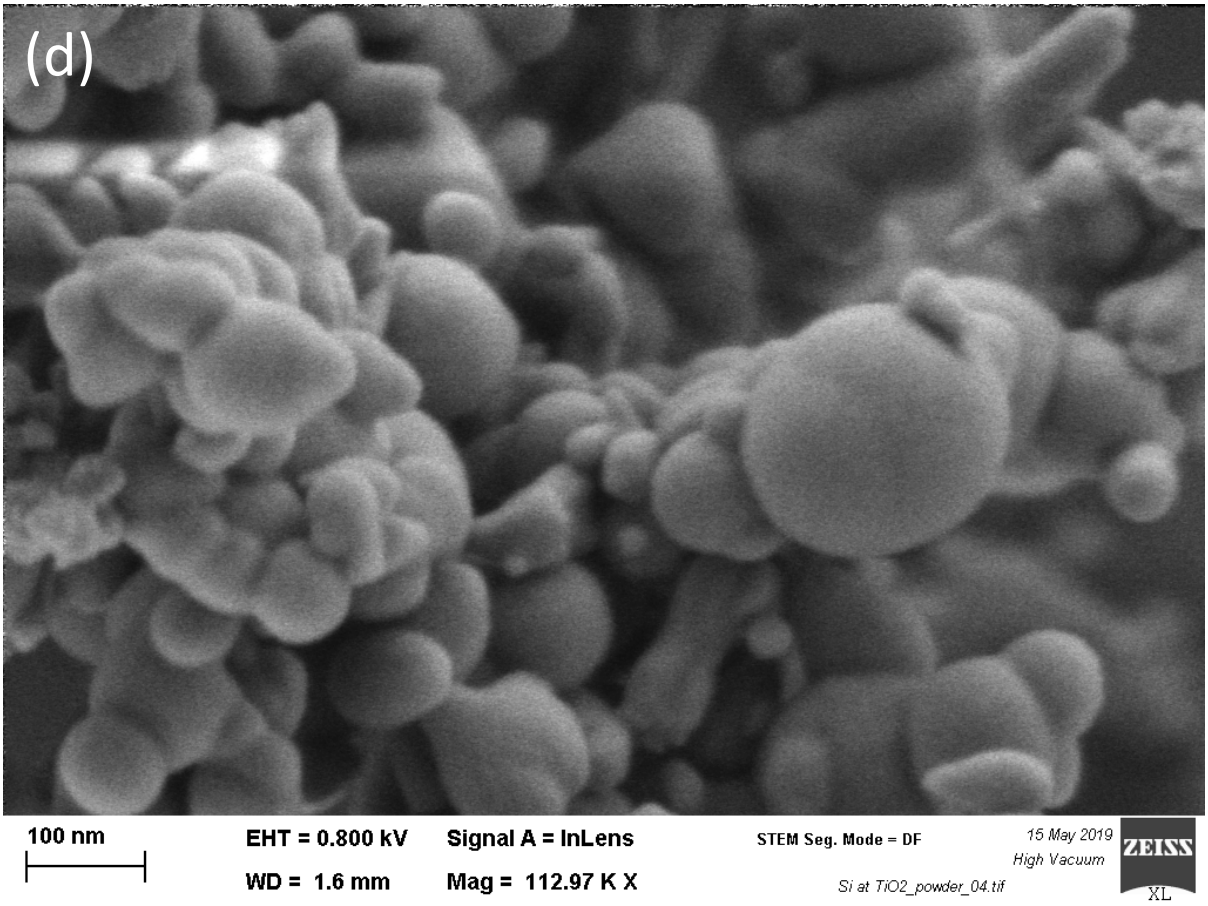

Figure 55. Higher resolution SEM images of Si@TiO_2, different shapes of Si@TiO_2 are shown, (a) SEM image with 10 µm scale, (b) SEM image of another part of the sample with 10 µm scale, (c) SEM image with 5 µm scale, (d) STEM image with 100 nm

5.5 Battery assembly procedure

To measure the performance of the battery with Si@TiO2 as the anode, carbon black, binder and our sample were mixed together. The mixture was coated with copper foil and cut to a 16 mm circle to fit the battery case.

Basic materials used for battery assembly were: PVDF (Polyvinylidene fluoride 50mg/ml), separator (Celgard), activated charcoal, 1-Methyl-2-pyrrolidone, lithium, foamed nickel and $LiPF_6$ in a mixture of ethylene carbonate/ dimethyl-carbonate/ethyl-methyl-carbonate (1:1:1).

Assembly is one of the important elements of battery capacity. The manufactory problem will fail the battery when the battery is tested. The assembly steps are shown in Figure 56:

1. Dry the sample completely.
2. Weigh 0.16g sample mixed with 80mg PVDF and 80mg graphite. Add 200µl 1-Methyl-2-pyrrolidone.
3. Stir the mixture for 12 hours to fully mix the sample.
4. Make sure the mixture has mobility. If it is too thick to flow, add more 1-Methyl-2-pyrrolidone. If it is too thin, stir for longer.
5. After stirring, use a coating device to paint the surface sample with copper foil.
6. After drying for 12 hours in the vacuum oven, use a tablet press machine to cut the copper foil with the sample into a circle. Then cut the copper foil separately to calculate the average weight of the copper foil.
7. Then put the round copper foil with the sample into the oven to dry them again.

In the glovebox:

The gas used for the glovebox is 95% N_2 and 5% H_2 to protect the oxygen sensitive materials. Put the circle of copper foil over the positive electrode battery case. Cover the copper foil with a separator. Then put the foamed nickel with a piece of lithium above them. Finally, drip on 3-4 drops of electrolyte and assemble the battery.

There are two common binder systems: PVDF+NMP and SBR+CMC. PVDF and SBR are the binders to make sure that the sample can be coated with the copper foil properly. NMP and CMC are used to make the powder of active materials and carbon black can be easily spread in the slurry. The solvent for SBR and CMC is DI water. The carbon black and Si@TiO_2 are lighter than water, so they cannot be mixed well in this system. PVDF and NMP do not have this problem.

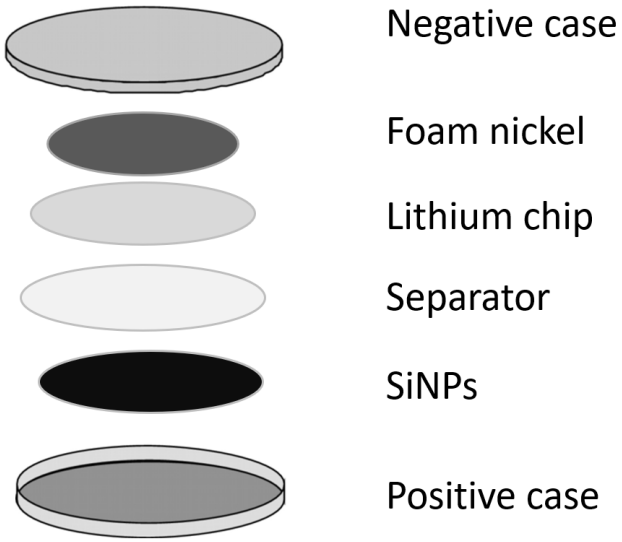

Figure 56. Assembled structure of coin cell

5.6 Half-cell and full-cell cycling test

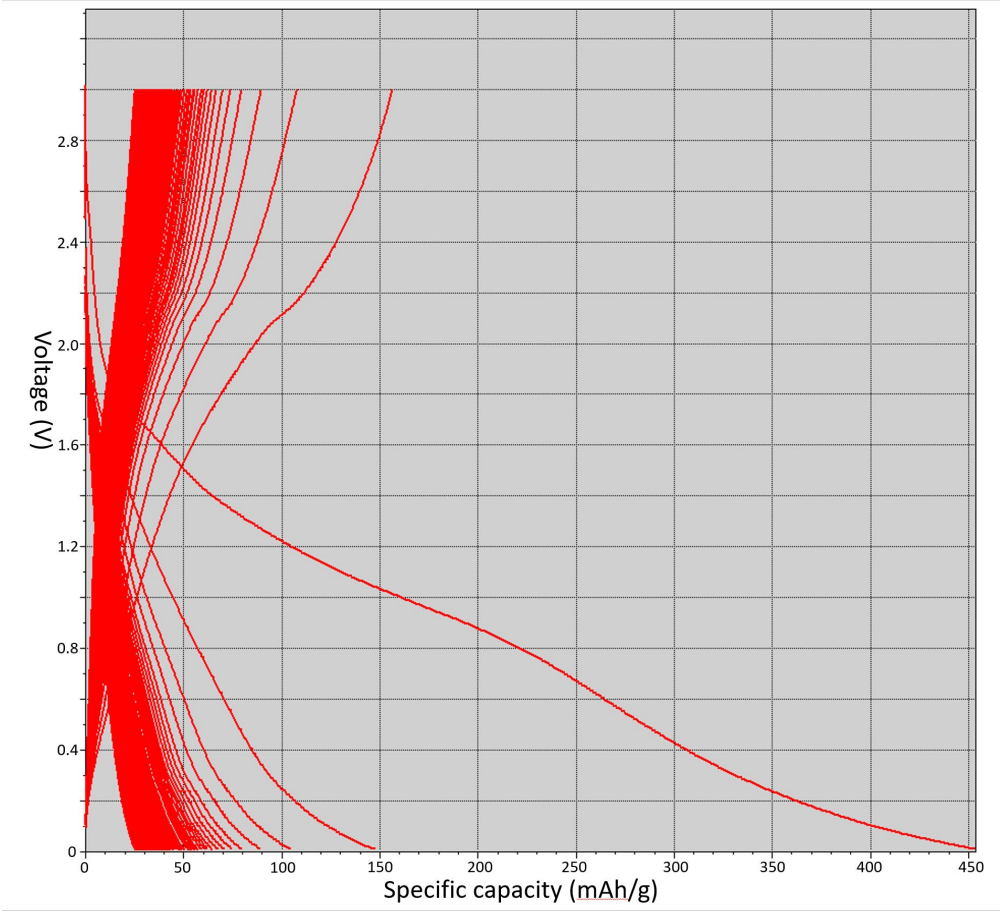

Figure 57. Cycling data from carbon black as a comparison with Si-based anode

The anode materials are assembled into a half cell. 1M $LiPF_6$+EC/DMC(1:1 v/v)+2% VC is chosen as the electrolyte. From Figure 57, it can be observed that the specific capacity of carbon black is lower than 150 mAh/g, which is also lower than the theory specific capacity: 372 mAh/g. The specific capacity of the first cycle can be up to 500 mAh/g. It will drop down rapidly in the second cycle.

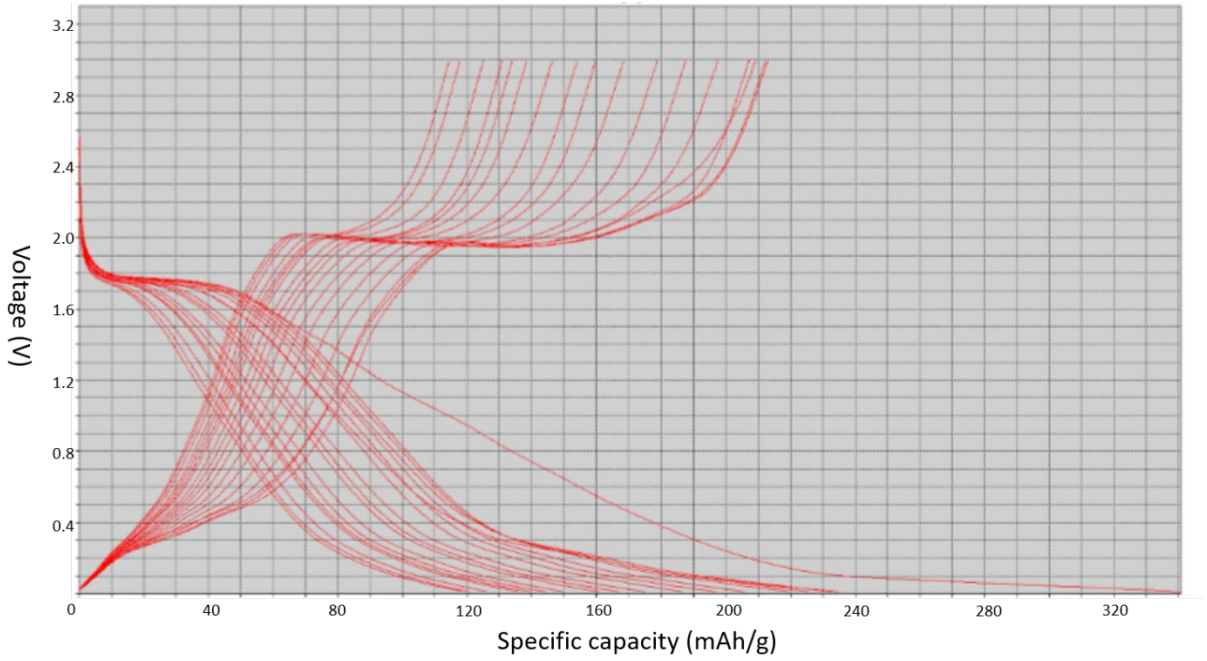

Figure 58. Cycling data from Si@TiO_2 (high amount of Ti)

Before the adjustment of the amount of titanium isoprorpoxide, the battery performance is shown in Figure 58 and Figure 59, when assembling the battery with the thicker titanium dioxide shell silicon nanoparticles.

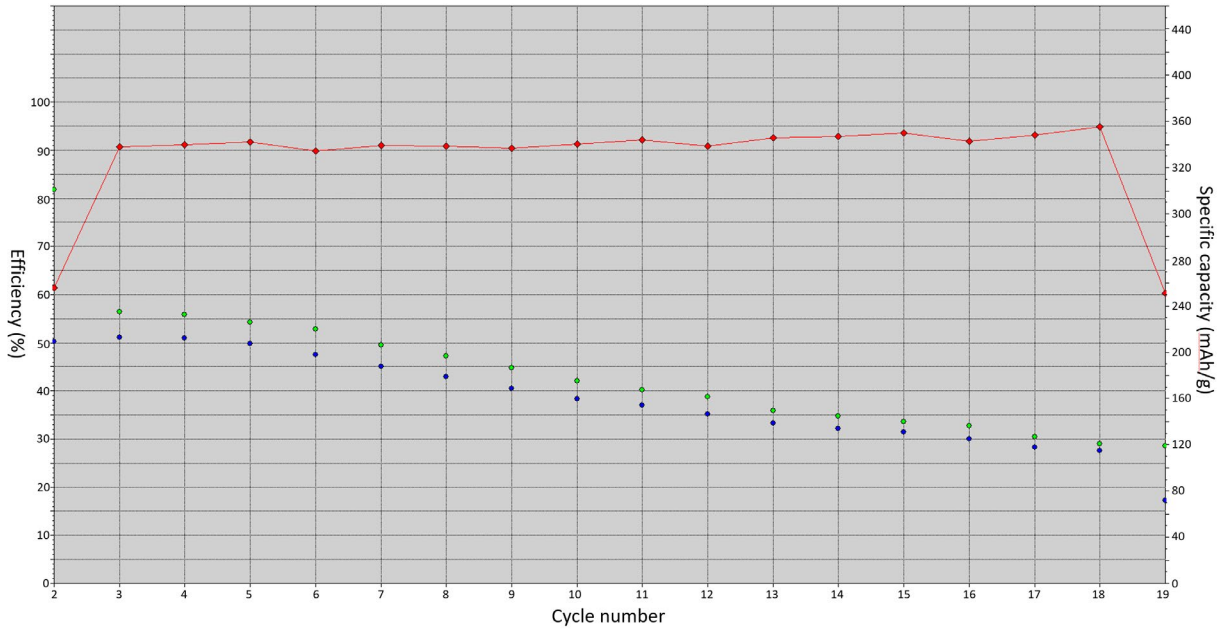

Figure 59. Columbic efficiency and specific capacity data from Si@TiO_2 (high amount of Ti)

The specific capacity of the higher amount of titanium is around 200 mAh/g; in the first cycle it can be up to 340 mAh/g, which is far away from the theory specific capacity of silicon and similar to the performance of titanium. The working voltage is around 1.8 V which is quite high when compared with silicon Combining this data with the previous XPS and XRD, the titanium dioxide shell is too thick, so the silicon does not contribute to the reaction during the charging and discharging cycles.

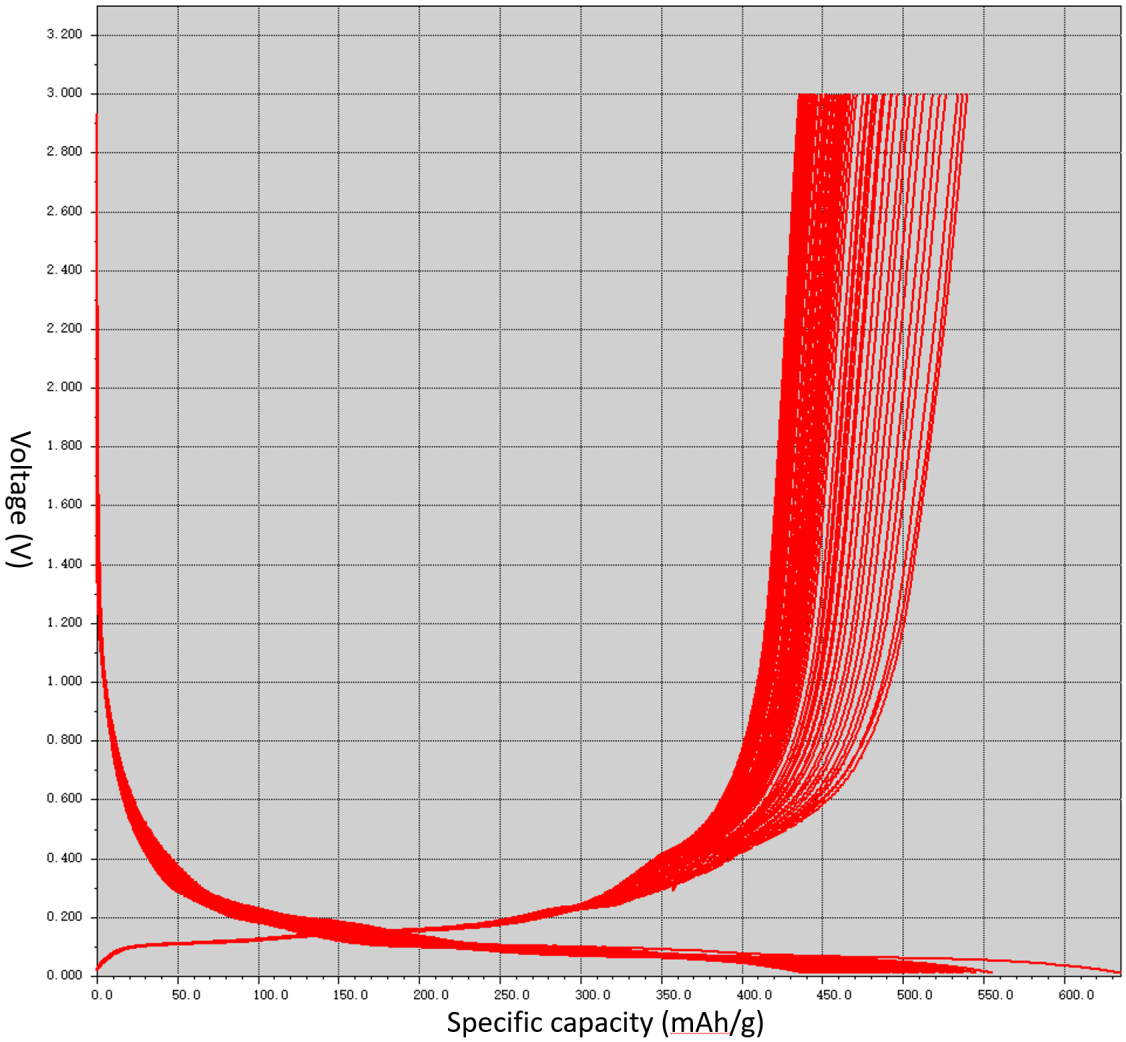

Figure 60. Cycling data from Si@TiO_2 (low amount of Ti)

After reducing the amount of titanium, the capacity of Si@TiO_2 improved a lot. The specific capacity of the first cycle can be up to 630 mAh/g, shown in Figure 60, which is almost double the capacity of the commercial materials used in batteries. Also, the stability was much better than the heavy titanium sample. After 50 cycles, the specific capacity was still 470 mAh/g, which was around 75% of the initial cycle, shown in Figure 60. The heavy one showed less than 50% specific capacity left after 10 cycles.

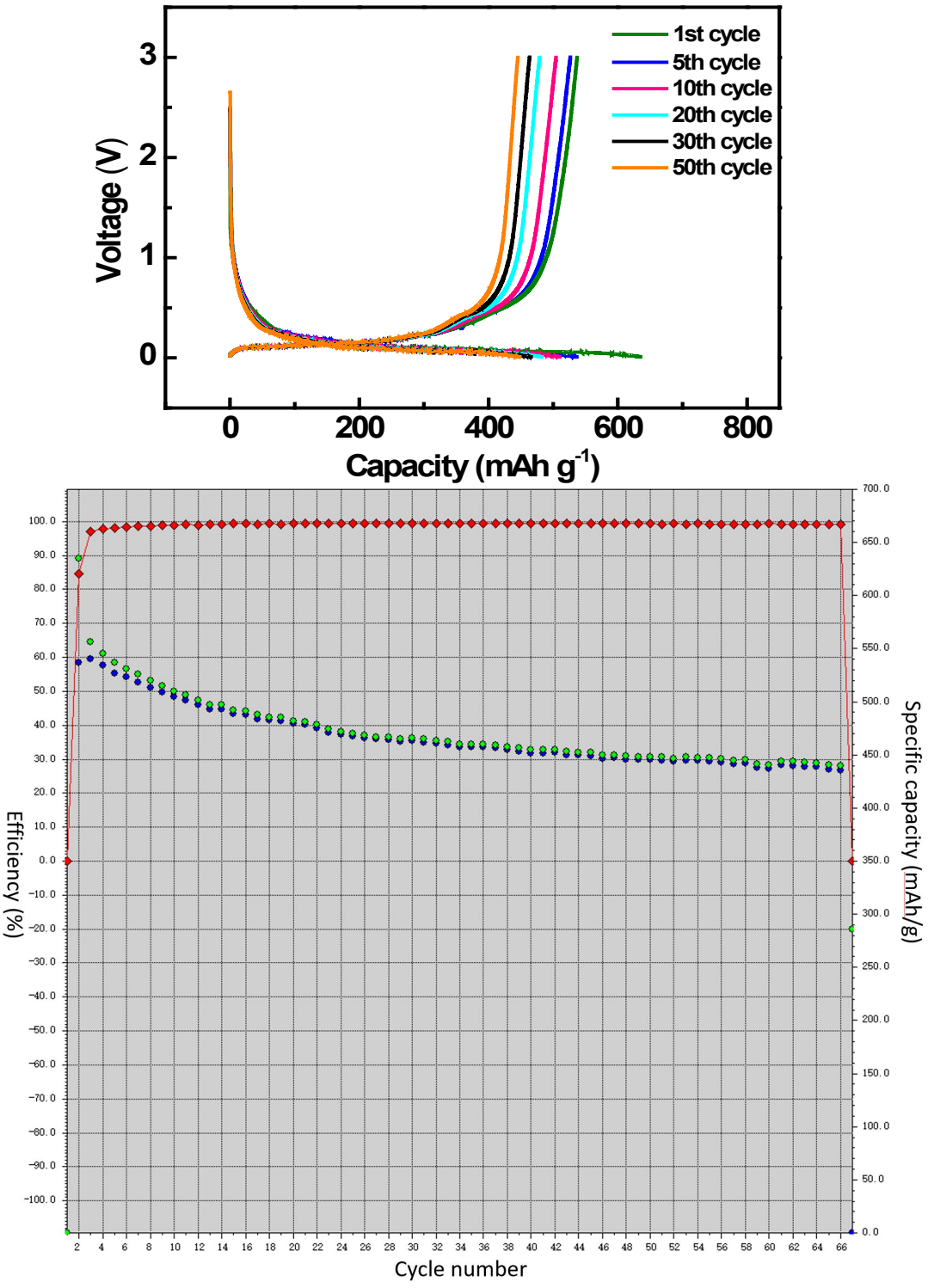

Figure 61. Columbic efficiency and specific capacity from Si@TiO_2 (low amount) and cycling data from Si@TiO_2 (1, 5, 10,20, 30, 50 cycle)

From Figure 62, it can be observed that the columbic efficiency remains at 100% and the specific capacity drops down from 550 mAh/g to 470 mAh/g from the second cycle to the 50th cycle.

A half-cell battery is not able to be used in daily life; it is just a research standard to obtain data from the materials that people focus on. It is therefore necessary to assemble and test a full-cell battery. However, which kind of cathode materials is chosen is quite important. $LiCoO_2$ is selected as the cathode materials. The theory capacity of $LiCoO_2$ is up to 274 mAh/g. The full-cell test results show that

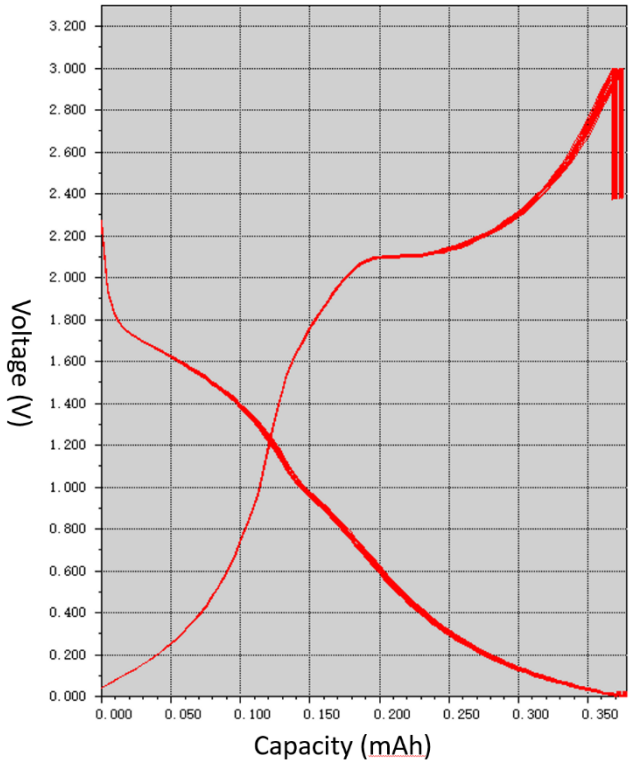

Figure 62. Full-cell cycling data from Si@TiO2 (mass loaded: 0.958mg), around 1 mg si-based active material loaded on the anode chip

the specific capacity for the silicon-based anode can be over 380 mAh/g after 150 cycles, which is over 7 times the specific capacity of graphite, shown in Figure 62 and Figure 63.

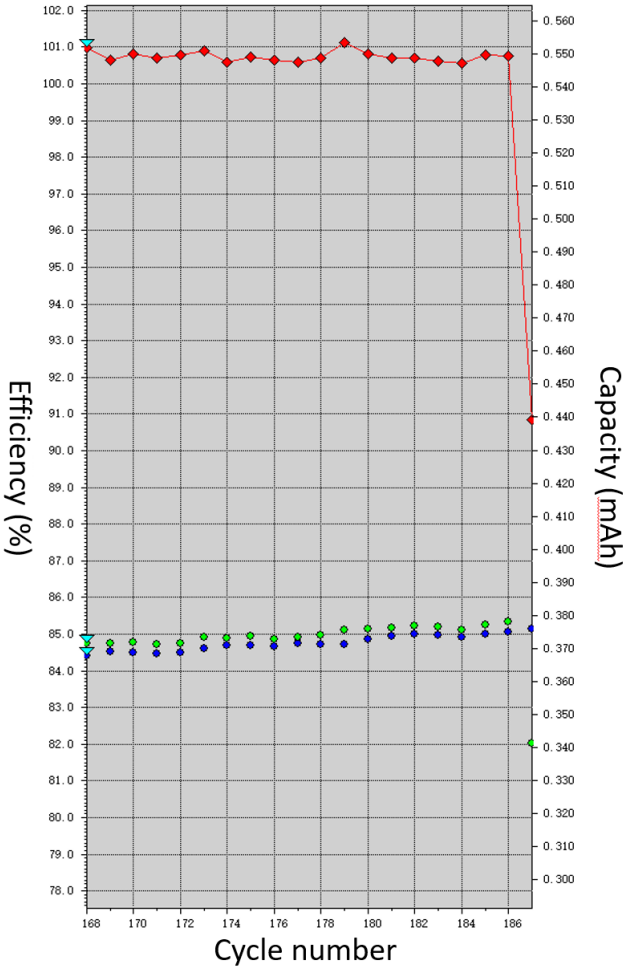

Figure 63. Columbic efficiency and capacity from Si@TiO_2 for full cell

5.7 Electrochemical workstation test

The CV curve is shown in Figure 64, which displays the reduction-oxidation reaction of the silicon-based anode during the first charging and discharging cycle within the voltage range 0-3.0 V at scan rate 0.1 mV s-1. There is a primary reduction peak at about 0.6 V, which mainly corresponds to the silicon and a sharp peak around 1.5 V, possibly owing to the TiO_2. The observed oxidation peaks at 0.7 V and 1.4 V should be attributed to the lithium insertion into the silicon and TiO_2. The TiO_2 shell is too thick for the second charge-discharge cycles. The whole TiO_2 shell contributes to redox reaction; the deep TiO_2 did not participate inthe redox reaction.

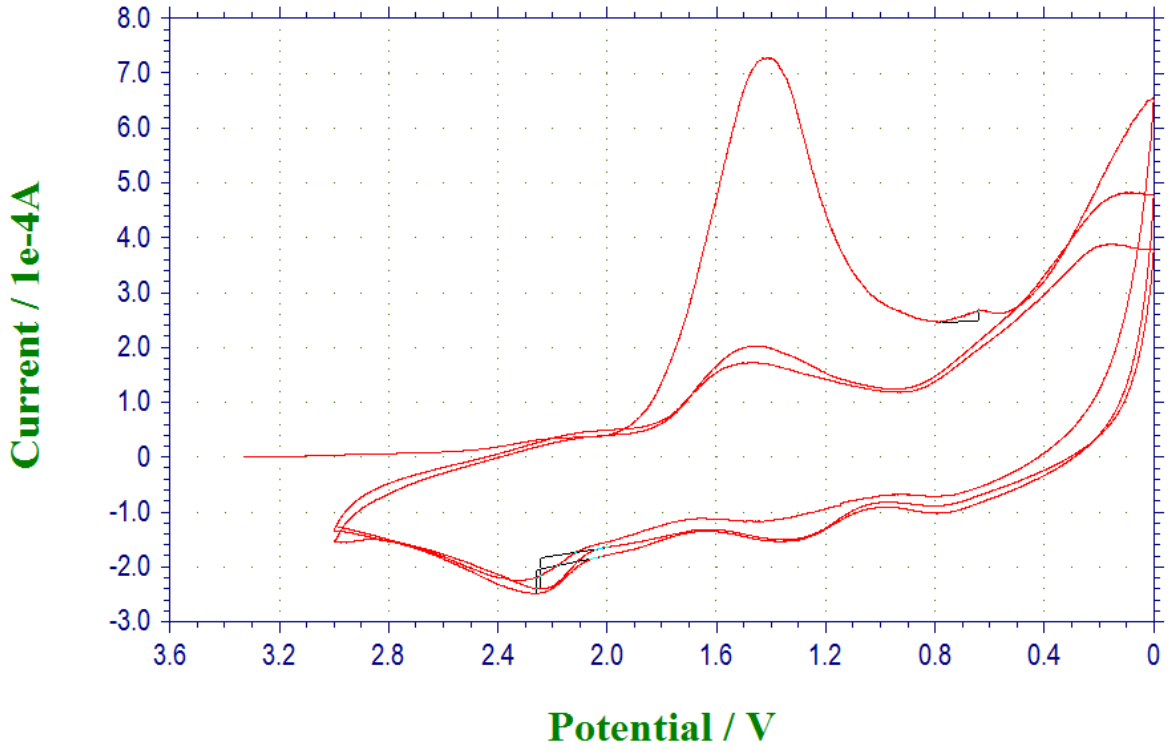

Figure 64. CV curve of $Si@TiO_2$

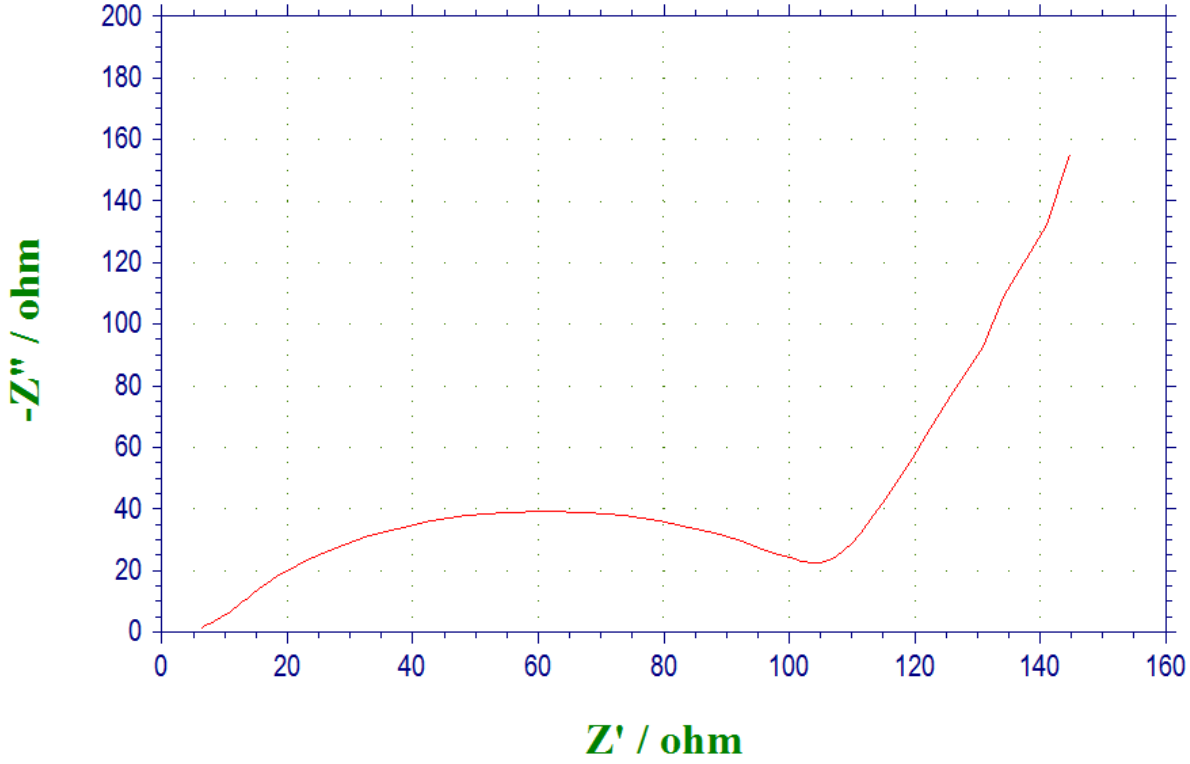

Figure 65. Electrochemical impedance spectra for $Si@TiO_2$ with frequency range from 0.01 to 100 kHz

5.8 EMU study for lithium ion diffusion

5.8.1 Background

The research on energy storage devices such as LIBs is vital for electric vehicles (EVs), electronic devices and grid-scale energy storage. According to the recent reports by market research firms, IHS Isuppli, Transparency Market Research and Taiyou Research, the global market for LIBs alone is expected to expand to US$53.7 billion a year by 2020. The surge in production of EVs by the car industry, including Tesla, Nissan and General Motors, makes a significant contribution to such a high demand. However, the current batteries can only take a car about 400 km after a single charging, which is substantially less than the range of conventional cars. If a battery's energy density could be doubled, the driving range would be doubled.

Research into replacing the traditionally used graphite for silicon as an anode material for LIBs has become increasingly prominent over the years. This is due to the promising electronic properties silicon has to offer over graphite. It has been widely reported that silicon has an exceptionally high specific capacity of 4200 mAh/g, especially when compared to the currently used graphite anode capacity of 372 mAh/g.[8] The higher capacity renders a higher energy density availability in energy storage devices, which is crucial for EVs and grid-scale energy storage. Silicon makes up 27.7% of the Earth's crust and it is the 2nd most abundant element in the crust. In addition to abundance, the availability of silicon is also greater, as silicon is routinely found in the form of complex silicate minerals.

Despite having a much larger theoretical capacity, silicon has been plagued by large volume expansion and contraction upon lithiation and delithiation, resulting in the anode cracking and sintering, thus giving the anode a very short lifetime. The use of silicon nanoparticles compacted together with titanium oxide in a hollow structure has increased the anode lifetime towards commercial application levels with a real capacity of almost twice that of graphite.[9]

5.8.2 Experimental discussion

In a conventional graphite anode, it takes six carbon atoms to hold one lithium ion. In a silicon anode, each silicon atom can hold four – a huge advantage. Here we propose a brand-new project in EMU,[10] to investigate the kinetics of lithium ions in our unique high capacity anode materials with the following two aims:

(i) to study the temperature effect on muon relaxation rate with lithium ion diffusion.
Since this is the first time investigating such anode materials, we need to know whether muons are sensitive to Li intercalated in these materials and the temperatures of Li diffusion occurrence.

(ii) to investigate the effect of silicon nanoparticles' concentration on the capacity of the anodes.

Muon relaxation should increase as lithium concentration increases. Li concentration is dependent on the charging states and it is affected by the silicon nanoparticles in this case.

The anode materials, silicon nanoparticles encapsulated in a TiO_2 hollow structure, have been synthesised in lab, forming a 0.2 mm thickness anode coated with 10 μm copper foil. The areal densities of these materials are such that the majority of muon stops will be in the anode; however, it is likely that there will be a small copper component in the signal, which will be needed to be considered during the data analysis. Anode materials with (a) 0% and (b) 10% silicon nanoparticles mixed with graphite will be studied, each in three charging states: (i) zero charged; (ii) half charged; (iii) fully charged. Therefore, in total, we have six samples to measure. In the future, we need an in-situ measurement facility to accommodate the full study of this project.

A muon study on Li-ion diffusion in Li intercalated graphite C_6Li and $C_{12}Li$ probed has been successfully conducted.[11] We expect to employ a similar methodology to study silicon anodes. Assuming an average count rate of ~120 Mev/hr, samples are to be measured in zero field (ZF), a weak longitudinal field (LF), and a weak transverse field (wTF) in the temperature (T) range between 50 and 500 K using a cryo-oven; we estimate at least 24 hours per sample. In total, we request 6 days to complete this preliminary experiment. The EMU experiment has been carried out with an uncharged sample and a half-charged sample. Along with these two samples, it is important to add the fully charged one to the data set.

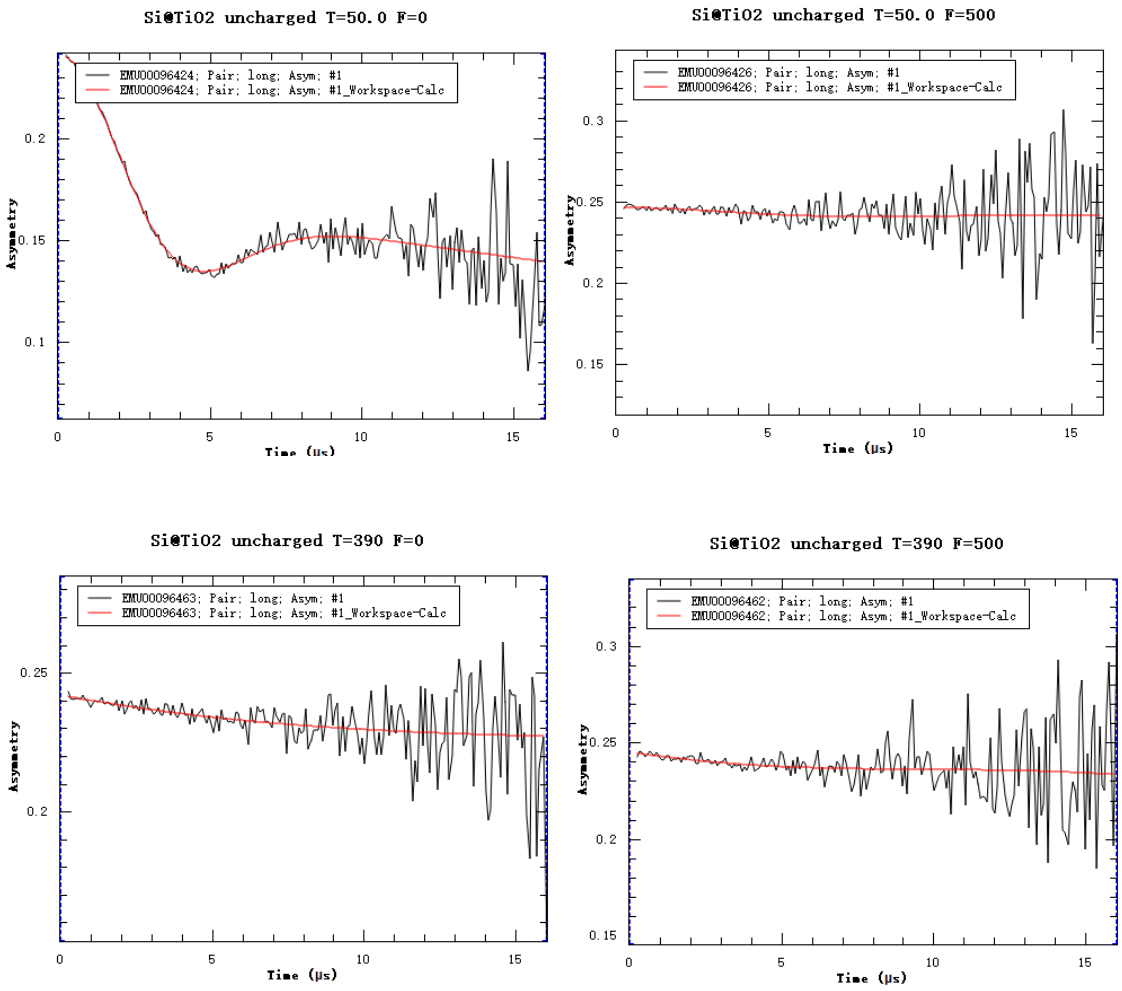

Figure 66. Lithium diffraction from uncharged Si@TiO_2 (a) uncharged Si@TiO_2 at 50 K with zero field (b) uncharged Si@TiO_2 at 50 K with 500 Gauss field (c) uncharged Si@TiO_2 at 390 K with zero field (d) uncharged Si@TiO_2 at 390 K with 500 Gauss field

The form of the ZF data measured at 50K from an uncharged sample during the beamtime can be modelled in a manner consistent with that described in previous research,[12] using a Kubo Toyabe to represent the muons stopped in the Cu foil (sigma ~ 0.37 μs^{-1}) and a relaxation term to describe muons stopped elsewhere. In our case, because there is no Li present and other moments (Ti, Si, O) are weak, this was slowly relaxed at 50K (lambda ~0.018 μs^{-1}) – there is likely to also be a contribution to this decay from muons stopped outside the sample, as the present sample mounting is not fully optimised. When the temperature was increased to 390 K, the lambda was about 0.0039 μs^{-1}.

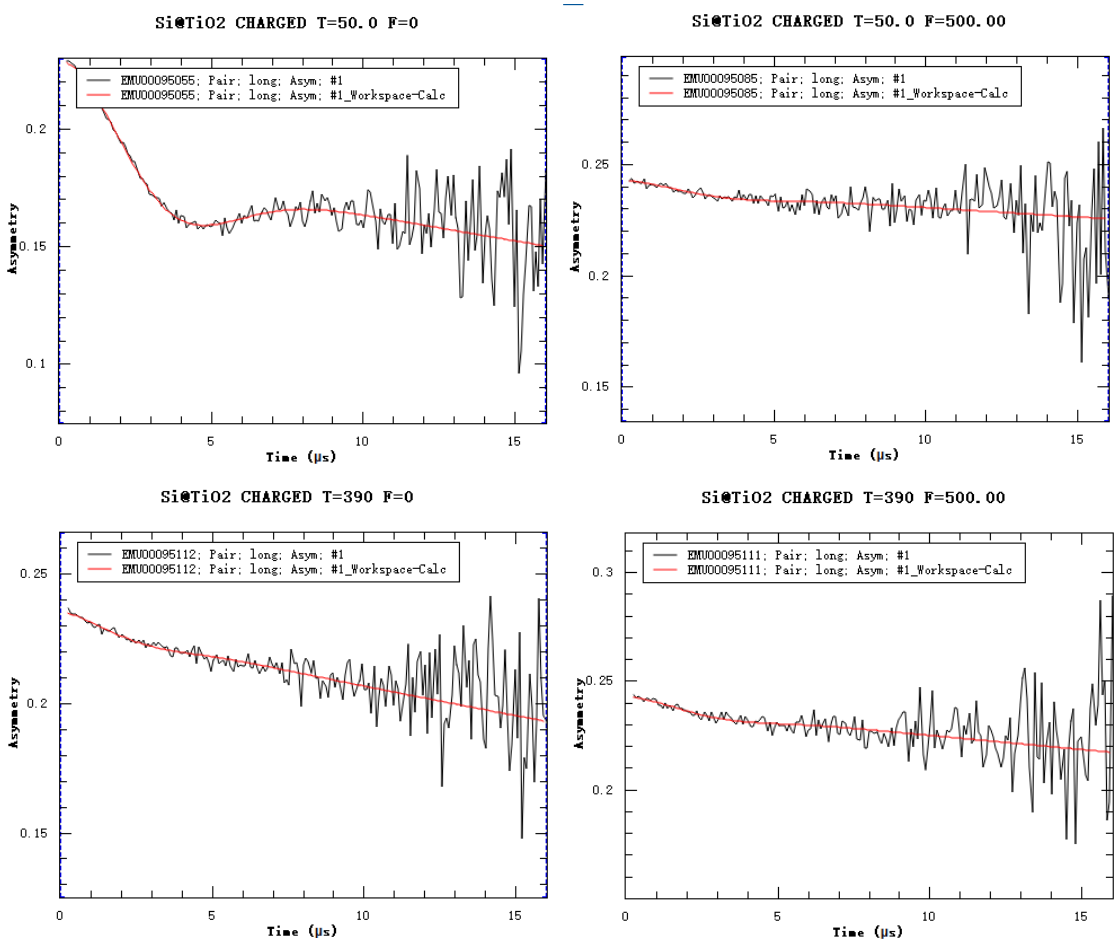

Figure 67. Lithium diffraction from uncharged Si@TiO2 (a) charged Si@TiO2 at 50 K with zero field (b) charged Si@TiO2 at 50 K with 500 Gauss field (c) charged Si@TiO_2 at 390 K with zero field (d) charged Si@TiO2 at 390 K with 500 Gauss field

The half-charged sample was measured with the same temperature and field. After the lithium was added to the sample, the relaxation was stronger than in the uncharged one (lambda ~0.011 μs^{-1}). Comparing these two samples, we are sure that there is a contribution to this decay from muon stopped by the lithium ion.

5.9 Biomass silicon nanoparticles

Apart from Si@TiO_2, biomass silicon nanoparticles are researched in this project as well. Biomass SiO_x based anode material from barley husk was produced by the procedure shown in Chapter 1. More data is required to prove this material has high specific capacity. The specific capacity is related to the x of SiO_x, one way to improve the capacity is to reduce the oxygen. In the future work, the effect of oxygen will be researched.

Biomass SiO_2-C is designed. Biomass SiO_2-C from barley husk was processed by the following Scheme 1:

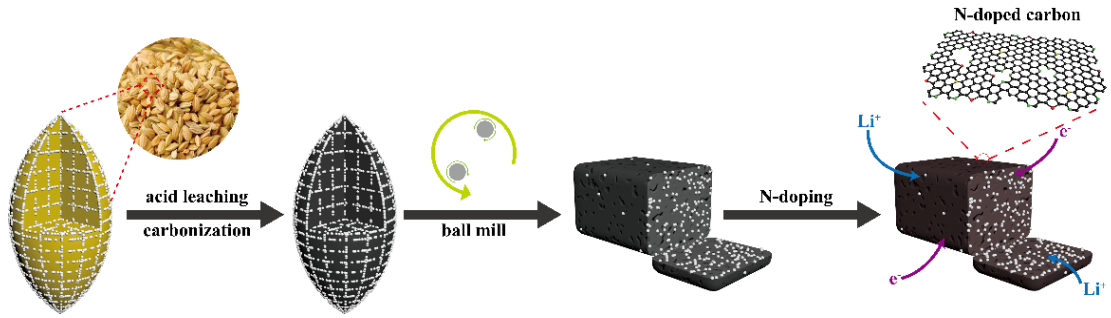

Scheme 1: Procedure for biomass SiO_2-C

Barley husk was dried in an oven at 40°C overnight. Acid wash was taken afterwards to remove the P, K, S etc. contained in the barley husk. Si, O and C will be left for the remaining process. The residue is ball milled to obtain SiO_2 and C. The powder after ball milling is heated to 650°C with N_2 protection. After those steps, SiO_2 is embedded into the carbon.

Also, aluminum could be one factory to improve the performance of this material. In the future work, the effect of addition of aluminum can be researched.

5.9.1 Characteristics of biomass silicon nanoparticles

5.9.1.1 X-ray Photoelectron Spectroscopy

X-ray Photoelectron Spectroscopy (XPS), involves the interactions of x-ray beams with the sample solid surface to produce energy peaks for electrons that react to a specific energy. The XPS survey spectrum obtained from biomass silicon nanoparticles is shown in Figure 68, high resolution of Si 2p and C 1s are shown in (a) and (b).

After heating silicon nanoparticles with N_2 protection in furnace at 650°C, some of the carbon will react with the O of SiO_2, but there was carbon left outside the silicon nanoparticles. This is shown in Figure 68 (b): a strong C 1s peak appears and covers the signal from Si. XPS is a technique to detect the surface of materials. C1s is 83.08% and O1s is 16.35%. The signal from silicon is weak, and the percentage of silicon is 0.57% because the XPS is not able to analyse more than 5-10 nm.

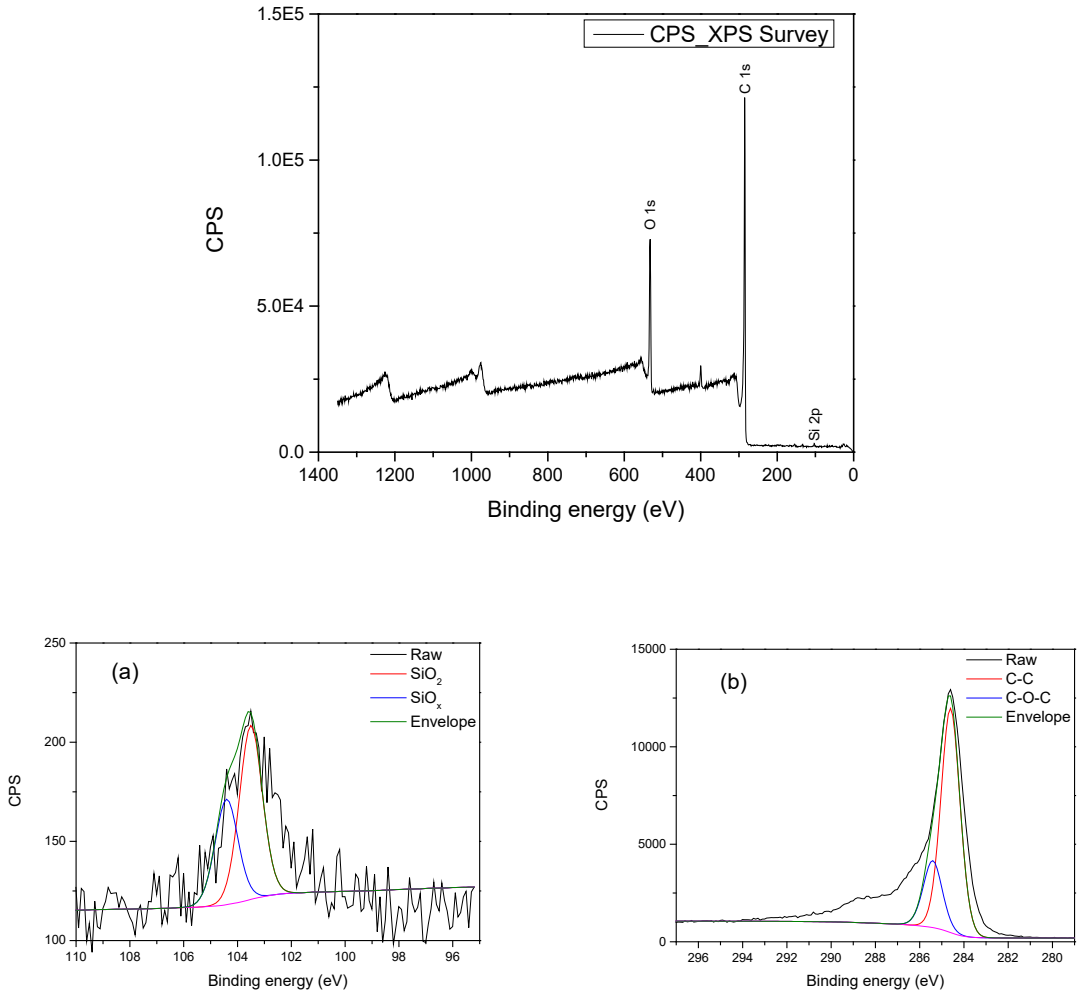

Figure 68. XPS survey for biomass silicon nanoparticles with 1 eV step (a) High resolution spectrum obtained from biomass silicon nanoparticles showing Si2p region with 0.1 eV step (b) High resolution obtained from biomass silicon nanoparticles showing C1s region with 0.1 eV step

5.9.1.2 Scanning electron microscope

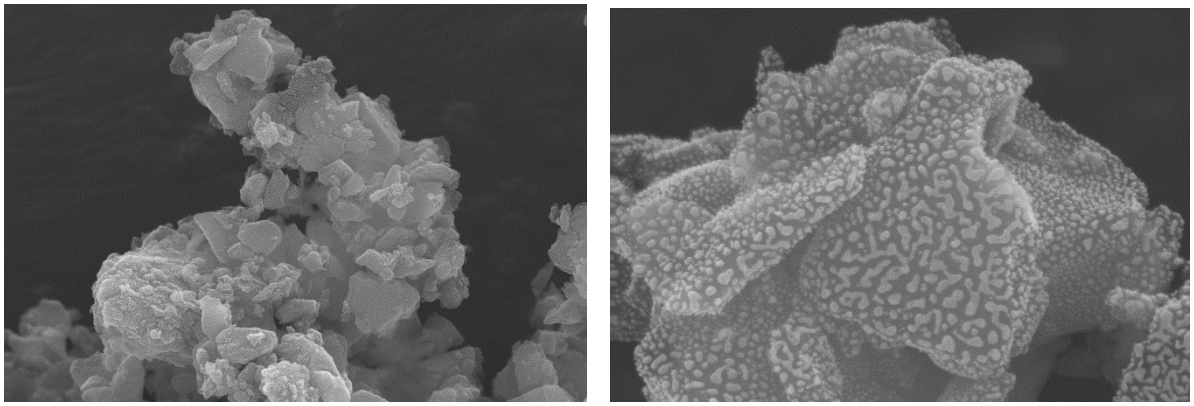

Figure 69. SEM images for biomass silicon nanoparticle with 1 µm and 100 nm scale

SEM images for biomass silicon nanoparticles with 1 µm and 100 nm scale are shown in Figure 69. Due to the large amount of carbon contained in this sample, silicon is not able to be found in SEM. The carbon wrapped outside will potentially help to reduce the volume change while charging and discharging.

5.9.2 Half cell cycling performance test

This silicon based biomass material is coated and assembled into coin cell following the same structure shown in Figure 56. The initial cycle is 1880 mAh/g, but there is a 44% drop between the first and second cycle. After 38 cycles, the specific capacity is still around 800 mAh/g, which is 6 times than graphite. The coulombic efficiency is above 100% for the majority of the 38 cycles.

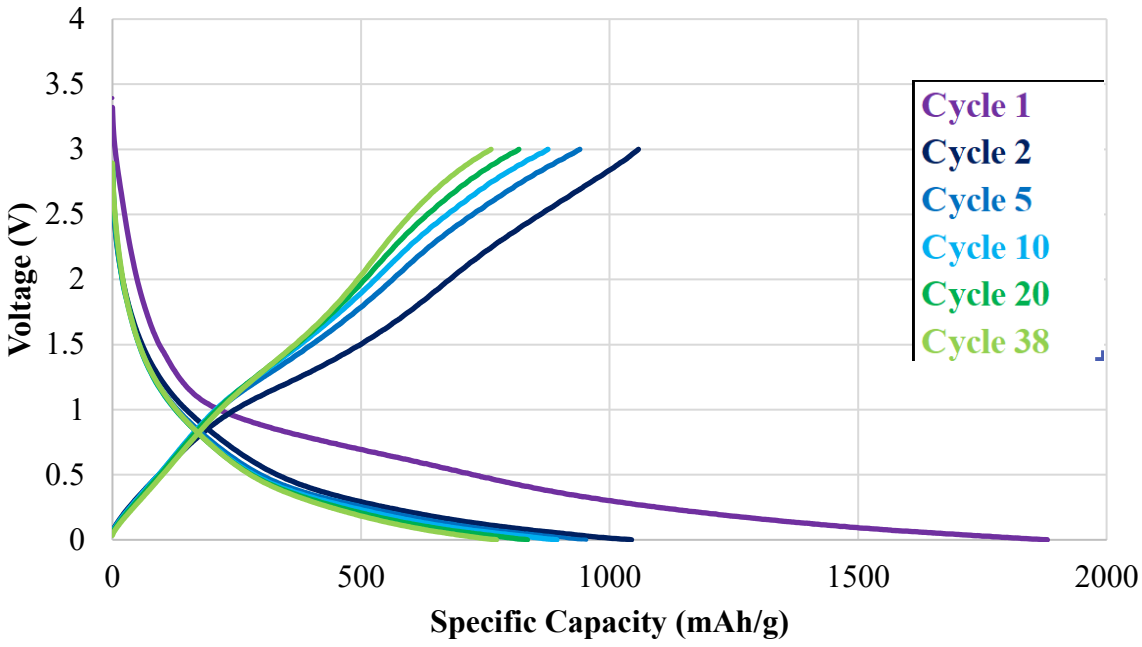

Figure 70. Specific capacity of biomass silicon nanoparticles.

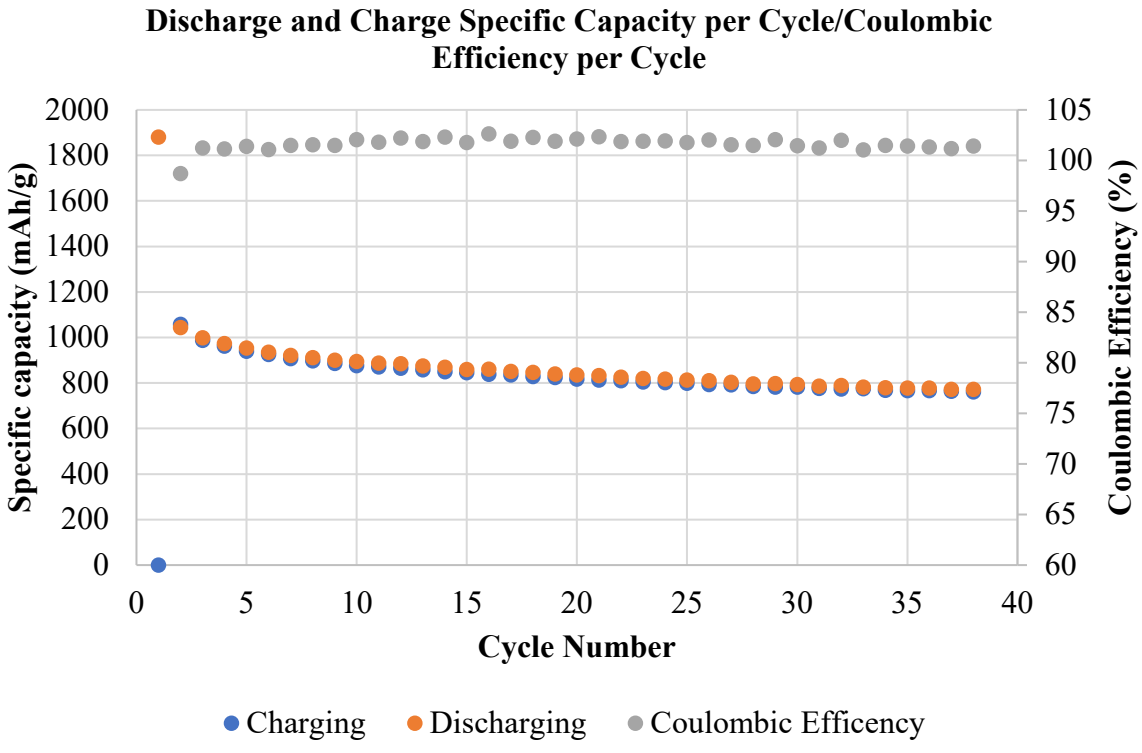

Figure 71. Columbic efficiency and specific capacity from biomass silicon nanoparticles.

5.10 Summary and conclusion

Compare the XPS spectra obtained from Si@C and Si@TiO_2, the peak of Si-C disappears in the XPS spectrum obtained from Si@TiO_2. That clearly prove the carbon was burned away. The peak of TiO_2 in the spectrum of Si@TiO_2 shows that the Ti contained in the titanium isoproproxide is Ti^{4+} and the silicon nanoparticles are wrapped by TiO_2. All the data confirm the hollow structured silicon nanoparticles wrapped by TiO_2 have been successfully synthesized and the battery performance prove the silicon nanoparticles have the potential to be an anode material to improve the performance of market level lithium-ion batteries.

Furthermore, not only the commercial silicon nanoparticles can be the core of the hollow structured nanoparticles. The biomass silicon nanoparticle might be an alternative nanoparticle to reduce the cost. However, the amount of titanium isoproproxide for aging still need to be researched to get a suitable thickness of the TiO_2 shell, not too thick to prevent the redox reaction.

For the biomass silicon nanoparticles, silicon nanoparticles can not be seen in the SEM image because there are a lot of carbon. But a weak signal of Si in the XPS spectrum shows silicon is embedded in carbon. The battery performance proves this biomass silicon nanoparticles can reach to high capacity. However, the capacity of the second cycle drops rapidly. That is similar to the performance of SiO_2. Also, only small amount of silicon contain in the barley as all the silicon are in the barley husk. If the barley husk can be rolled as the raw material and pure the silicon more, the performance would be better.

5.11 References

1. Zhang, F.; Yi, F.; Gao, A.; Shu, D.; Sun, Z.; Mao, J.; Zhou, X.; Zhu, Z.; Sun, Y., Interfacial electrostatic self-assembly in water-in-oil microemulsion assisted synthesis of Li4Ti5O12/Graphene for lithium-ion-batteries. *Journal of Alloys and Compounds* **2020,** *819*, 153018.
2. Tian, Q.; Chen, Y.; Zhang, W.; Sui, Z.; Yang, L., Reducing the excessive interior space of SnO2@C nanotubes by encapsulating SnO2 nanowires for high lithium storage. *Journal of Alloys and Compounds* **2020,** *820*, 153404.
3. Tan, J.; Qi, X.; Mao, J., A novel Al@TiO2-MCMB dual-ion battery with excellent cycling performance at high current rate. *Journal of Alloys and Compounds* **2020,** *818*, 152853.
4. Sun, F.; Huang, K.; Qi, X.; Gao, T.; Liu, Y.; Zou, X.; Wei, X.; Zhong, J., A rationally designed composite of alternating strata of Si nanoparticles and graphene: a high-performance lithium-ion battery anode. *Nanoscale* **2013,** *5* (18).
5. Liu, H.; Bi, Z.; Sun, X.-G.; Unocic, R. R.; Paranthaman, M. P.; Dai, S.; Brown, G. M., Mesoporous TiO2-B Microspheres with Superior Rate Performance for Lithium Ion Batteries. *Advanced Materials* **2011,** *23* (30), 3450-3454.
6. Li, J.; Wang, Y.; Huang, Z.; Huang, K.; Qi, X.; Zhong, J., Synthesis of Si/TiO2core–shell nanoparticles as anode material for high performance lithium ion batteries. *Journal of Materials Science: Materials in Electronics* **2016,** *27* (12), 12813-12819.
7. Jin, Y.; Li, S.; Kushima, A.; Zheng, X.; Sun, Y.; Xie, J.; Sun, J.; Xue, W.; Zhou, G.; Wu, J.; Shi, F.; Zhang, R.; Zhu, Z.; So, K.; Cui, Y.; Li, J., Self-healing SEI enables full-cell cycling of a silicon-majority anode with a coulombic efficiency exceeding 99.9%. *Energy and Environmental Science* **2017,** *10* (2), 580-592.
8. Liu, N.; Lu, Z.; Zhao, J.; McDowell, M. T.; Lee, H.-W.; Zhao, W.; Cui, Y., A pomegranate-inspired nanoscale design for large-volume-change lithium battery anodes. *Nature Nanotechnology* **2014,** *9* (3), 187-192.
9. Jin, Y.; Li, S.; Kushima, A.; Zheng, X.; Sun, Y.; Xie, J.; Sun, J.; Xue, W.; Zhou, G.; Wu, J.; Shi, F.; Zhang, R.; Zhu, Z.; So, K.; Cui, Y.; Li, J., Self-healing SEI enables full-cell cycling of a silicon-majority anode with a coulombic efficiency exceeding 99.9%. *Energy & Environmental Science* **2017,** *10* (2), 580-592.
10. Giblin, S. R.; Cottrell, S. P.; King, P. J. C.; Tomlinson, S.; Jago, S. J. S.; Randall, L. J.; Roberts, M. J.; Norris, J.; Howarth, S.; Mutamba, Q. B.; Rhodes, N. J.; Akeroyd, F. A., Optimising a muon spectrometer for measurements at the ISIS pulsed muon source. **2014,** *751*, 70-78.
11. Izumi Umegaki, S. K., Hiroshi Sawada, Hiroshi Nozaki, Yuki Higuchi, Kazutoshi Miwa, Yasuhito Kondo, Martin Månsson, Mark Telling, Fiona C. Coomer, Stephen P. Cottrell, Tsuyoshi Sasaki, Tetsuro Kobayashia, Jun Sugiyama, Li-ion diffusion in Li intercalated graphite C6Li andC12Li probed by uSR. *Phys. Chem. Chem. Phys.* **2017,** *19* (19058).
12. Umegaki, I.; Kawauchi, S.; Sawada, H.; Nozaki, H.; Higuchi, Y.; Miwa, K.; Kondo, Y.; Månsson, M.; Telling, M.; Coomer, F. C.; Cottrell, S. P.; Sasaki, T.; Kobayashi, T.; Sugiyama, J., Li-ion diffusion in Li intercalated graphite C6Li and C12Li probed by μ+SR. *Physical Chemistry Chemical Physics* **2017,** *19* (29), 19058-19066.

Chapter 6 Future work

In this chapter, future work is proposed: silicon nanoparticles from natural product for lithium-ion batteries, synthesized Si@TiO_2 for lithium-ion batteries and EMU.

Contents

Future work can be divided into two parts. The first part is silicon nanoparticles embedded in carbon from barley husk. The second part is synthesized hollow-structured silicon nanoparticles. The second part can be divided into two separate research purpose. One is for lithium-ion batteries, one is for EMU.

6.1 Biomass SiO_x based anode material

Background of biomass SiO_x based anode material from barley husk was shown in Chapter 1 and some data is shown in Chapter 5. However, more data is required to prove this material has high specific capacity.

The specific capacity is related to the x of SiO_x, one way to improve the capacity is to reduce the oxygen. In the future work, the effect of oxygen will be researched. Possibly, the speed of ball milling can be increased to react more O with C to improve the purity of Si.

The original material using in this project is the whole wheat, the barley husks are the purpose raw material. After changing to barley husks, the amount of carbon will be reduced.

Also, aluminum could be one factory to improve the performance of this material. In the future work, the effect of addition of aluminum can be researched.

One more thing needs to be researched is the pollution during the heating in furnace, it might increase the cost in production.

6.2 Synthesis of hollow structured silicon nanoparticles

The procedure of this material is shown in Chapter 5. This material has shown higher specific capacity than the commercial carbon used in batteries. However, it is still far away from the theoretic specific capacity of Si. The material of the shell can be changed to get better performance in the future.

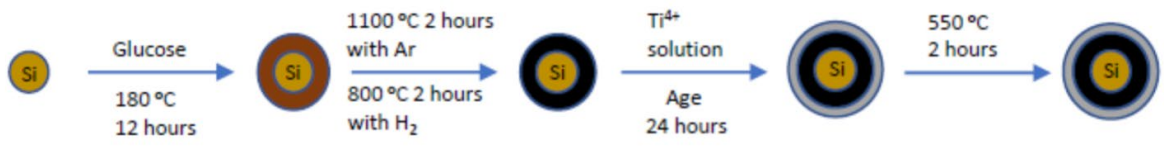

Figure 72. Future synthesis of hollow structured silicon nanooptics.

The structure of hollow structured silicon nanoparticles can be adjusted to get higher capacity. An additional carbon layer can be added between TiO_2 and Si. For the existing sample, a better set of electrolyte and binder should be tried to improve the performance. Also, lower amount of Ti^{4+} can be tried to reduce the TiO_2 shell outside the silicon nanoparticles.

For the EMU experiment, the fully charge and fully discharged data is needed to be compared.

Appendix: List of paper, conferences and posters

During my four years' PhD experience, one paper has been published and the work is included in this thesis.

I. A Muon Spectroscopic and Computational Study of the Microscopic Electronic Structure in Thermoelectric Hybrid Silicon Nanostructures

Yue, C., Liborio, L., Bian, T., Sturniolo, S., Wright, J. A., Cottrell, S. P., Khasanov, R., Simutis, G., Jayasooriya, U. A. & Chao, Y.,

The Journal of Physical Chemistry C. 124, 18, p. 9656-9664 9 p. (2020)

Presentation and posters are listed below:

Poster: Muon spin spectrum of thermoelectric Silicon Quantum Dots,

at *UK Neutron and Muon Science and User Meeting* (2019), *ISIS Student Meeting* (2019)

Presentation: Silicon nanoparticles for application in lithium-ion batteries,

at *UEA Chemistry Research Day* (2019)